PROCEEDINGS QTS'23

On the Bures metric for rank-deficiency qudit states

Martin Bureš[1,2*], **Arsen Khvedelidze**[2,3,4], **Dimitar Mladenov**[5]

[1] *Institute of Experimental and Applied Physics, Czech Technical University in Prague, Czech Republic*
[2] *Laboratory of Information Technologies, Joint Institute for Nuclear Research, Dubna, Russia*
[3] *A Razmadze Mathematical Institute, Iv. Javakhishvili, Tbilisi State University, Tbilisi, Georgia*
[4] *Institute of Quantum Physics and Engineering Technologies, Georgian Technical University, Tbilisi, Georgia*
[5] *Theoretical Physics Department, Faculty of Physics, Sofia University "St Kliment Ohridski", Sofia, Bulgaria*
*E-mail: bures@physics.muni.cz

Abstract

The Bures-Fisher metric on the subset $\mathfrak{P}_{N,k}$, of state space of $N-$level quantum system, comprising of rank-k density matrices is given by a solution to the Uhlmann equation. Solving the Uhlmann equation on $\mathfrak{P}_{N,k}$, we use its decomposition $\mathfrak{P}_{N,k} = \bigcup_\alpha \mathfrak{P}^k_{[H_\alpha]}$, into a finite union of strata $\mathfrak{P}^k_{[H_\alpha]}$ of different $SU(N)$ orbit types with all admissible isotropy groups H_α. Solution to the Uhlmann equation on the corresponding orbits stratum $\mathfrak{P}^k_{[H_\alpha]}$, defines uniquely the Bures-Fisher metric for a rank deficient states.

Recent developments in the emerging field of quantum computation and quantum information theory have received a great deal of attention to studies of $N-$level systems. According to the statistical interpretation of quantum theory, it is a new kind of a probabilistic model and quantum $N-$level system is an analogue of the classical probability model with a finite probabilistic space [1]. Despite being the simplest quantum system, it turns out that this quantum probabilistic model drastically differs from its classical counterpart. The quantum analogue of classical probability distribution is the state of system, described by a density matrix $\varrho \in \mathfrak{P}_N$. The state space $\mathfrak{P}_N$ comprises all $N \times N$ Hermitean, normalized semi-positive matrices,

$$\mathfrak{P}_N = \{\, X \in M_N(\mathbb{C}) \,|\, X = X^\dagger \,,\; X \geq 0 \,,\; \mathrm{Tr}\, X = 1 \,\} \,. \tag{1}$$

The analogue of a classical random variable is a quantum observable, represented by an $N \times N$ Hermitian matrix A. If $A = \sum_i a_i |e_i\rangle\langle e_i|$ is the spectral decomposition of A with respect to the orthonormal basis of eigenvectors $|e_i\rangle$ corresponding to eigenvalues, $\mathrm{spec}(A) = \{a_1, a_2, \dots, a_N\}$, then the *probability distribution of the observable A in state ϱ over spectrum* is defined as:

$$p^A_\varrho(a_i) = \mathrm{Tr}\biggl(\varrho\, |e_i\rangle\langle e_i|\biggr) \,, \qquad i = 1, 2, \dots, N \,. \tag{2}$$

Following this analogy, many methods from information geometry, the geometry of manifolds of probability distributions in classical statistics [2], have been adopted for various studies of quantum systems [3]. Particularly, an issue of establishing of Riemannian structures on the quantum counterparts of space of probability measures, became a subject of recent investigations. Nowadays, due to practical goals in the area of modern quantum technologies, a special attention has been drawn to the question of the determination of quantum analogues of a well-known, natural Riemannian metric, the so-called Fisher metric, as well as a family of affine connections.

Our report is devoted to the discussion of this topic within quantum information geometry. We will analyse the metric on $\mathfrak{P}_N$, originated from the distance function $d(\varrho_1, \varrho_2)$ between density matrices $\varrho_1, \varrho_2 \in \mathfrak{P}_N$, which is known under different names, the Fisher (in statistics), Bures (classical and quantum information theory), Wasserstein metric (optimal transport):

$$d(\varrho_1, \varrho_2) := \sqrt{\mathrm{tr}\varrho_1 + \mathrm{tr}\varrho_2 - 2\mathrm{tr}\left(\varrho_1^{1/2}\, \varrho_2\, \varrho_1^{1/2}\right)^{1/2}} \,. \tag{3}$$

The distance function (3) corresponds to the Bures metric which belongs to the special class of the so-called monotone Riemannian metrics. It is minimal among all monotone metrics and its extension to pure states is exactly the Fubini–Study metric [4].

Explicit formulae for the Bures metric are known for special cases. Particularly, Dittmann has derived several explicit formulae (that do not require any diagonalization procedure) for the Bures metric on the manifold of finite-dimensional nonsingular density matrices [5, 6, 7, 8].

However, owing to the nontrivial differential geometry of the state space $\mathfrak{P}_N$, studies of its Riemannian structures require a refined analysis for the non maximal rank density matrices. Indeed, let $\mathfrak{P}_{N,k} \subset \mathrm{M}_N(\mathbb{C})$ be a manifold comprising of the normalized $N \times N$ density matrices of rank k. According to [8], every $\mathfrak{P}_{N,k}$ admits the Bures metric g_B and hence one can consider subspace of fixed rank as the Riemannian manifold $(\mathfrak{P}_{N,k}, \mathrm{g}_B)$. The union $\mathfrak{D}_N := \bigcup_{k=1}^N \mathfrak{P}_{N,k}$ is not a manifold, but a convex subset of affine space of all normalized Hermitian matrices. Furthermore, $\mathfrak{D}_N$ cannot be isometrically embedded to any manifold. Due to these reasons the interplay between the Bures metric and the quantum Fisher information deserves a special analysis (see e.g. the discussion in [9]).

In the present report, following the purification method and the fundamental principle of parallel transport along the state (see e.g. [5]) we will derive the metric on each strata $\mathfrak{P}_{N,k}$ from the the bundle projection $M_N(\mathbb{C}) \to \mathfrak{P}_N$. Our exposition is exemplified in details by considering the Bures metric for qubit $(N = 2)$ and qutrit $(N = 3)$ in different strata.

References

[1] A.S. Holevo, Statistical Structure of Quantum Theory, Springer, 2001.

[2] S. Amari, Information Geometry and Its Applications, Springer, Japan, 2016.

[3] I. Bengtsson and K. Zyczkowski, Geometry of Quantum States: An Introduction to Quantum Entanglement, 2nd edition. Cambridge University Press, (2017)

[4] D. Petz, C. Sudár, Geometries of quantum states, Journal of Mathematical Physics 37 (6), 2662-2673 (1996).

[5] A. Uhlmann, Geometric Phases and Related Structures, Rep. Math. Phys., **36** 461-481, (1995).

[6] M. Hubner, Explicit computation of the Bures distance for density matrices, Physics Letters A163, 239 (1992).

[7] J. Dittmann, On the Riemannian Geometry of Finite Dimensional Mixed States, Seminar Sophus Lie 3, 73-87, (1993).

[8] J. Dittmann, On the Riemannian metric on the space of density matrices, Rep. Math. Physics, 36 309–315, (1995).

[9] D. Šafránek, Discontinuities of the quantum Fisher information and the Bures metric, Physical Review A95, 052320 (2017).

Depth analysis of variational quantum algorithms for heat equation

Nikita Guseynov[*1,2], **Andrey Zhukov**[1],
Walter Pogosov[1,2,3], **Andrey Lebedev**[1,2]

[1]*Dukhov Research Institute of Automatics (VNIIA), Moscow, 127030, Russia*
[2]*Moscow Institute of Physics and Technology (MIPT), Dolgoprudny, 141700, Russia*
[3]*Institute for Theoretical and Applied Electrodynamics, Russian Academy of Sciences, Moscow, 125412, Russia*
*E-mail: guseynovnm@my.msu.ru

I. INTRODUCTION

Quantum computing is a promising technology based on the principles of quantum mechanics [1]. The main motivation is outperform the state-of-the-art classical algorithms and achieve the so called quantum supremacy [2, 3]. Well-known examples are the quantum search algorithm [4] and Shor's factorization algorithm [5], which are both superior to the classical ones. Quantum computers can also be useful in various linear algebra problems. A remarkable example is the Harrow, Hassidim, and Lloyd (HHL) algorithm for solving systems of linear equations [6, 7]. Because the classical algorithms generally have the polynomial complexity in the matrix size N, HHL algorithm provides the exponential speed-up in the case of sparse matrices. This algorithm however requires a large-depth quantum circuit composed of highly accurate quantum gates. Both these requirements are problematic in the present era of noisy intermediate-scale quantum (NISQ) computers [8]. Error correction codes [9–11] and error mitigation techniques [12–14] could potentially overcome these problems, however, the state-of-the-art quantum devices lack enough number of qubits to work in the fault-tolerant regime.

II. RESULTS

The paper studies the implementation of three variational quantum algorithms for solving the heat equation presented in the finite difference form. This problem is reduced to the solution of the system of linear equations arising at each discrete step of the time evolution.

In the first approach (direct variational method) the expectation value of the Hamiltonian (2) is minimized on some class of probe functions. The Hamiltonian is constructed in a way that its ground state corresponds to the solution of the system of linear equations.

$$|x\rangle = A^{-1}|b\rangle . \tag{1}$$

It can be readily shown [15] that this solution $|x\rangle$ is the ground state of the Hamiltonian

$$H = A^{+}(I - |b\rangle\langle b|)A, \tag{2}$$

We performed proof-of-principles quantum computation with the matrix of size 4×4 using the real quantum processor of IBM Q project. The direct variational algorithm demonstrates a fundamental possibility of solving the system of linear equations (3) on a quantum computer. However, the exponential number of Pauli products in the matrix decomposition does not allow one to achieve the quantum speedup (superiority over classical algorithms). In some cases it is possible to effectively sample over these products if we know the distribution of the decomposition coefficients, but this requires a separate study.

$$Ax = b, \tag{3}$$

$$A(c) = \begin{pmatrix} -2-c & 1 & 0 & \cdots & 0 & 1 \\ 1 & -2-c & 1 & \cdots & 0 & 0 \\ 0 & 1 & -2-c & \cdots & 0 & 0 \\ \vdots & & \ddots & \ddots & & \vdots \\ 0 & 0 & \cdots & -2-c & 1 & 0 \\ 0 & 0 & \cdots & 1 & -2-c & 1 \\ 1 & 0 & \cdots & 0 & 1 & -2-c \end{pmatrix}, \tag{4}$$

$$x = \begin{pmatrix} U_0^{\tau+1} \\ U_1^{\tau+1} \\ \vdots \\ U_{N-1}^{\tau+1} \end{pmatrix}, \qquad b = \begin{pmatrix} b_0^{\tau} \\ b_1^{\tau} \\ \vdots \\ b_{N-1}^{\tau} \end{pmatrix}. \tag{5}$$

The second approach (Hadamard test approach) is based on the minimization of the expectation value of the same Hamiltonian, but the problem of the exponential number of Pauli products is eliminated by using the Hadamard test [16]. A numerical simulation of the algorithm was performed with up to $n = 8$ qubits using three different entanglers or Ansatzs. The results show that it can be possible to achieve the quantum superiority, but the simulations with more qubits are required to definitively confirm this issue. It is also important to identify an effective entangler for the investigated problem. With this approach, three types of Ansatzes were tested: the Hardware Efficient, Checkerboard and the Digital-Analog Ansatz. The best results were obtained for the Checkerboard Ansatz, as it gives a more uniform entanglement. In addition, by increasing the grid parameter c, see, one decreases the number of required layers in the Ansatz. An exponential acceleration of up to eight qubits was demonstrated for this entangler. However, we argue that the considered number of qubits is not enough for an unambiguous conclusion about the advantage of the algorithm over the classical one.

The third type of approach (Ansatz tree approach) minimizes the l_2 norm (6), rather than the expectation value of the Hamiltonian.

$$L_R(x) = \| Ax - |b\rangle \|_2^2 = x^\dagger A^\dagger Ax - 2Re\{x^\dagger A\,|b\rangle\} + 1; \tag{6}$$

The algorithm is based on the unitary decomposition of the matrix (4). For the heat equation it turns out to be advantageous to switch to the Fourier representation by using the quantum Fourier transform. In the Fourier representation, the matrix becomes diagonal with a sinusoidal spectrum. Then we used a technique that allows us to replace the spectrum of this matrix by a piecewise-quadratic function, which, at the level of the original discretized problem, corresponds to the elimination of high-frequency oscillations of the solution, justified from the physical point of view. This makes it possible to radically reduce the number of Pauli products in the matrix decomposition. The simulation of the algorithm with up to eight qubits was performed and the complexity of the algorithm was estimated. The complexity is determined by the depth of the algorithm. The results show that the depth depends polynomially on the number of qubits for certain values of the grid parameter c. This reveals the fundamental ability of the Ansatz Tree Approach to demonstrate the quantum superiority for the heat equation.

Thus, the third approach can be considered as the most promising. The reason is that Ansatz Tree Approach makes use of the explicit form of the matrix (4), unlike the other algorithms discussed, which use the universal entanglers.

---

[1] R. P. Feynman, Int. J. Theor. Phys **21** (1982).
[2] H.-S. Zhong, H. Wang, Y.-H. Deng, M.-C. Chen, L.-C. Peng, Y.-H. Luo, J. Qin, D. Wu, X. Ding, Y. Hu, et al., Science **370**, 1460 (2020).
[3] R. Li, B. Wu, M. Ying, X. Sun, and G. Yang, IEEE Transactions on Parallel and Distributed Systems **31**, 805 (2019).
[4] L. K. Grover, in *Proceedings of the twenty-eighth annual ACM symposium on Theory of computing* (1996), pp. 212–219.
[5] P. W. Shor, SIAM Review **41**, 303 (1999).
[6] A. W. Harrow, A. Hassidim, and S. Lloyd, Phys. Rev. Lett. **103**, 150502 (2009).
[7] A. Montanaro and S. Pallister, Phys. Rev. A **93**, 032324 (2016).
[8] J. Preskill, Quantum **2**, 79 (2018).
[9] S. J. Devitt, W. J. Munro, and K. Nemoto, Rep. Prog. Phys. **76**, 076001 (2013).
[10] K. Noh and C. Chamberland, Phys. Rev. A **101**, 012316 (2020).
[11] L. Egan, D. M. Debroy, C. Noel, A. Risinger, D. Zhu, D. Biswas, M. Newman, M. Li, K. R. Brown, M. Cetina, et al., Nature **598**, 281 (2021).
[12] K. Temme, S. Bravyi, and J. M. Gambetta, Phys. Rev. Lett. **119**, 180509 (2017).
[13] S. Endo, S. C. Benjamin, and Y. Li, Phys. Rev. X **8**, 031027 (2018).
[14] A. Zhukov and W. Pogosov, Quant. Inf. Proc. **21**, 1 (2022).
[15] X. Xu, J. Sun, S. Endo, Y. Li, S. C. Benjamin, and X. Yuan, Science Bulletin **66**, 2181 (2021).
[16] H.-Y. Huang, K. Bharti, and P. Rebentrost, New J. of Phys. **23**, 113021 (2021).

Non-markovianity estimation for qubit of 5-qubit quantum computer

Pavel Vedrukov[1*], Alexey Liniov[1], Iosif Meerov[1], Sergey Denisov[1,2]

[1] *Lobachevsky State University of Nizhny Novgorod, Nizhniy Novgorod, Russia*
[2] *Oslo Metropolitan University, Oslo, Norway*
*E-mail: pavelvedrukov@mail.ru

Abstract

We present the results of experiments on estimating the spam error of the qubit and constructing Kraus operators that describe the discrete evolution of the qubit. The obtained data were used to estimate the non-Markovian property of the qubit.

Introduction

The processing of measurements of special quantum circuits [1] using the method of harmonic inversion [2] makes it possible to restore a set of eigenvalues that form a diagram qualitatively similar to the full spectrum of Liouvillian of open quantum system presented in [3]. Lindblad tomography method [4] makes it possible to estimate SPAM Errors, Kraus operators, Non-markov measure, the Hamiltonian, quantum jump operators, and corresponding decay rates that describe the evolution of open quantum system.

We estimated SPAM errors, reconstructed the evolution by Kraus operators for discrete times, and estimated the non-Markovianity of the first qubit of the ibmq_belem quantum computer on the IBM Quantum Computing platform.

Building quantum circuits

The first step of the Lindblad tomography method is to build a set of specialized quantum circuits.

1. The qubit is initialized by a state ρ_0 close to the initial state and one of six one-qubit rotations $R_s = \{I, X_\pi, Y_{\frac{\pi}{2}}, Y_{-\frac{\pi}{2}}, X_{-\frac{\pi}{2}}, X_{\frac{\pi}{2}}\}$ that initialize the qubit in one of the six ground states on the Bloch sphere ($|0\rangle, |1\rangle, |+\rangle, |-\rangle, |i\rangle, |-i\rangle$) respectively.

2. Waiting cicuit is applied to the qubit. The waiting circuit is described by the function $\widetilde{I}(t) = U_1^\dagger U_2^\dagger ... U_t^\dagger U_t ... U_2 U_1$. Each use of a pair of gates $U_i^\dagger U_i$ increases the circuit "waiting time" by 1.

3. A qubit is measured in one of three Pauli bases (x, y, z) by applying one-qubit rotations $R_b = \{Y_{-\frac{\pi}{2}}, X_{\frac{\pi}{2}}, I\}$ and the measurement operation.

These steps are repeated for all combinations of initial rotations, waiting circuit duration $t = [0...99]$ and measurement bases. We performed 20,000 measurements for each of 1800 quantum circuits on ibmq_belem quantum computer.

SPAM errors estimation

Once we have a full set of data, we can analyze the initial state preparation error and measurment error of the quantum computer using the maximum likelihood estimation.

The imperfect initial state is parametrized as the density matrix of a one-qubit quantum system ρ_0 limited by physical conditions: it must have a unit trace and be positive semi-definite. The positive semidefiniteness is ensured in the optimization procedure by expressing ρ_0 in the form of Cholesky decomposition $\rho_0 = AA^\dagger$ and estimating the matrix A without conditions. The single trace condition can be added as $\rho_{00} + \rho_{11} = 1$.

Measurement error is described by the positive operator-valued measure (POVM). The measurement is initially performed in z-basis. Measurements in other bases are performed by rotating the qubit before the measurement. This rotations can't be considered error-free and therefore they should be parameterized as arbitrary rotation matrices and evaluated together with POVM and imperfect initial state. It should be noted that the error of the qubit rotation operation is significantly less than the error of the measurement operation. It is reasonable to assume that the qubit rotation error has small effect on initial state preparation and measurement. One-qubit POVM consists of two operators representing 2×2 matrices M_0, M_1: $M_0 + M_1 = 1$. Probability of measurement in the initial state $\rho_0 = Tr(\rho M_0)$ and the excited state $\rho_1 = Tr(\rho M_1)$. POVM matrices are positive semidefinite and this condition can be avoided by using the Cholesky decomposition of matrices (as with the initial state matrix).

As a result, we used the likelihood function of the following form to find an estimate of the prepared initial state ρ_0 and operators M_0, M_1

$$ln(\mathcal{L}_{SPAM}) = \sum_{b,s} f(s,b) ln(Tr[\rho_s M_b]) + \overline{f}(s,b) ln(Tr[\rho_s (I - M_b)]). \tag{1}$$

where $b \in z, x, y$ is the element index in the set of measurement bases, $s \in (|0\rangle, |1\rangle, |+\rangle, |-\rangle, |i\rangle, |-i\rangle)$ is the element index in the set of imperfect begin states, $f(s,b)$ and $\overline{f}(s,b)$ are total numbers of 0's and 1's from measurements, $M_b = R_b M_0 R_b^\dagger$ would require estimating the matrix elements of M_0, $\rho_s = R_s \rho_0 R_s^\dagger$ would require estimating the matrix elements of the ρ_0.

Reconstructing Kraus operators

Any quantum operation or set of quantum operations can be represented by Kraus operators and the evolution of the system from the initial state to the final state is described as $\rho = \sum_j \mathcal{K}_j \rho_0 \mathcal{K}_j^\dagger$ with the unit trace condition $\sum_j \mathcal{K}_j^\dagger \mathcal{K}_j = 1$. Kraus operators are unique up to a unitary transformation and evolution can also be described by another set of Kraus operators.

For reconstructing Kraus operators for all time delays $t = [1...99]$ we consider the next maximum log-likelihood function

$$ln(\mathcal{L}_{\mathcal{K}}(t_i)) = \sum_{b,s} f(s,b,i) ln(Tr[\rho_s(t_i) M_b]) + \overline{f}(s,b,i) ln(Tr[\rho_s(t_i)(I - M_b)]), \tag{2}$$

where parameters defined as in (1) and $\rho_s(t_i) = \sum_j \mathcal{K}_j \rho_s \mathcal{K}_j^\dagger$.

Non-Markovianity estimation

The non-Markovianity measurement uses the following fact: for any quantum process that can be described by the time-dependent Lindblad master equation that describes the Markovian dynamics

$$\dot{\rho}(t) = -\frac{i}{\hbar}[H(t), \rho(t)] + \sum_i \gamma_i (L_i(t)\rho(t)L_i^\dagger(t) - \frac{1}{2}\{L_i^\dagger(t)L_i(t), \rho(t)\}) \tag{3}$$

with positive decay rates $\gamma_i > 0$ the trace distance $D(\rho_1(0), \rho_2(0))$ between two initial states can only decrease. An increase in the trace distance between states in time means a violation of the equation and the presence of non-Markovian errors, since non-Markovian processes cannot be described by the main Lindblad equation. Based on this observation, the following estimation of the non-Markovian calculation was proposed in [5]

$$N_{markov} = max_{\rho_1(0),\rho_2(0)} \int_{\sigma>0} \sigma(t, \rho_1(0), \rho_2(0)) dt, \tag{4}$$

where $\sigma(t, \rho_1(0), \rho_2(0)) = \frac{d}{dt}(D(\rho_1(t), \rho_2(t)))$.

Results

We have obtained the initial state and POVM matrices for the first qubit of the 5-qubit ibmq_belem quantum computer

$$\rho_0 = \begin{pmatrix} 0.9955 & -0.0061 + 0.0067i \\ -0.0061 - 0.0067i & 0.0045 \end{pmatrix}, M_0 = \begin{pmatrix} 0.9995 & -0.017 + 0.0124i \\ -0.017 - 0.0124i & 0.0307 \end{pmatrix}. \tag{5}$$

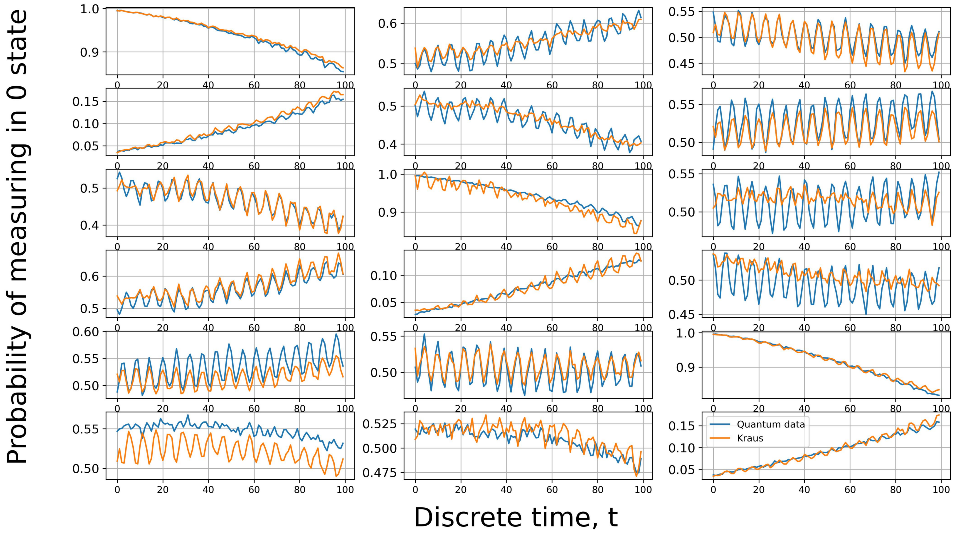

Figure 1: Frequency of measurements in the state $|0\rangle$ obtained from the quantum computer for different depths of the waiting circuit and the estimated frequency at discrete times using SPAM error and sets of Kraus matrices

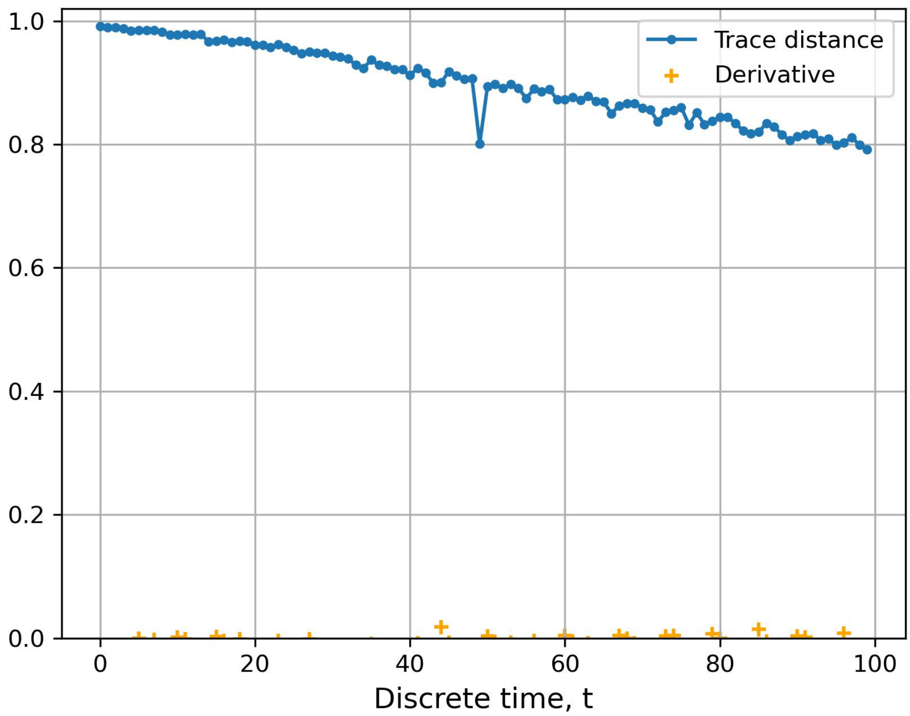

Figure 2: Non-markovianity estimation of the first qubit of ibmq_belem $N_{markov} = 0.30799$

Fig. 1 shows the discrete frequency evolution by Kraus operators. Fig. 2 shows the change of the trace distance for times $t_i = [0...99]$. The estimated value of the non-Markovian measure is a good indicator for an attempt to describe the evolution of a qubit by the Lindblad equation in comparison with the value of the non-Markovianness estimate for a qubit presented in [4].

References

[1] *Sommer O. E., Piazza F., Luitz D. J.*, Many-body hierarchy of dissipative timescales in a quantum computer. Phys. Rev. Research. **3**, 023190 (2021).

[2] *Taylor H. S., Mandelshtam V. A.*, Harmonic inversion of time signals and its applications. J. Chem. Phys. **107**, (1997).

[3] *Wang K., Piazza F., Luitz D. J.*, Hierarchy of relaxation timescales in local random Liouvillians. Phys. Rev. Lett. **124**, 100604 (2020).

[4] *Samach, Gabriel O and Greene, Ami and Borregaard, Johannes and Christandl, Matthias and Barreto, Joseph and Kim, David K and McNally, Christopher M and Melville, Alexander and Niedzielski, Bethany M and Sung, Youngkyu and others*, Lindblad tomography of a superconducting quantum processor. Phys. Rev. Applied **18**, 064056 (2022).

[5] *Breuer, Heinz-Peter, Elsi-Mari Laine, and Jyrki Piilo*, Measure for the degree of non-Markovian behavior of quantum processes in open systems. Phys. Rev. Lett. **103**, 210401 (2009).

Methods of measuring photons re-emitted by single-photon detectors during optical ”backflash” attack on QKD systems

Sergey Bogdanov[1,2*], **Ivan Sushchev**[1,3], **Andrey Klimov**[1]

[1] *Quantum Technology Centre of Moscow State University, Moscow, 119991, Russia*
[2] *National Research University Higher School of Economics, Moscow, 101000, Russia*
[3] *Faculty of Physics, Moscow State University, Moscow, 119991, Russia*
*E-mail: king16061999@gmail.com

Abstract

In order to examine QKD systems for sustainability to the “backflash” attack, it is necessary to measure the probability of photon re-emission and estimate the maximum possible information leakage. However, conventional methods of registration ”backflash” photons are not effective enough. We present experimental setups for measuring backflash photons with polarisation, spectral and time-domain features. Analysis of obtained experimental data demonstrates advantages and drawbacks of each experimental method.

Quantum key distribution (QKD) systems provide a secure exchange of information between legitimate users, guaranteed by the laws of quantum mechanics [1]. Nevertheless, QKD systems may be vulnerable to optical attacks due to the imperfection of the equipment [2]. One of the possible attacks on QKD systems using single-photon avalanche InGaAs detectors is the ”backflash attack” [3]. Since secondary photons are emitted back into the communication channel during events related to the counting of avalanche photodetectors (SPAD), Eve (the eavesdropper) can take advantage of the SPAD vulnerability to reveal the secret key by passively registering photons using a circulator between Alice and Bob’s communication channel, and thus obtain information about the encoded state of light.

However, in classical optical reflectometry method [4], electrical gates are applied to the measuring detector together with each probing laser pulse, which leads to crucial noise during measurement. Moreover, measuring detector registers significant amount of photons reflected from the surface of detector under test. Reflected and backflash photons overlap each other, therefore, it is of a great challenge to distinguish backflash photons and accurately estimate the probability of re-emission. Histogram of backflash and reflected photon is shown in Figure 1. Accordingly, in order to increase signal-to-noise ratio it is necessary to develop new methods of measuring backflash photons.

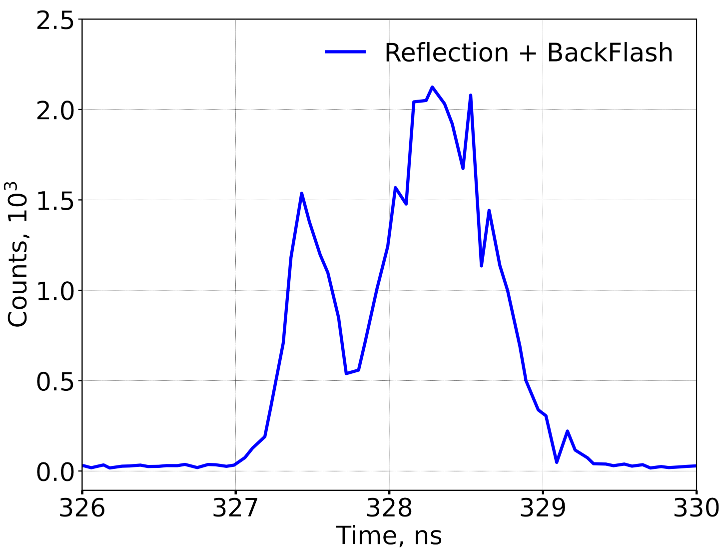

Figure 1: The scheme of correlation “backflash” measurements by optical reflectometry

Firstly, reflected peak could be suppressed by using polarizing filter and polarization controller. However, backflash is unpolarized emission, thus, total amount of backflash emission will drop twice. The scheme of polarizing measurements is shown in Figure 2. Therefore, this method enables to distinguish the reflected peak from the backflash peak and accurately measure the probability of re-emission.

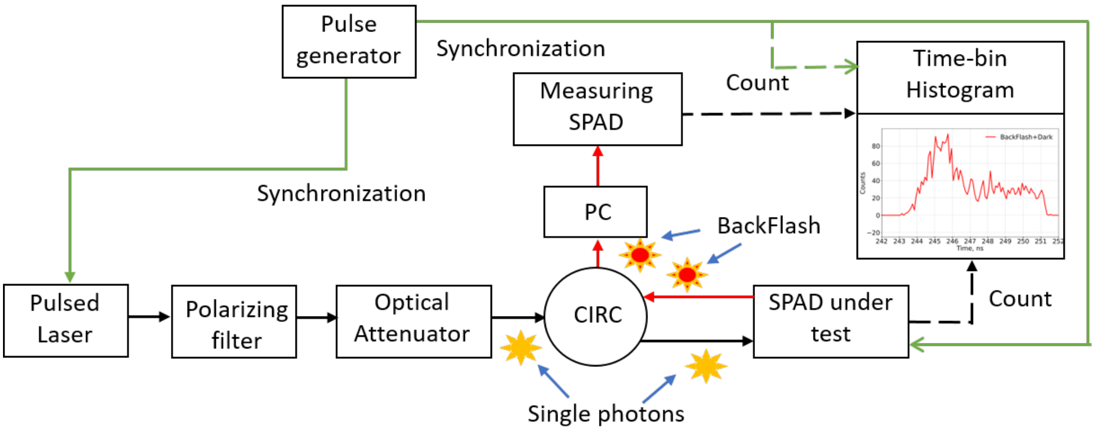

Figure 2: The scheme of “backflash” measurements by optical reflectometry, suppressing reflection by polarization controller and polarizing filter

Another possible method to reduce errors associated with reflection consists in using a CWDM (Coarse Wavelength Division Multiplexer) in the measurement scheme. Therefore, reflected photons with the wavelength of 1550 nm will be suppressed. Since spectrum of backflash is distributed over the entire spectral range of the detector sensitivity, the amount of backflash photons decrease insignificantly. The scheme of the “backflash” measurements by optical reflectometry, suppressing reflection by the CWDM, is shown in Figure 3.

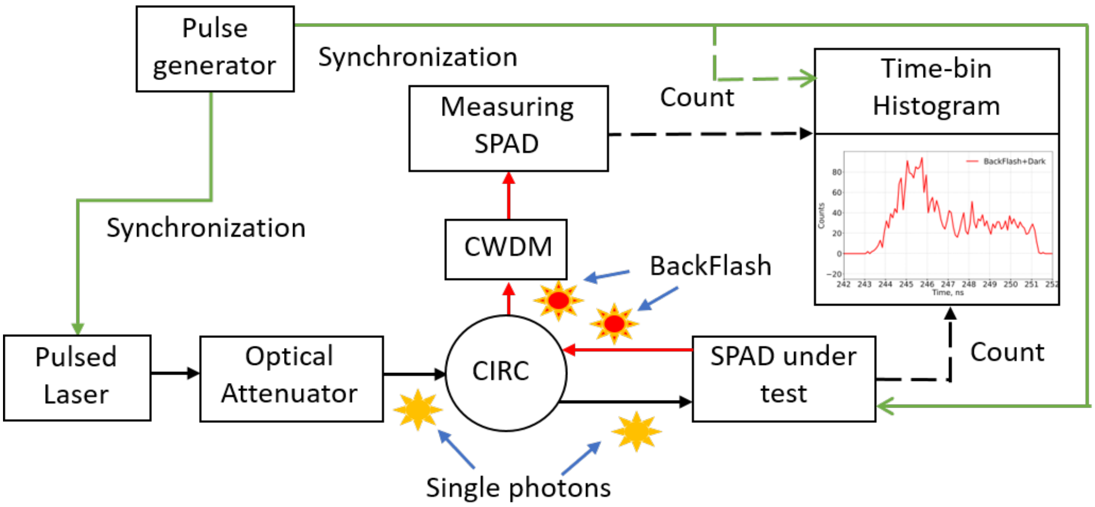

Figure 3: The scheme of the “backflash” measurements by optical reflectometry, suppressing reflection by the CWDM

The time of statistics collection takes a few minutes, however, the measuring SPAD will register 10 re-emitted photons per pulse, which is comparable to the SPAD’s dark noise. In order to increase signal-to-noise ratio and reduce noise and other parasitic readings of the measuring SPAD we suggest to add a time correlator into the measurement scheme [5]. In correlation measurements of the re-emission of a single-photon detector, an electrical gate is applied to the measuring SPAD only if the detector under test is triggered. This increases the signal-to-noise ratio. The scheme of correlation measurements of the re-emission of a single-photon detector by optical reflectometry with a time correlator is shown in Figure 4.

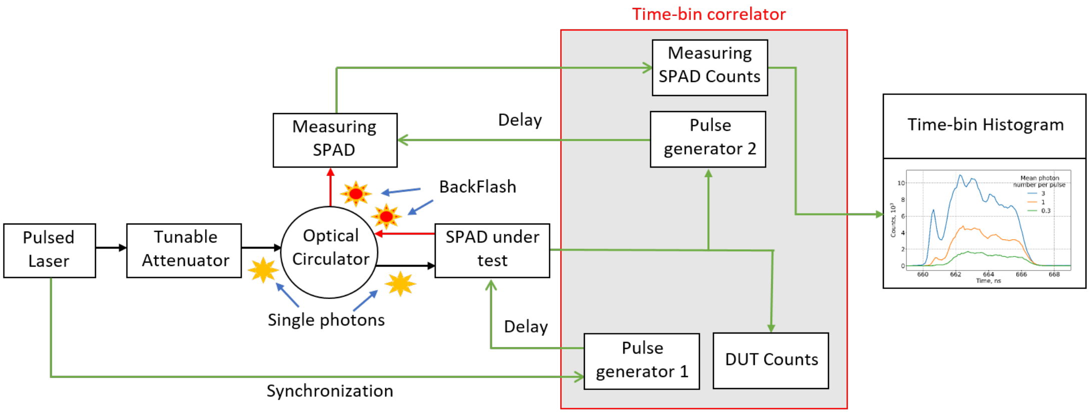

Figure 4: The scheme of correlation "backflash" measurements by optical reflectometry

This correlation measurements method has an important advantage: the contribution of reflected photons depends on the mean photon number per pulse (μ). Since the measuring detector can register photons only if the detector under test is triggered, this measurement method enables to increase the signal-to-noise ratio by at least two orders of magnitude. Furthermore, while using the optimal value of $\mu < 1$, the contribution of reflected photons becomes significantly smaller, and the histograms of reflected and re-emitted photons do not overlap. Thereby it is possible to accurately calculate the probability of "backflash" re-emission.

References

[1] *S. N. Molotkov*, Journal of Experimental and Theoretical Physics, **114**, 168 (2014).

[2] *N. Jain, B. Stiller, I. Khan, D. Elser, C. Marquardt, G. Leuchs*, Contemporary Physics, **57(3)**, 366-387 (2016).

[3] *C. Kurtsiefer*, Journal of Modern Optics **48(13)**, 2039-2047 (2001).

[4] *A. Meda*, Light: Science & Applications, **6**, (2017).

[5] *S. Bogdanov*, SPIE Quantum Technologies 2022, **12133**, (2022).

Method for evaluating the effectiveness of protection measures against laser damage attack of fiber-optical quantum key distribution systems

Bugai K.E.[1,2*], Zyzykin A.P.[1], Bulavkin D.S.[1], Dvoretskiy D.A.[1,2]

[1]*SFB Laboratory, Ltd, Moscow, 127273, Russia*
[2]*Bauman Moscow State Technical University, 2nd Baumanskaya str. 5-1, Moscow, Russia 107005*
*E-mail: `kirillbugajjwork@yandex.ru`

Abstract

We present a method for evaluating measures of protection against the laser damage attack, which can assist the developers make the QKD system more secure. Based on this criterion/method, the resistance to LDA of permanent fiber optic attenuators widely used in QKD fiber optic systems was analyzed.

Introduction

Quantum key distribution (QKD) System provides a secure exchange of information between legitimate users, guaranteed by the laws of quantum mechanics. However, if the eavesdropper (Eve) changes the absorption of the fiber optic attenuator widely used for single-photon state preparation, then the safety of such a system will be at great risk [1]. In Alice, a fiber optical attenuator is usually the last component that interacts with laser radiation before passing through the quantum channel. However, for eavesdroppers, the attenuator is the first component, which can be attacked by high-power laser radiation.

Experimental setup and results

We have developed a method for evaluating the effectiveness of protection measures to assist the designer of QKD systems. Such an approach is an essential element of research, for only by reflecting on practice can development of QKD systems be generated. We have simulated the changing attenuation (Π) and the average number of photons on the probability of the appearance of two photons in a pulse. The simulation graph is shown in Fig. 1a. Such study help designers will be able to determine the changing absorption that will compromise the security of their system. By making a planar section of the graph with the mu used in the quantum protocol, one can determine the threshold for attenuation change, as shown in Fig. 1b.

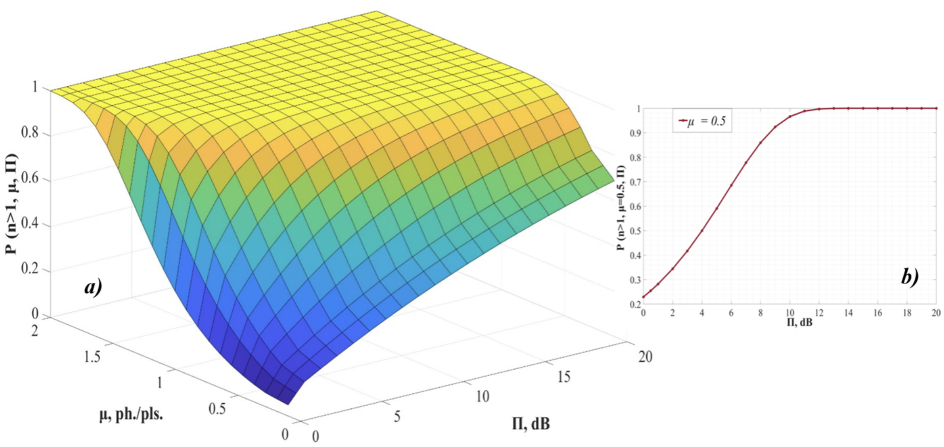

Figure 1: (a) Graph the changing attenuation (Π) and the average number of photons on the probability from the appearance of two photons in a pulse, (b) Graph the changing attenuation (Π) on the probability from the appearance of two photons in a pulse at $\mu = 0.5$

The experimental setup for LDA is shown in Fig. 1. CW laser radiation with a high power up to 5.5 W at a wavelength of 1561 nm is directed along with the fiber to the studied sample of the attenuator (DUT). As a result of DUT heating, the absorption of the attenuator may increase providing single-photon state corruption [1]. To monitor the change in the DUT absorption, another CW laser is installed in the experimental setup at a wavelength of 1547.315 nm. High power coupler of 90/10 was used both to control the 2 laser power (10%) and to transmit laser power to the DUT (90%). High power circulator was used on one hand to deliver the CW high-power radiation to the DUT and another hand to transmit 2 laser power to the detection system after the DUT. The spectral filter (set for the 2 wavelength) is installed in the detection setup to cut off the reflected radiation from the high-power CW laser. The attenuator in front of the SF was used to prevent laser damage from the reflected radiation of the high-power laser. High power optical isolator after LD2 was used to prevent laser seeding effect from high power laser [2]. The fiber fuse effect from high power radiation may occur in the DUT. A fiber spool with 100 m of SMF-28 fiber was added to the setup as protection for high-power laser. Using this experimental setup, the changing attenuation can be calculated using Equation (1).

$$\Pi_i = 10 \log \left(\frac{P_{m.PM1} - P_{m.ref}}{P_{m.st.PM1}} \right), [dB], \tag{1}$$

where

$P_{m.st.PM1}$ – the value of the average power at the receiver PM1 before exposure to powerful laser radiation on the component, W,

$P_{m.ref}$ – the value of the average power that is reflected from the sample, W,

$P_{m.PM1}$ – the value of the average power at the receiver PM1 during exposure to powerful laser radiation on the component, W.

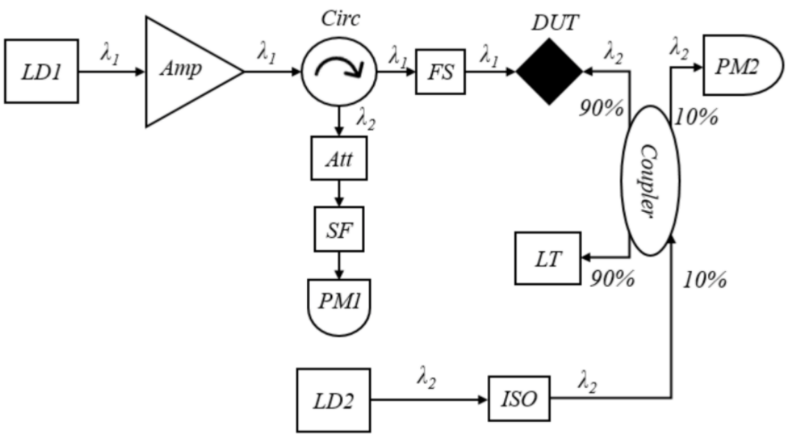

Figure 2: The experimental setup. LD1 — 1 laser diod; Amp — er-doped fiber amplifier, Circ— fiber-optic circulator; FS — fiber spool; Coupler —90/10 fiber optical coupler; PM1, PM2 —power meters; SF— spectral filter, Att — attenuator; ISO —high-power fiber optical isolator; DUT— device under test, LD2 — 2 laser diode; LT - fiber optical light trap

Using this method, we studied the effect of LDA on 3 same pieces of widely used commercially available attenuators with 10 dB absorption, shown in Fig. 3 b. Experimental data on the changing attenuation of the DUT under high-power CW radiation is shown in Fig. 3 a. Using the proposed method, the results obtained show that the change in DUT attenuation, under the influence of high-power radiation, leads to an increase in the probability from the appearance of two photons in a pulse by 11%. Therefore, the 10 dB attenuators used are not resistant to LDA.

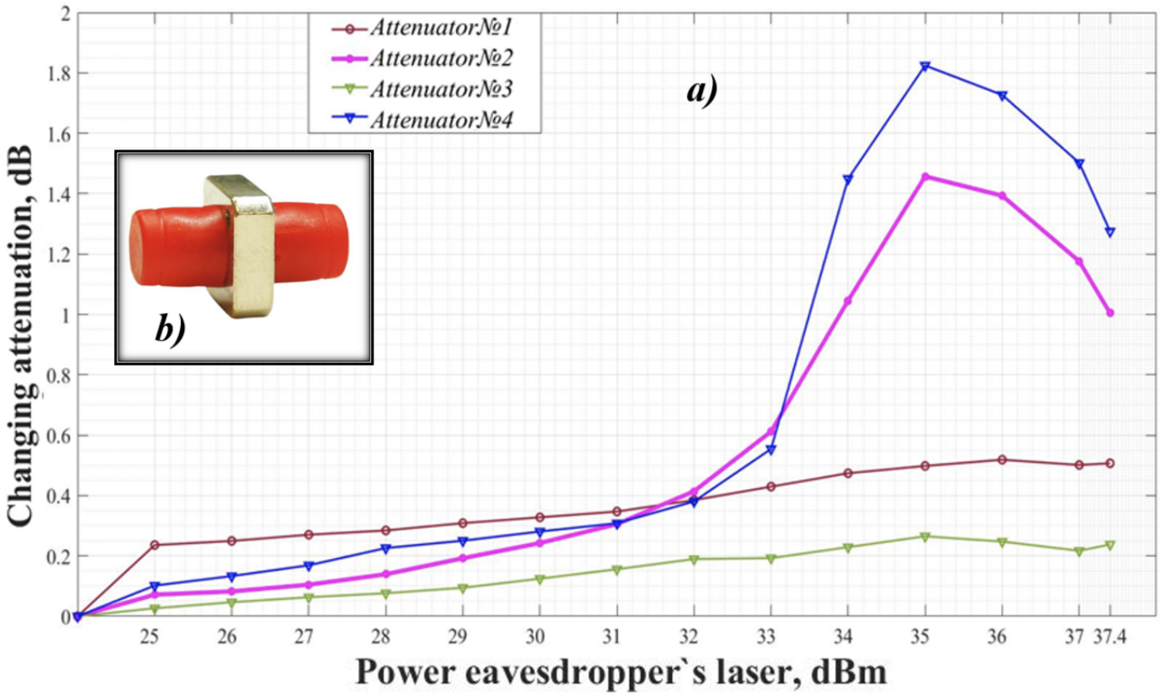

Figure 3: (a) Attenuation deviation of DUT under high-power CW radiation, (b) Image of used 10-dB attenuator

References

[1] *Alferov, S.V., Bugai, K.E., Pargachev, I.A.*, Study of the Vulnerability of Neutral Optical Filters Used in Quantum Key Distribution Systems against Laser Damage Attack. Jetp Lett. **116**, 123–127 (2022).

[2] *Anqi Huang, Alvaro Navarrete, et.al.*, Phys. Rev. Applied 12, 064043 (2019).

Study of single-photon detector blinding attack with modulated bright light

Daniil Bulavkin[1*], **Kirill Bugai**[1,2], **Dmitriy Dvoretskiy**[1,2]

[1] *SFB Laboratory, Ltd, Moscow, 127273, Russia*
[2] *Bauman Moscow State Technical University, 2nd Baumanskaya str. 5-1, Moscow, Russia 107005*
*E-mail: Daniil.Bulavkin@sfblaboratory.ru

Abstract

We present an experimental setup for blinding attack with modulated bright light with the opportunity of changing pulse width in the range of 5-20 ns at various repetition rates. Then we are comparing the conventional defense method via bias current analyses during CW and bright pulse blinding.

Quantum Key Distribution Systems (QKD) provide a secure exchange of information between legitimate users guaranteed by the laws of quantum mechanics. There are many attacks on the conventional components of QKD systems, and one of the most promising and dangerous for whole system security is the blinding attack of single-photon detectors [1]. When blinded, the single-photon detector is switched from Geiger mode to linear mode and, thus, ceases to be sensitive to single photons. This attack can allow the eavesdropper (Eve) to fully control the APD triggering and thereby impose his key [2].

An experimental setup for carrying out the blinding attack is shown in Fig. 1. Laser radiation passes through a polarizer and enters an amplitude modulator based on a Mach-Zehnder interferometer. The phase modulator is connected to a power supply, which brings it to the operating point corresponding to the minimum transmission of the modulator. A signal of a certain shape is fed to the high-frequency output of the modulator, which will set the shape of the optical signal going to the single-photon detector. Then the radiation hits the 90/10 beam splitter. From the 90% output, the radiation enters the wideband 20 GHz photodetector module, which monitors the signal shape. From the 10% output, the laser pulse goes to the attenuator, and from it to the single-photon detector. The single-photon detector is a commercially available device with software and electronics that allows monitoring the detector parameters such as counting rate, bias current, and temperature. The detector operates in gated mode and is synchronized using the signal generator with a frequency of 10MHz. We perform the blinding attack at different pulse widths using a signal generator and monitor the level of bias current. Then, we compare the bias current during CW and pulse single-photon detector blinding. Data depicted in Fig.2 clearly shows that blinding using modulated light causes the rising of the bias current less than CW blinding which proves that bright light pulses are more effective than CW blinding. However, increasing the bias current is enough to be detected if corresponding electronics components would be chosen.

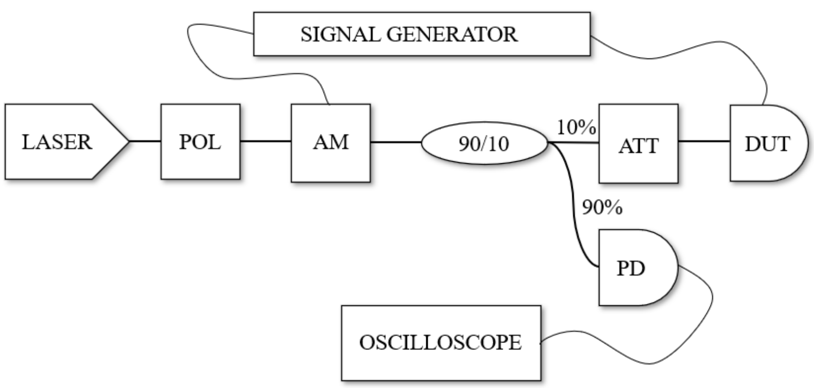

Figure 1: Experimental setup (LASER – 1550nm laser source, POL – polarizer, AM – amplitude modulator, 90/10 – 90/10 optical splitter, ATT – attenuator, PD – wideband photodetector module 20GHz, DUT – single-photon avalanche diode)

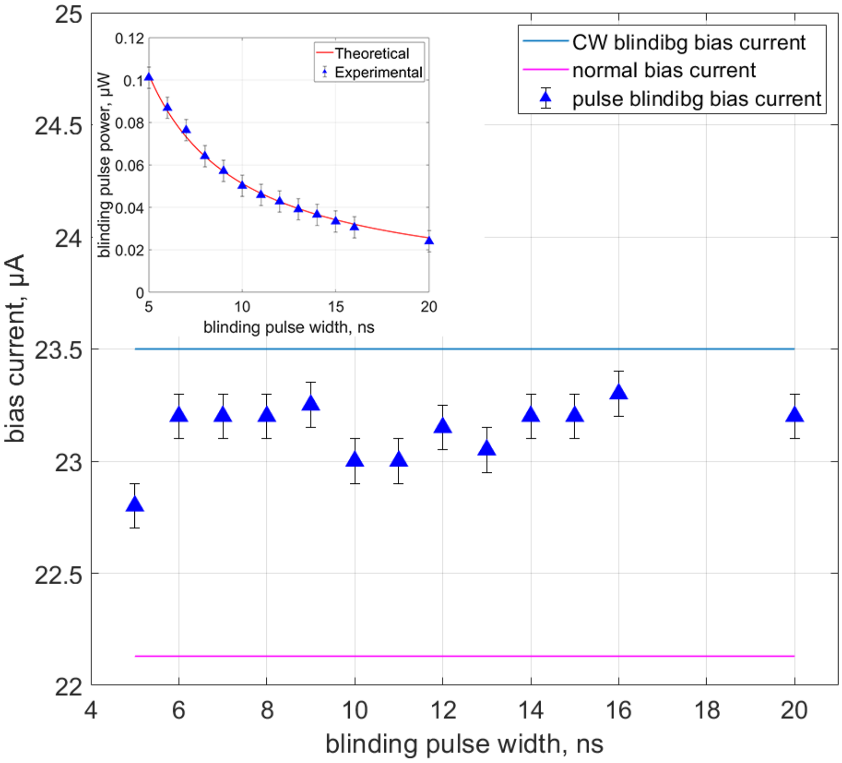

Figure 2: Bias current vs blinding pulse width during CW blinding and modulated blinding against bias current in normal condition of the SPAD. Inserted fig. – comparing of the experimental blinding pulse power dependence on pulse width vs theoretical fitted curve.

The inset of Fig.2 shows the experimental blinding pulse power dependence on pulse width fitted by the theoretical curve. The fitted curve has the form of the hyperbola, which proves that detector-blinding power depends mainly on the energy in the pulse.

References

[1] *1. L. Lydersen, C. Wiechers, C. Wittmann, D. Elser, J. Skaar, and V. Makarov*, Nat. Photonics 4(10), 686–689 (2010).

[2] *2. V. Chistiakov, A. Huang, V. Egorov, and V. Makarov*, Opt. Express 27(22), 32253–32262 (2019).

Investigating Optical Switch Insertion Loss due to Ambient Temperature Changes

Kirill Demkin[1*], Sergei Alferov[1],
Konstantin Stepanov[1]

[1] *"InfoTeCS",Moscow, Russia*
*E-mail: Kirill.Demkin@infotecs.ru

Abstract

Optical losses must be taken into account when designing quantum key distribution networks. In this study, we have examined the insertion losses of an optical switch due to changes in ambient temperature.

Introduction

Switching of optical lines plays an important role in quantum key distribution (QKD) networks. Switching can be achieved in various ways, including using an optical switch. Like any optical element, such a switch has its own optical losses. Losses can be caused by different reasons, including changes in ambient temperature. As is known, the ability to generate shared keys in QKD networks is limited by the insertion losses in the line [1].

Thus, it is crucial to study insertion losses of an optical switch due to ambient temperature changes.

Experiment scheme

The scheme of the experiment is shown in Fig.1. A 1x12 MEMS optical switch was used for the

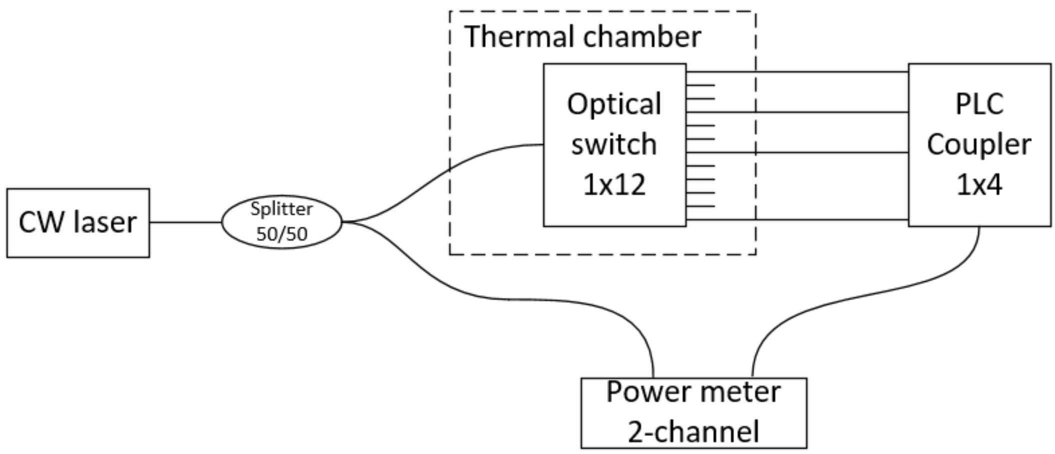

Figure 1: Experiment scheme

study. The switch was conditioned in a thermal chamber at +1 and +40 degrees Celsius. According to the specification, the maximum temperature-induced loss deviation is 0.2 dB. A continuous wave 1550 nm laser was used as the radiation source. The power was measured using a 2-channel power meter. The stability of the laser was controlled by removing a part of the radiation by a 1x2 passive splitter with a 50/50 split ratio. A 1x4 planar coupler (PLC) was used to avoid additional manual re-connection of optical adapters during loss measurement.

Table 1: Initial conditions.

Port number	Initial port loss, dB	1x4 coupler loss, dB	Total power (incl. losses), μW
1	0.45	7.01	1052.5
4	0.36	6.88	1017.2
7	0.6	6.85	975.2
12	0.38	7.00	1032.9

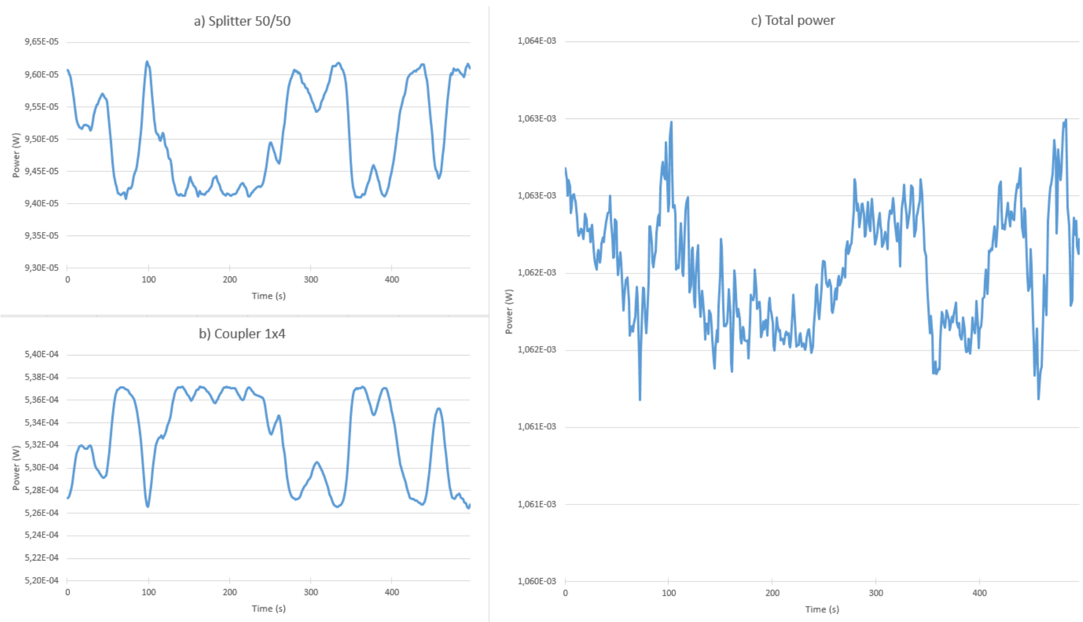

Figure 2: Power at the a) 50/50 splitter output, b) 1x4 coupler output, c) the total power

The average measured losses in the switch ports under initial conditions, the total output power in both channels, as well as the losses on the 1x4 coupler according to the specification are shown in Table 1. The insertion losses for a specific port were calculated by the following formula:

$$\Delta_i = A_i^{cur} - A_{0i} \tag{1}$$

where A_i^{cur} is the current loss value in the specified port (dB), A_{0i} is the initial loss value (dB).

As can be seen from Fig. 2a,b, the radiation power is redistributed, that is, the maximum in one graph corresponds to the minimum in the other. The total power value is more stable (Fig.2c). Indeed, the standard deviation for the first case is 3.78E-6 and 4.11E-6, respectively, while for the total power is 3.76E-7.

The changes in losses after 1-hour temperature stabilization are shown in Fig.3. A positive value in the graph (hereinafter) corresponds to an increase in the insertion loss.

The insertion loss changes (port 1) during 1 hour of temperature increase to +40 degrees are shown in Fig.4. The sharp drops in the graph are probably caused by the changing transmission in detachable optical connections due to the periodic switching on of the thermal chamber compressors.

Conclusion

The change in the losses of all investigated ports is within 0.2 dB as specified by the manufacturer. The observed deviations during 1-hour measurement are most likely caused by the external influence of the vibrating thermal chamber.

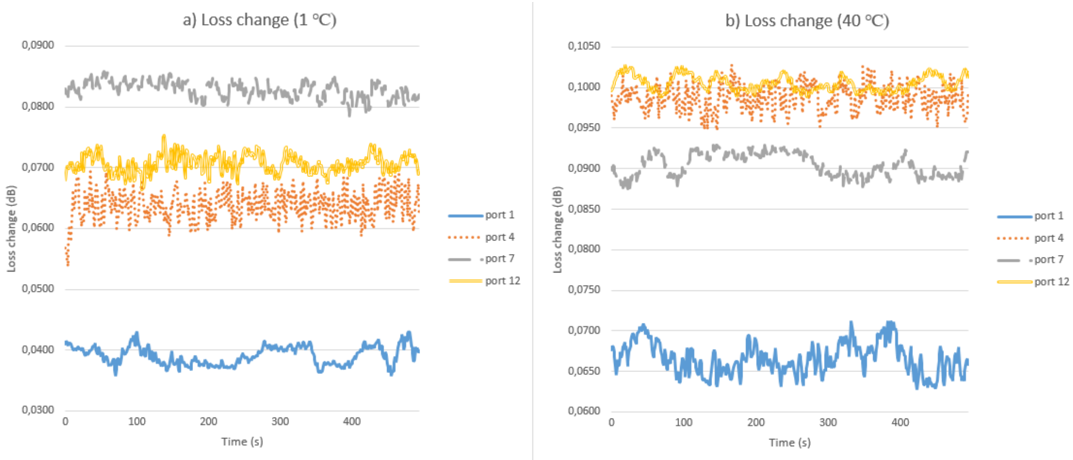

Figure 3: Loss change within 1 minute after temperature stabilization: a) +1 degree, b) +40 degree degree

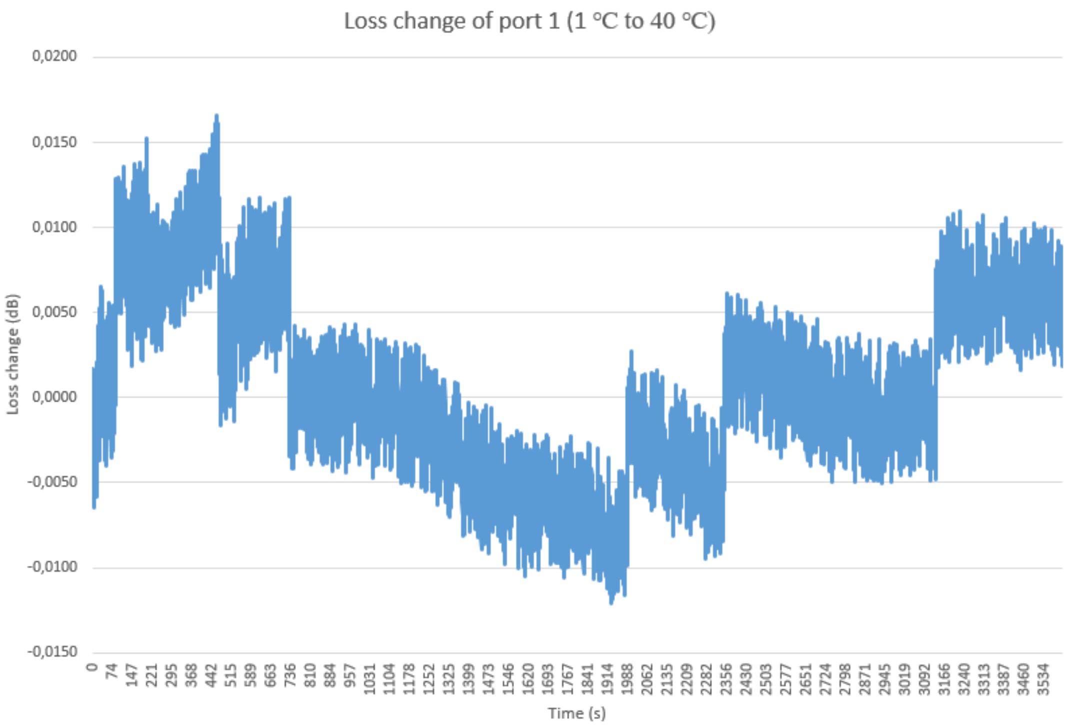

Figure 4: Loss change during 1-hour of temperature increase to +40 degrees

References

[1] *H. Shibata, T. Honjo, K. Shimizu*, Quantum key distribution over a 72 dB channel loss using ultralow dark count superconducting single-photon detectors. Optics Lett. **39**, 5078 (2014).

Semi-empirical model of satellite-to-ground quantum communication

Aleksandr Khmelev[1,2,3,*], Egor Ivchenko[1,2,3], Alexey Duplinsky[3,4], Vladimir Kurochkin[2,3,5]

[1] *Moscow Institute of Physics and Technology, Dolgoprudny, Russia*
[2] *Russian Quantum Center, Moscow, Russia*
[3] *QSpace Technologies, Moscow, Russia*
[4] *HSE University, Moscow, Russia*
[5] *NTI Center for Quantum Communications, NUST MISiS, Moscow, Russia*
*E-mail: aleksandr.khmelev@phystech.edu

Abstract

Large-scale quantum communication have just become a reality as a result of successful satellite quantum communication experiments. Here we present a semi-empirical quantum key distribution (QKD) model between the Micius satellite and our actual ground stations as a more practical method for analyzing the elements of a future quantum network. Based on the measured parameters of ground stations with telescope apertures of 300 mm and 600 mm we have obtained the modeled secret key lengths that differ by 3.2 to 4.6 times for several typical satellite passages. Therefore, the small-scale ground station can be useful for satellite-based QKD experiments.

Quantum communication technology provides a potentially unhackable communication channel for the exchange of encryption keys and also long-term data security [1]. Typically, quantum communications are restricted to a few hundred kilometers and rely on photon states being exchanged through an optical fiber [2, 3]. The idea of using a satellite as a quantum trusted node is proposed to expand the range of quantum communication.

Here, we present a semi-empirical satellite-to ground QKD model for a more realistic analysis of developed ground stations with 0.3 m and 0.6 m telescope apertures. Based on the measured characteristics of an atmospheric channel and optical ground systems, we compare the secure key rate and error rate for both QKD receivers.

Satellite-to-ground communication geometry and link efficiency

To determine channel efficiency in a satellite-based QKD model, we calculate the time-dependent distance $d(t)$ between the transmitter and the receivers, as well as the satellite elevation angle θ_{El} above the horizon. We consider several typical satellite passages and calculate one passing through the zenith in a circular orbit.

Channel losses between a satellite and a ground station dynamically change during quantum communication, which significantly distinguishes this method from fiber optic or terrestrial QKD. In general, diffraction losses vary as the distance between a satellite and a ground station changes. Additionally, varying elevation angles result in varying effective thicknesses of the atmosphere during light transmission.

The diffraction loss can be calculated using the laser source divergence γ, communication channel length d, and effective receiving area with the telescope diameter D_T and obstruction ε of the secondary mirror, as follows $\varepsilon D_T^2/(\gamma d)^2$. Meanwhile, the atmospheric extinction has been estimated via 600-mm ground station. We measure the fluxes of stars with different elevation angles and known magnitudes outside the atmosphere in spectral range (845 nm–855 nm) [4], and defined the atmospheric extinction coefficient $\varkappa$.

Hence, link efficiency, or the overall transmission of photons at 850 nm between the Micius satellite and a ground station, is given by

$$\eta(t) = \frac{\varepsilon D_T^2}{(\gamma d)^2} \cdot 10^{-0.4\varkappa \csc\theta_{El} \cdot (1-0.0012\cot^2\theta_{El})} \eta_{opt}\eta_{det}, \quad (1)$$

where η_{opt} is an optical efficiency of the respective ground station and η_{det} is a quantum efficiency of a single photon detector.

Table 1 summarizes the baseline parameters of the setups required for further modeling.

Table 1: Parameters of the experimental setups for simulating link efficiency between Micius satellite and the ground stations [4]

D_T (mm)	ε	η_{opt}	η_{det}	γ (Rad)	$\varkappa$
300	0.81	0.44	0.55	10^{-5}	0.23–0.34
600	0.73	0.27	0.55	10^{-5}	0.23–0.34

Satellite-to-ground QKD analysis

We simulate a satellite-to-ground QKD experiment using the BB84 decoy-state protocol [5]. We determine the sifted key rate (SKR) and quantum bit error rate (QBER) of the designed receivers. Then, we estimate the secret key length by applying data post-processing for signal state QKD.

Figure 1 presents the simulated QKD characteristics for signal intensity pulses during the satellite passage with a peak elevation angle of 32.5° and for the theoretical zenith passage. Table 2 shows the length of the input sifted keys and the estimated length of the secret keys throughout the time of Δt.

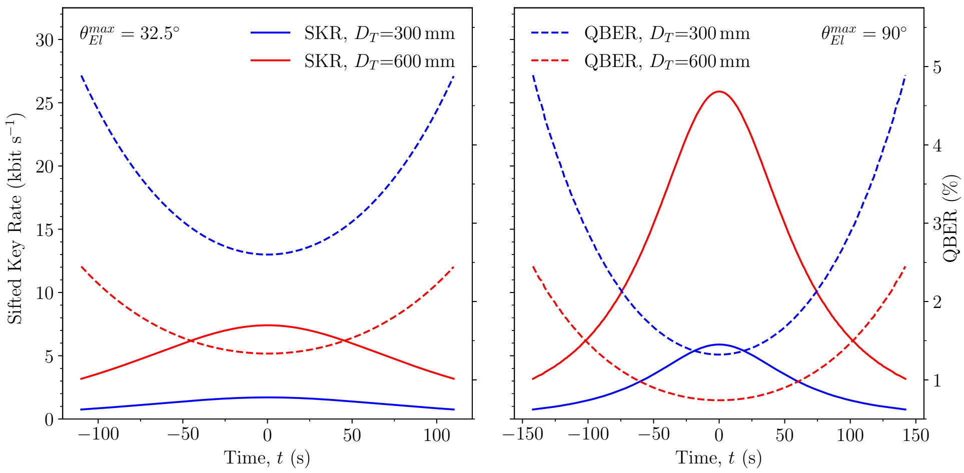

Figure 1: Modelled sifted key rate and QBER of signal states during the satellite passage above a ground station on October 31, 2021 and during the zenith satellite passage. The computations are carried out for clear weather conditions and for elevation angles greater than 20°.

Table 2: Sifted key length vs secret key length (SKL) for practical receivers in simulated satellite-to-ground QKD experiment. Calculation presented for the 300 mm / 600 mm ground stations.

Passage	Sifted Key Length (kbit)	SKL(kbit)
2021-10-31 ($\theta_{El}^{max} = 32.5°$, Δt =221 s)	547 / 1207	40 / 182
2021-03-23 ($\theta_{El}^{max} = 42°$, Δt =260 s)	859 / 1897	101 / 357
2021-03-09 ($\theta_{El}^{max} = 57.5°$, Δt =283 s)	1263 / 2790	187 / 600
Zenith passage ($\theta_{El}^{max} = 90°$, Δt =285 s)	1586 / 3505	260 / 803

We applied the model to our ground stations and analyzed the secure key generation performance with Micius satellite based on the features of our ground stations and measured air losses. The secret key lengths of ground stations with 300 mm and 600 mm apertures differ by 3.2 to 4.6 times, while consider typical satellite passages with different peak elevation angles, whereas telescope areas differ by four times. It demonstrates that small-scale ground stations can be useful for satellite-based QKD experiments.

This work was supported by the Ministry of Education and Science of the Russian Federation in the framework of the Program of Strategic Academic Leadership "Priority 2030" (Strategic Project "Quantum Internet").

References

[1] *V. Scarani, H. Bechmann-Pasquinucci, N.J. Cerf, M. Dušek, N. Lütkenhaus and M. Peev*, The security of practical quantum key distribution. Rev. Mod. Phys. **81**, 1301 (2009).

[2] *J.-P. Chen, C. Zhang, Y. Liu, C. Jiang, W. Zhang, X.L. Hu, J.-Y. Guan, Z.-W. Yu, H. Xu, J. Lin, M.-J. Li, H. Chen, H. Li, L. You, Z. Wang, X.-B. Wang, Q. Zhang, and J.-W. Pan*, Sending-or-Not-Sending with Independent Lasers: Secure Twin-Field Quantum Key Distribution over 509 km. Phys. Rev. Lett. **124**, 070501 (2020).

[3] *M. Pittaluga, M. Minder, M. Lucamarini, M. Sanzaro, R. Woodward, M.-J. Li, Z. Yuan, and A. Shields*, 600-km repeater-like quantum communications with dual-band stabilization. Nature Photonics **15**, 1 (2021).

[4] *A.V. Khmelev, A.V. Duplinsky, V.L. Kurochkin and Y V Kurochkin*, Stellar calibration of the single-photon receiver for satellite-to-ground quantum key distribution Journal of Physics: Conference Series **2086**, 012137 (2021).

[5] *X. Ma, B. Qi, Y. Zhao, and H.-K. Lo*, Practical decoy state for quantum key distribution. Phys. Rev. A **72**, 012326 (2005).

Investigating the feasibility of balanced detector blinding attacks in Continuous-Variable Quantum Key Distribution systems

Polina Morozova*, **Boris Nasedkin**

Laboratory of Quantum Communications, ITMO University, St. Petersburg, Russia
*E-mail: pamorozova@itmo.ru

Abstract

The study examines the vulnerability of the balanced detector in quantum key distribution systems due to limitations in electronic components. It experimentally determines the relationship between average intensity values and applied radiation power, and identifies the saturation threshold and level of noise in the signal. The findings can aid in identifying potential blinding attacks and provide insight into defense strategies.

Introduction

The importance of secure data transfer cannot be ignored in today's world, for which various methods are utilized. One of the most promising methods is Quantum Key Distribution (QKD) systems, which provide secure encryption key transfer at a fundamental level. These systems allow two remote parties, commonly referred to as Alice and Bob, to establish a secret key over a public quantum channel through classical communication [1]. However, there are various vulnerabilities in quantum networks that can be exploited by intruders, potentially compromising the encryption key transmission. QKD systems based on continuous variables rely on coherent detection, using a device such as a balance detector.

Balanced Detector

The focus of this study is on the security of the balance detector (BD), a critical component in quantum key distribution systems. The BD comprises both optical and electronic components. The aim is to address potential vulnerabilities and identify strategies for defense against potential attacks [2]. The main source of electronic noise in the balanced detector (BD) is attributed to thermal noise in the transimpedance amplifier (TIA) circuit. To accurately detect quantum signals, the BD must distinguish shot noise from electronic noise. The dispersion of the BD output signal is a measure of shot noise, which is determined by observing its linear dependence on the power of the local oscillator (LO) [3]. Electronic noise is determined by comparing it to the dispersion of shot noise in the absence of a quantum signal applied to the BD.

Blinding attack

A blinding attack aims to saturate the balance detector by sending high-power radiation to its signal port or local oscillator. The experiment measured the dependence of average intensity value on power and dispersion value, i.e. excessive noise, a key parameter in monitoring CV-QKD. The result of the experiment measurements is shown in the Fig. 1. At a power of around 7 μW, the balanced detector switches from linear to nonlinear operation, causing photocurrent to exceed permissible levels and leading to saturation of the electronics, also known as blinding of the balance detector and appearance of vulnerabilities. If the balanced detector reaches saturation mode when an intruder intervenes, and legitimate users will measure the variance, then there is a chance that according to their data, the excess noise is below the threshold value, which means that everything is sort of fine, and the users will accept the compromised keys. The intruder, on the other hand, can listen to the classic channel, which is needed to match the post-processing, in order to copy the the same post-processing on their data to get identical keys.

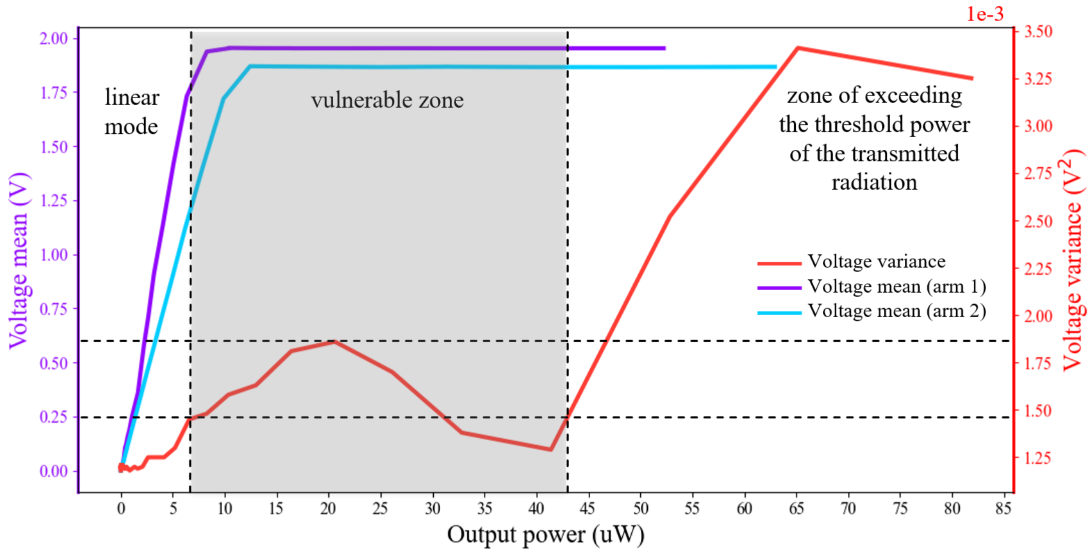

Figure 1: Illustration of balanced detector in a saturation mode with the formation of a vulnerable zone caused by linear mode boundary crossing the dispersion line

References

[1] *J. Nitin, H. Chin, H. Mani, C. Lupo, D.S. Nikolic, A. Kordts, S. Pirandola, T.B. Pedersen, M. Kolb, B. Ömer, C. Pacher, T. Gehring and U.L. Andersen*, Practical continuous-variable quantum key distribution with composable security. Nature communications **13.1**, 4740 (2022).

[2] *H. Qin, R. Kumar and R. Alléaume*, Quantum hacking on a practical continuous-variable quantum cryptosystem by inserting an external light. In Electro-Optical and Infrared Systems: Technology and Applications XII; and Quantum Information Science and Technology **9648**, (2015).

[3] *X. Tang, R. Kumar, S. Ren, A. Wonfor, R.V. Penty and I.H. White*, Performance of continuous variable quantum key distribution system at different detector bandwidth. Optics Communications **471**, 126034 (2020).

[4] *H. Qin, R. Kumar, V. Makarov and R. Alléaume*, Homodyne-detector-blinding attack in continuous-variable quantum key distribution. Physical Review A **98.1**, 012312 (2018).

Spectral dependence of Trojan horse attack on a subcarrier wave QKD system

Boris Nasedkin[1*,2], **Fedor Kiselev**[2,3], **Andrei Gaidash**[1,3,4], **Anton Kozubov**[1,3,4], **Vladimir Egorov**[2,3]

[1] *Laboratory of Quantum Processes and Measurements, ITMO University, Saint Petersburg, Russia*
[2] *Laboratory for Quantum Communications, ITMO University, Saint Petersburg, Russia*
[3] *SMARTS-Quanttelecom LLC, Saint Petersburg, Russia*
[4] *Department of Mathematical Methods for Quantum Technologies, Steklov Mathematical Institute of Russian Academy of Sciences, Moscow, Russia*
*E-mail: banasedkin@itmo.ru

Abstract

In these paper we considered affect of chosen wavelanght at possibility of Trojan-horse attack in 1500–2100 nm spectral range. We showed that insertion losses of investigated system strongly affect at Trojan-horse attack possibility. We also showed that affection of photon number per pulse and photon number at sidebands compensate each other in 1500–2100 nm.

Introduction

Quantum communications systems are protected by fundamental physical laws. Nevertheless it is possible to use loopholes of equipment to extract information about distributed bit sequence. Searching of such loopholes is an area of quantum hacking. One on the powerful ways to extract information about distributed bit sequence is Trojan-horse attack [1, 2]. For realisation of these attack, eavesdropper send to Alice's or Bob's system scanning pulses which interact with optical parts of system. For example such pulses may interact with phase modulator when the process of state settings is on, and then reflect back to eavesdropper. Eavesdropper can find such wavelength which reflect back with minimal attenuation comparing with another available wavelengths. To close that loophole, possibility of Trojan horse attack investigated in 1000–1800 nm range [3, 4]. Nevertheless it was shown that Trojan horse attack possible beyond these range [5]. In these work we analysed possibility of Trojan horse attack in 1500–2100 nm.

Results

Corresponding to [6] one can assume possibility of Trojan horse attack realisation against subcarrier QKD [7] as:

$$\chi(\mu) \approx h\Big(\frac{1-e^{-2\mu}}{2}\Big), \tag{1}$$

where $h(x) = -x\log_2(x) - (1-x)\log_2(1-x)$ is binary entropy function, and μ is the mean photon number of all sidebands in the spectrum.

Mean photon number can be estimated as:

$$\mu_p = \ M \cdot N \cdot 10^{\frac{T}{10}} \tag{2}$$

where M is mean photon number at side bands, N is number of photons per pulse with with fixed frequency of state changing for maximal possible power of scanning pulses (10 W) and T is insertion losses of investigated system.

One can find that not only insertion losses of system T has spectral dependence but also M and N. And if N depends only on wavelength chosen as scanning, M strongly depends on phase modulator material.

As an investigated material we choose lithium niobate which is one of the mostly used materials in fiber phase modulators. Number of photons at sidebands depends on applied on crystal voltage and for the same voltage it is different for different wavelengths. To limit our calculations we investigate affect of listed parameters for 1500–2100 nm spectral range.

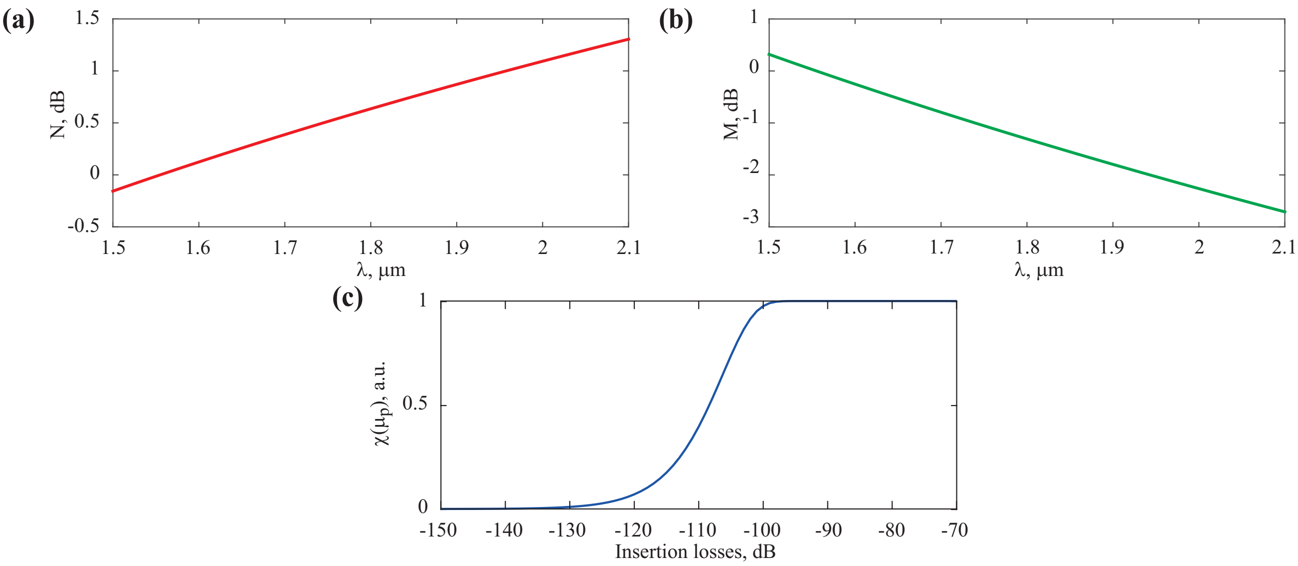

Figure 1: a) Spectral dependence of photon number mean per pulse, b) spectral dependence of photon number at sidebands c) Holevo bound evaluated for mean photon number of an output probe beam, μ_p (**??**), dependent on insertion losses

In Figure 1 a and b we showed wavelengths dependence for photon number per pulse and photon number at side bands presented in dB relatively to 1550 nm as 0 dB. We used such presentation to simplify our calculations and use data as an amendment to insertion losses. Photon number per pulse is increase and photon number at side bands decrease with wavelahght. In Figure 1 c we presented calculated Holevo bound. For insertion losses < -130 dB Trojan-horse attack is impossible and for > -100 dB permit to eavesdropper to get full information about distributed bit sequence.

Conclusion

Insertion losses of investigated system strongly affect at Trojan-horse attack possibility. Affection of photon number per pulse and photon number at sidebands compensate each other in 1500–2100 nm. Trojan horse attack is possible for meaning of insertion losses > -100.

The study was partially funded by the Ministry of Education and Science of the Russian Federation (Passport No. 2019-0903).

References

[1] *A. Vakhitov, V. Makarov, D.R. Hjelme*, Large pulse attack as a method of conventional optical eavesdropping in quantum cryptography. Journal of modern optics. **48**, **13**, 2023–2038 (2001).

[2] *N. Gisin, S. Fasel, B. Kraus, H. Zbinden, and G. Ribordy*, Trojan-horse attacks on quantum-key-distribution systems. Phys. Rev. A. **73**, 022320 (2006).

[3] *N. Jain, B. Stiller, I. Khan, V. Makarov, C. Marquardt, and G. Leuchs*, Risk analysis of Trojan-horse attacks on practical quantum key distribution systems. IEEE Journal of Selected Topics in Quantum Electronics **21**, 168–177 (2014).

[4] *A.V. Borisova, B.D. Garmaev, I.B. Bobrov, S.S. Negodyaev, and I.V. Sinil'shchikov*, Risk Analysis of Countermeasures Against the Trojan-Horse Attacks on Quantum Key Distribution Systems in 1260–1650 nm Spectral Range. Optics and Spectroscopy. **128**, **11**, 1892–1900 (2020).

[5] *I.S. Sushchev, D.M. Guzairova, A.N. Klimov, D.A. Dvoretskiy, S.A. Bogdanov, K.D. Bondar, and A.P. Naumenko* , Practical security analysis against the Trojan-horse attacks on fiber-based phase-coding QKD

system in the wide spectral range. Emerging Imaging and Sensing Technologies for Security and Defence VI. **11868**, 57–63 (2021).

[6] *S. Sajeed, C. Minshull, N. Jain, and V. Makarov*, Invisible Trojan-horse attack. Sci. Rep. **7**, 1-7 (2017).

[7] *G.P. Miroshnichenko, A.V. Kozubov, A.A. Gaidash, A.V. Gleim, and D.B. Horoshko*, Security of subcarrier wave quantum key distribution against the collective beam-splitting attack. Optics express. **26**, **9**, 11292–11308 (2018).

[8] *S. Sajeed, P. Chaiwongkhot, A. Huang, H. Qin, V. Egorov, A. Kozubov, A. Gaidash, V. Chistiakov, A. Vasiliev, amd A. Gleim*, Security of subcarrier wave quantum key distribution against the collective beam-splitting attack. Sci. Rep. **11**, **1**, 1–16 (2021).

Relevant attacks on quantum key distribution systems

Ivan Sushchev[1,2,3*]

[1] SFB Laboratory, Ltd, Moscow, 127273, Russia
[2] Quantum Technology Centre of Moscow State University, Moscow, 119991, Russia
[3] Faculty of Physics, Moscow State University, Moscow, 119991, Russia
*E-mail: Ivan.Sushchev@sfblaboratory.ru

Abstract

Quantum key distribution systems (QKD) are able to provide data transmission security guaranteed by the fundamental laws of physics. Nevertheless, real systems can be subject to a number of attacks, which become possible both due to the peculiarities of the transferred quantum states and imperfect technical implementation of such systems. To achieve secrecy during key distribution, it is necessary to take these attacks into account and equip the system with protection by adding active and passive optical elements to it, as well as modifying the quantum protocol. The examination of attacks on QKD systems is carried out during certification works. This report highlights the relevant attacks on QKD systems, the methods of protection against them and the main approaches to security analysis of QKD systems.

Quantum key distribution (QKD) systems can theoretically provide unconditionally secure key sharing between two parties, often called Alice and Bob, guaranteed by laws of quantum mechanics [1, 2]. However, practical imperfections in the implementation of such systems make it necessary to verify that an eavesdropper (Eve) is not able to steal the secret key exploiting security loopholes [3]. Here I provide a survey of the relevant attacks on QKD systems.

The straightforward way to attacking the QKD system consists in a ”Man-the-Middle” strategy which only operates with the quantum states in the communication channel. The simplest example is the Intercept-Resend attack in which Eve carries out measurements on the individual quantum states the same way as Bob. She encodes the measurement outcome in new quantum states and eventually deliver them to Bob. Such attack represents no threat for BB84 protocol and alike as far is being accompanied by quantum bit error rate (QBER) rise. Moreover, the information gain is not optimal for an adversary, so the Translucent, the Collective and the Joint attacks take place [4] (see Fig. 1). It is known that the collective attack provides the maximum information gain for BB84 protocol. Despite being detected by QBER rise, such attack serves as a foundation for conducting and, hence, accounting for side channel attacks.

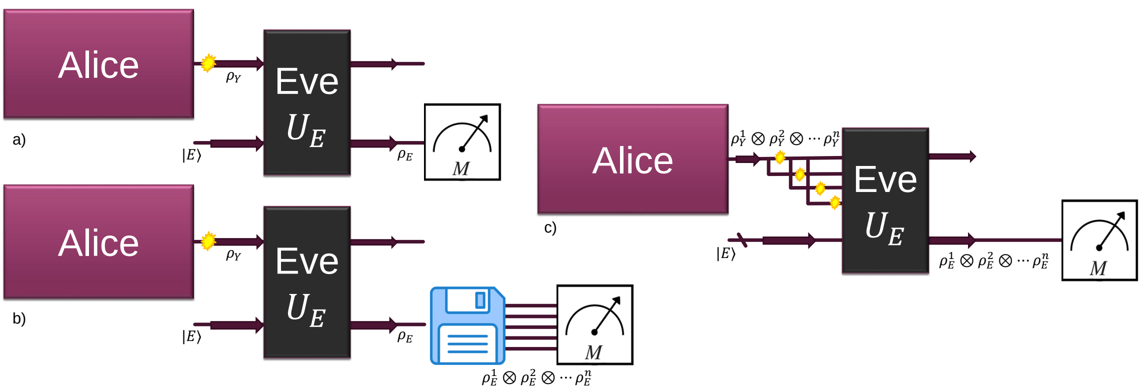

Figure 1: The Translucent (a), the Collective (b) and the Joint attack (c). Each line represents a qubit, the crossed line is a set of qubits. The M-labeled device represent a measurement station, the floppy disk is the quantum memory.

An implementation of weak coherent pulses (WCPs) instead of single-photon radiation leads to another class of attacks, known as the Photon Number Splitting (PNS) attack and the Beam-Split (BS) attack. These attacks consider the different ways of splitting the legitimate radiation remaining invisible. To mitigate such atacks one must consider proper protocol modifications, such as the Decoy-State method [5]. Note that today the complete implementation of the PNS and BS attacks seems unrealistic since the quantum memory and no-loss optical channel are not invented yet.

Another class of attacks is based on utilization of side channels. These attacks let Eve to identify a portion of a secret key measuring the state of an auxiliary quantum system, i.e. a side channel state, thus, avoiding the rise of QBER. Such attacks are the Trojan Horse attack (THA) [6], the Backflash attack (BFA) [7], and the attack based on measuring the radio emission from electronic apparatus. In absence of proper defensive measures these attacks represent a critical threat to communication security. A set of optical elements (such as optical isolators, circulators, bandpass filters, watchdog detectors, etc.) and protocol modifications must be applied to a QKD systems to avoid them.

The attacks aimed to impose the Bob's measurement outcomes belong to the Fake States attacks (FSA) class. They usually exploit the single photon detectors based on single photon avalanche diodes (SPADs) vulnerabilities. It appears that the SPADs become sensitive to classical radiation under certain conditions, which makes them vulnerable to such attacks as continuous and pulsed Detector Blinding attack (DBA) [8], the Aftergate (AG) attack and the Detector Efficiency Mismatch (DEM) attack. Unlike the side-channel attacks, it is usually impossible to mitigate FSA by means of communication protocol, therefore, specific technical measures, such as the SPAD current monitoring, must be implemented.

Finally, there exist a type of preliminary attacks aimed to change the properties of Alice or Bob station affecting the magnitude of states departing from Alice or Bob station (both legitimate WCPs and gained from THA or BFA) or Bob's measurement probabilities. These are the Laser Damage attack (LDA) [9] and the Laser Seeding attack (LSA) resulting in either permanent or reversible damage of optical elements inside the QKD system. It gives Eve an opportunity to succeed, for instance, in PNS attack, BS attack, THA or BFA. It is important to make sure that the QKD system is sustainable to high power radiation for these attacks to fail.

In conclusion, there is a variety of attacks on QKD systems. To ensure the secure communication each of them must be taken into account. Implementing the proper defensive mechanisms and subsequent certification checkup are necessary for every QKD system to provide unconditional security of quantum communication.

References

[1] *S. N. Molotkov*, Journal of Experimental and Theoretical Physics, **114**, 168 (2014).

[2] *M. A. Nielsen and I. L. Chuang*, Quantum Computation and Quantum Information (2000).

[3] *N. Jain*, Contemporary Physics, **57:3**, 366-387 (2016).

[4] *S. N. Molotkov*, JETP Letters, **111**, 653-661 (2020).

[5] *Z. W. Yu*, Physical Review A., **88 6** (2013).

[6] *I. Sushchev*, Proceedings of SPIE, Emerging Imaging and Sensing Technologies for Security and Defence VI, **11868** (2021).

[7] *S. Bogdanov*, Proceedings of SPIE, Quantum Technologies, **12133** (2022).

[8] *D. Bulavkin*, Proceedings of SPIE, Quantum and Nonlinear Optics IX, **12323** (2022).

[9] *K. Bugai*, International Conference Laser Optics 2022, 1-1, (2022).

Multi-mode delay interferometer for phase-encoded QKD over free-space channels

Vladislav Tretiakov[1*], **Konstantin Kravtsov**[1]

[1] *MSU Quantum Technology Centre, 119991 Moscow, Russia*
*E-mail: tretiakov.vv18@physics.msu.ru

Abstract

Quantum key distribution (QKD) is a quantum communication protocol based on principles of quantum mechanics, information carriers in which are quantum objects such as photons. Implementations of QKD utilizing fiber communication lines are widespread. The phase encoding is commonly used in such lines. Meanwhile, in free-space channels, polarization-encoded protocols are usually used due to their relative implementation simplicity and robustness of polarization in free-space propagation. It would seem to be impractical to use a phase encoding across free-space channels due to distortions of temporal and spatial modes of photons during propagation through an atmospheric turbulence. Here, we investigate free-space delay interferometer which performs passive optical correction of multi-mode signal. So far we have observed the visibility ≈ 95 % for single-mode signal and ≈ 93 % for multi-mode signal, which allows us to believe that practical QKD implementation with this interferometer is possible. Also we show that the interference visibility for a multi-mode signal is relatively independent of the length of the multi-mode fiber at the input of the interferometer.

Introduction

Quantum key distribution (QKD) [1] is a method of sharing secret keys between two legitimate parties involved in the communication process. QKD over fiber communication channels has achieved great results and QKD experiments over 421 km fiber were demonstrated [2]. However, there is a fundamental limitation in increasing of communication distances over optical fiber due to its internal losses. Free-space QKD experiments are usually based on polarization-states protocols, since they are simple to implement and the polarization is almost not affected by the atmospheric turbulence.

Considering free-space quantum channels it is important to note that the implementation of polarization-state protocols implies quantum measurements to be conducted directly in the free-space channel, consequently the receiving telescope can not be separated from the measurement device by significant distances. However, sometimes it's convenient to collect signal after the receiving telescope into an optical fiber and transmit it to the place where it can be comfortably measured. Either single-mode or multi-mode optical fiber can be used for this purpose. In the first case, it's appeared to be impractical to collect into a single-mode fiber the signal which is distorted by atmospheric turbulence, because a large loss level occurs. In the second case we need to refuse from polarization-states protocols because information about the polarization is lost when signal enters a multi-mode fiber. A convenient alternative to them is a phase encoding [4]. However, commonly used delay interferometers don't allow to obtain required interference visibility with a multi-mode signal.

Here we investigate a multi-mode free-space delay interferometer for analyzing phase-encoded photons. Such interferometer can be used in implementation of QKD protocols based on phase encoding. Experiments on visibility measurements with such an interferometer have been already conducted [3]. However, the delay value was only 2 ns, meanwhile we demonstrate free-space delay interferometer with the delay equal 5.7 ns. There are some limitations (lower bounds) on the delay time due to multi-mode dispersion, which leads to broadening of pulses propagating through the multi-mode fiber. So the phase encoding QKD implementations over installed multi-mode fiber communication lines is another purpose of this research.

Experimental setup

Experimental setup of our multi-mode free-space delay interferometer is depicted in the Fig. 1.

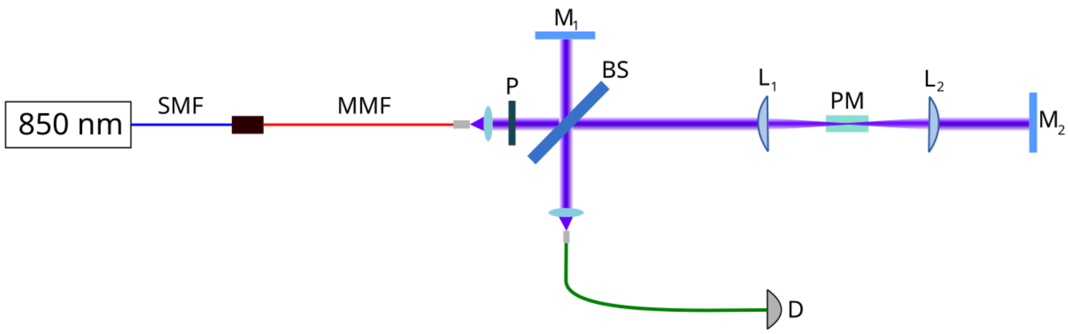

Figure 1: Schematic experimental setup. We used CW laser at the wavelength 850 nm, SMF - single-mode fiber, MMF - multi-mode fiber, P - polarizer, BS - beamsplitter, M_1, M_2 - flat mirrors, L_1, L_2 - thin lenses, PM - phase modulator, D - detector

The main feature of this delay interferometer is a presence of 4f-scheme in its long arm, which induces the correction of the multi-mode signal's wavefront and leads to indistinguishability of two arms of the interferometer for different spatial modes. It was shown in [3] that an unbalanced delay interferometer without any additional optics does not possess such feature. Distinguishability or indistinguishability of interferometer's arms means the absence or presence of the interference visibility respectively.

It can be mathematically shown that in the paraxial approximation the 4f-scheme is equivalent to a flat mirror located in the focal plane of the lens L_1, so this delay interferometer effectively becomes the balanced Michelson interferometer providing all distances are matched correctly (Fig. 2).

Interference visibility

This type of interferometer has been already investigated [3] by Jin *et al*, and the interference visibility was $V_{single} \approx 0.91$, $V_{multi} \approx 0.89$. Here we demonstrate that it is possible to obtain higher values of visibility. Also for the best of our knowledge it has not been yet shown that the visibility does not depend on the length of a multi-mode fiber at the input of interferometer, so the next step is to investigate this dependence. Such research is important beacause this interferometer is supposed to be at a distance of tens or hundreds of meters from the receiving telescope. The results of this research are presented in the table 1

Table 1: Values of interference visibility for different lengths of the fiber at the input of free-space delay interferometer.

Fiber	Visibility
Single-mode	0.95±0.01
Multi-mode ø50 um, 1 m	0.93±0.01
Multi-mode ø50 um, 25 m	0.93±0.01
Multi-mode ø50 um, 50 m	0.92±0.01
Multi-mode ø50 um, 100 m	0.93±0.01

This results show that the visibility is relatively independent of the length of a multi-mode fiber at least at the distances of hundred meters, so this interferometer can be separated from the receiving telescope, which is very convenient for a practical implementation of QKD protocols over free-space channels.

So far we have connected single-mode and multi-mode fibers directly, but in real applications in free-space quantum cryptography it is supposed that a signal passes a turbulent atmosphere and only after that it is collected into a multi-mode fiber. So the question is: will we observe the same interference visibility if we introduce an atmospheric channel into our experimental setup? To answer this question

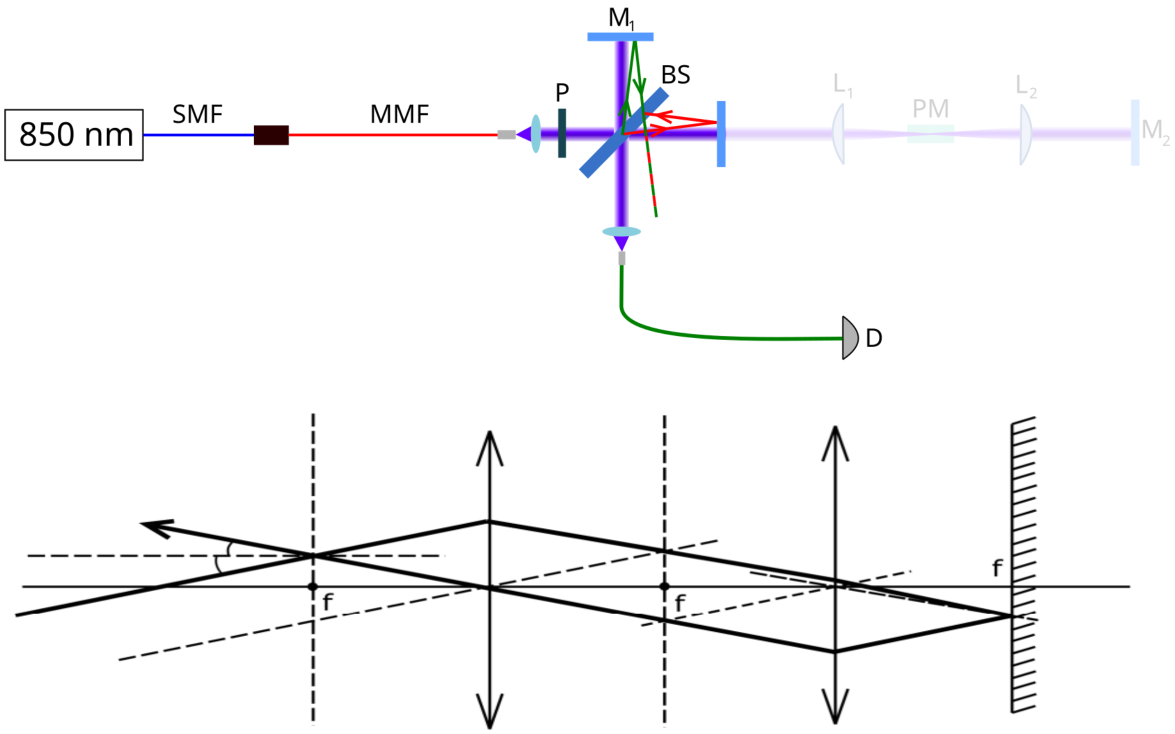

Figure 2: The role of the 4f-scheme in the setup: it reconstructs a wavefront in the focal plane of the lens L_1, so we obtain balanced Michelson interferometer, but it is still a delay interferometer, which is important for an implementation of the QKD phase encoding protocols.

we used a turbulator, which simulates the presence of the atmosphere. So we are going to carry out such an experiment and to perform the results on the 6th International School on Quantum Technologies.

References

[1] C. H. Bennett and G. Brassard. Quantum cryptography: Public key distribution and coin tossing. In *Proceedings of IEEE International Conference on Computers, Systems, and Signal Processing*, page 175, India, 1984.

[2] Alberto Boaron, Gianluca Boso, Davide Rusca, Cédric Vulliez, Claire Autebert, Misael Caloz, Matthieu Perrenoud, Gaëtan Gras, Félix Bussières, Ming-Jun Li, Daniel Nolan, Anthony Martin, and Hugo Zbinden. Secure quantum key distribution over 421 km of optical fiber. *Phys. Rev. Lett.*, 121:190502, Nov 2018.

[3] Jeongwan Jin, Sascha Agne, Jean-Philippe Bourgoin, Yanbao Zhang, Norbert Lütkenhaus, and Thomas Jennewein. Demonstration of analyzers for multimode photonic time-bin qubits. *Phys. Rev. A*, 97:043847, Apr 2018.

[4] Xiao-Tian Song, Dong Wang, Xiao-Ming Lu, Da-Jun Huang, Di Jiang, Li-Xian Li, Xi Fang, Yi-Bo Zhao, and Liang-Jiang Zhou. Phase-coding quantum-key-distribution system based on sagnac–mach-zehnder interferometers. *Phys. Rev. A*, 101:032319, Mar 2020.

Active basis choice for Quantum Key Distribution with Entangled States

Vinetskaya Polina[1,2*], **Kravtsov K.S.**[1,2]

[1] *MSU Quantum Technology Centre, Moscow, Russia*
[2] *HSE, Moscow, Russia*
*E-mail: polinvin@gmail.com

Abstract

BBM92 is one of the most well-known entangled-based quantum cryptography protocols. This work discusses the use of active basis choice and time multiplexing as BBM92 implementation modifications that reduce the number of detectors, considers the use of time shift attacks as applied to entangled-based protocols, and also proposes an optimal implementation scheme.

In addition to the common prepare-and-measure quantum key distribution method, there is an approach based on the transmission and analysis of entangled pairs, first described in the Ekert protocol [1]. Such protocols are not susceptible to source substitution [2] and provide security against individual attacks [3]. One of these protocols is BBM92, which is an analogue of BB84, but its implementation uses 8 single-photon detectors (Fig. 1), which makes its use impractical compared to the prepare-and-measure protocols.

An effective way to reduce the number of detectors is active basis choice, which consists in using electro-optical crystals such as lithium nobate as polarization modulators (Fig.2). The interlocutors randomly choose one of the 2 measurement bases by applying the appropriate voltage to the crystals and changing the polarization of the photon in their subspace. This allows to reduce the number of detectors in the BBM92 scheme to 4.

There is also a modification that uses, in addition to the active choice of the basis, time multiplexing. There are implementations of prepare-and-measure protocols using time-multiplexing [4], but this approach can also be applied to entanglement-based protocols [5]. After passing through the phase modulator, the signal enters the polarizing beam splitter and the part that has passed along the upper path is delayed (Fig. 3). The pieces then unite in the coupler and hit the detector, so Alice and Bob can identify the measured bit by the arrival time of the pulse. Such an implementation, despite all the advantages, is of dubious efficiency, since it may be vulnerable to a timing attack, which has also been described only for prepare-and-measure protocols. In this work, its application to entangled-based protocols was studied and an implementation resistant to it was proposed.

Methods

For all the described variants of the implementation of the BBM92 protocol, the actions on the state generated by the source were described and the probabilities of detecting different states were calculated. Also, the principle of the time-shift attack was described applicable to entangled-based protocols and the analysis of the probabilities of measurement by the interlocutors showed the effectiveness of this attack in a scheme using time multiplexing. As an alternative, a protocol with active polarization state choice has been proposed, which also consists only two detectors (Fig.4). Interlocutors not only choose basis but also a polarization state by choosing one of 4 phase shifts. It has been shown that the probability distribution in this case is similar to the original implementation of BBM92. At the same time, the absence of time multiplexing does not allow using the time-shift attack.

Results

Departing from the BBM92 protocol in its original implementation, realization of the protocol based on electro-optical modulation technique has been described and discussed extensively; typical relevant values of the voltages to be aplied to the crystals were estimated. In this case, it was shown that the active basis choice is an effective way to modify the implementation of the protocol, since it does not affect the probabilities of detecting various states and decreases the number of detectors in scheme. It was also shown that the time-shift attack can be adapted to protocols on entangled states, which makes the use of time-multiplexing impractical, since Eve in this case can receive complete information about the final key. An scheme for active choice of the polarization state was proposed, which allows implementing the BBM92 protocol using 2 detectors in the scheme, and at the same time is not vulnerable to time-shift attack.

Figures

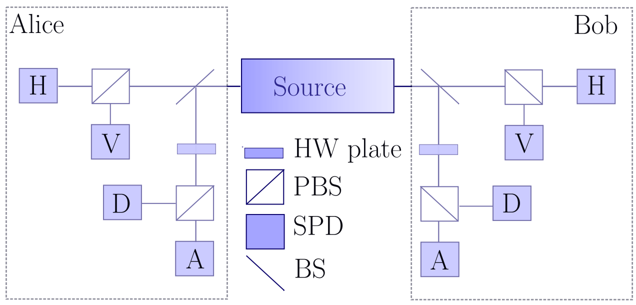

Figure 1: BBM92 circuit with passive basis choice. PBS – polarized beamsplitter, SPD – single photon detector, BS – symmetrical beamsplitter

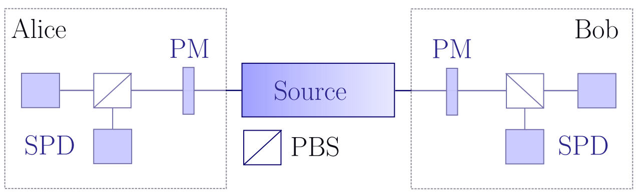

Figure 2: BBM92 with active basis choice

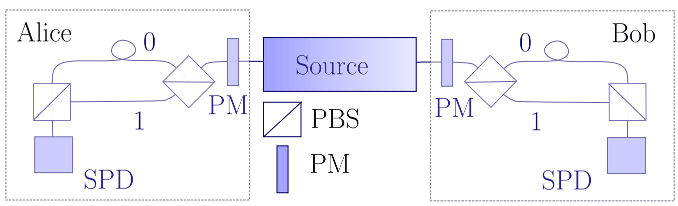

Figure 3: Time-multiplexing scheme

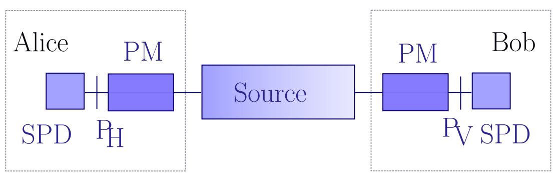

Figure 4: BBM92 with active polarization state choice

References

[1] A. Ekert, "Quantum Cryptography Based on Bell's Theorem", *Phys Rev Lett*, vol. 67, no. 6, pp. 661–663, Aug 1991.

[2] N. M. CH Bennett, G Brassard, "Quantum cryptography without Bell's theorem", *Phys Rev Lett*, vol. 68, no. 5, pp. 557–559, Feb 1992.

[3] E. Waks, A. Zeevi, Y. Yamamoto, "Security of quantum key distribution with entangled photons against individual attacks", *Phys Rev A*, vol. 65, p. 052310, Apr 2002, doi:10.1103/PhysRevA.65.052310.

[4] C. Marand, P. D. Townsend, "Quantum key distribution over distances as long as 30 km", *Opt Lett*, vol. 20, no. 16, pp. 1695–1697, Aug 1995, doi:10.1364/OL.20.001695.

[5] M. Peev, S. Bettelli, "QKD arrangement", US Patent 8,189,966, May 29 2012.

Comparison of Gaussian and vortex beams in free-space QKD with phase encoding in turbulent atmosphere

Iurii Adam[1], **Daniil Yashin**[2],
Daria Kargina, Boris Nasedkin

St. Petersburg National Research University of Information Technologies, Mechanics and Optics, St.Petersburg, Russia
E-mail: adam_yura@mail.ru[1], dayashin@itmo.ru[2]

Abstract

In this work, the use of vortex beams in the free-space QKD system with phase encoding under the condition of a turbulent atmosphere and their comparison with Gaussian beams are studied. Numerical simulations of signal transmission for two types of carriers in different turbulence conditions are obtained. The possibility of phase modulation preservation with additional modulation and demodulation of the vortex beam is also shown.

Introduction

Currently, there are many QKD protocols that encode information using various characteristics of electromagnetic radiation. Thus, the most commonly used QKD protocols in free space are based on polarization states of light. Despite the prevalence of this approach, it has a number of significant drawbacks. Firstly, such systems require the use of elements of the QKD complex that ensure the preservation of radiation polarization, which reduces the commercial potential of such systems. Secondly, systems based on polarization coding do not provide spatial invariance of the orientation of receiving and transmitting telescopic devices used for input/output of radiation from optical fiber, which requires the introduction of additional methods of compensation for polarization rotation, complicating the system and limiting its performance. As an alternative to the method described above it was proposed to use a phase coding protocol that removes the presented limitations and is used, for example, in a subcarrier wave QKD system [1]. An important feature of all QKD systems using an atmospheric communication channel is the effect of scattering particles and atmospheric turbulence on the propagating radiation, expressed in the maximum transmission range shortage and the key generation rate drop. A measure to counteract this problem can be the use of vortex beams as information carriers, for example, Laguerre-Gaussian modes, which are characterized by greater stability when propagating in free space compared to Gaussian beams [2].

Numerical simulation results

The theoretical model of the propagation process of a signal representing a vortex beam of radiation in an atmospheric turbulent channel is based on the method of random phase screens [3] in the approximation of static turbulence (it is assumed that the turbulence parameters do not depend on time and are constant over the entire length of the propagation channel). The evaluation of the parameters of the QKD system was carried out in accordance with the developed model of the process of subcarrier wave quantum key distribution [4]. The theoretical model takes into account the contribution of losses from the Mie scattering in the atmosphere, depending on the visibility conditions [5], and also considers geometric losses during signal detection, due to the "wandering" of the beam as a consequence of turbulence. Beams at the source plane are depicted on Fig. 1; The results of propagation simulation are presented on Fig. 2

As the object of study the subcarrier wave quantum key distribution (SCW QKD) system were chosen [1], the free-space implementation of which is described in [3]. The study of the parameters of this system, as well as their description, are detailed in [4].

It is worth noting that the propagation of quantum signals from the sender to the receiver is considered in the approximation of the classical description. In this work we do not consider the quantum effects such as quantum entanglement, quadrature and photon number squeezing, precisely described in [2, 5]. This approximation was made on the basis of the fact that the protocol used in the SCW QKD system is

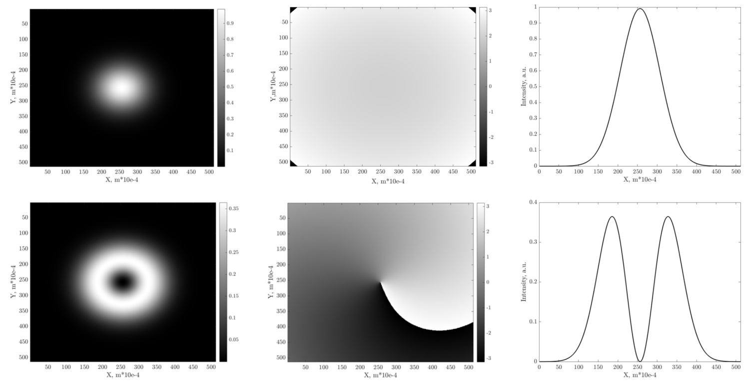

Figure 1: Laguerre-Gaussian modes. Columns show intensity distributions, phase fronts and beam profiles of Gaussian beam (Top) and Laguerre-Gaussian first mode (Bottom) at the source plane

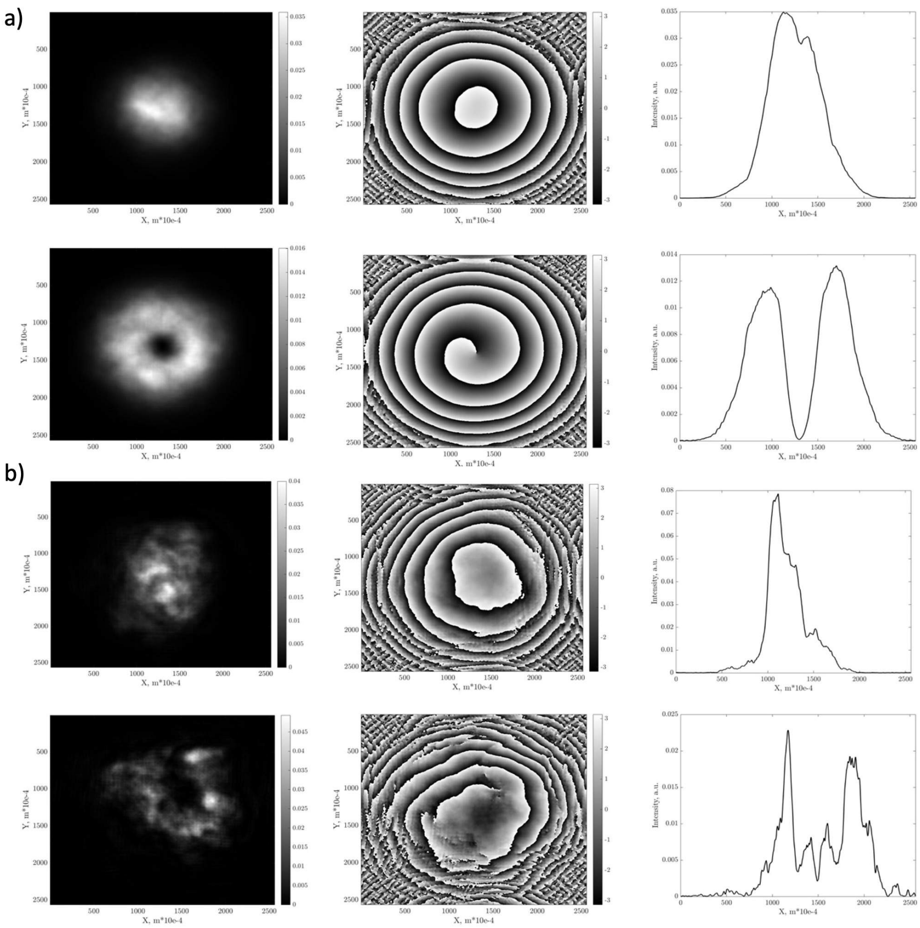

Figure 2: Intensity distribution, phase distribution and intensity profile in the detector plane of Gaussian beam and vortex beam at the distance L = 1000 m from the source plane in case of a) r_C = 1 m; b) r_C = 0.1 m

Table 1: The results of the study of the shift of the Gaussian and vortex beams' centers during the propagation through a turbulent atmosphere at a distance $L = 1000$ m

	r_C, m	Average shift, mm	RMS shift deviation, mm
Gaussian Beam	1	8.5	± 6.5
Vortex Beam	1	3.3	± 1.2
Gaussian Beam	0.1	47.5	± 25.6
Vortex Beam	0.1	19.2	± 12.0

based on the use of attenuated laser pulses - coherent states (obeying Poisson statistics), which are not strictly single-photon states (constituting the Fock basis). Numerical estimation of QKD parameters is shown on Fig. 3, 4

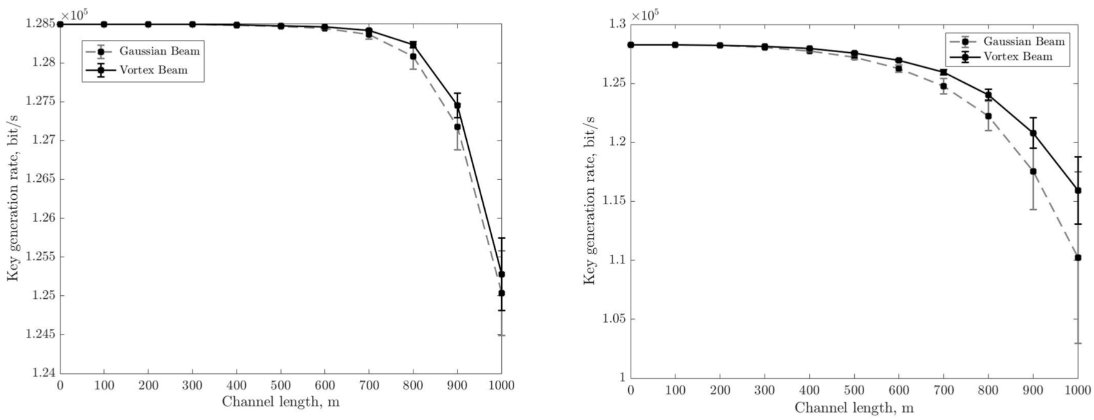

Figure 3: Dependence of key generation rate in an atmospheric communication channel on its length for $r_C = 1$ m (Left), $r_C = 0.1$ m (Right)

These results are in complete agreement with the beam wandering and channel losses estimates. Since the key generation rate and QBER are related to the amount of losses in the communication channel, it is natural that there is a slight advantage with respect to these parameters as well. For $r_C = 1$ m numerical curves for key generation rate and QBER are almost indistinguishable: the difference of mean values for given beams is small and standard deviation values are nearly equal, despite the fact that the vortex beam shows slightly better results. However, more significant advantage can be seen in conditions with $r_C = 0.1$ m. Average key generation rate for vortex beam is about 5% higher than for Gaussian beam at $L = 1000$ m and its standard deviation is noticeably less. Numerical results for QBER, however, shows less difference between the Gaussian and vortex beams, but may be more significant at longer distances, which requires further studies.

Experimental scheme and results

To study the possibility of phase modulation preservation during the transition from a Gaussian to a vortex beam and vice versa in the QKD system on phase coding, an experimental setup was implemented. The purposed scheme is a classic Mach-Zehnder interferometer, in one of the arms of which modulation and demodulation of vortex beam were realized. It is important to clarify that the proposed scheme is not a full-fledged QKD system, but it only imitates the process of phase coding in the classical approximation, however, the results obtained in this work will also be valid for a full-fledged quantum communications system.

In the purposed scheme shown in Fig. 6, the He-Ne laser module (LM) with the wavelength of 633 nm were used. This wavelength has already been used in several works on free-space QKD [6, 7, 8] due to the simplification of the alignment process. The optical radiation was directed to the beamsplitter (BS1), after which the first laser beam entered the phase modulator (PM), where it acquired a delay of

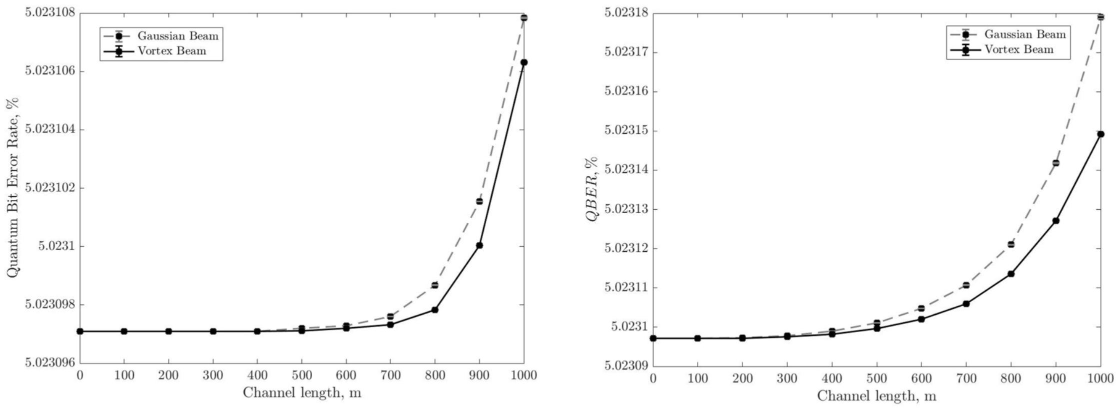

Figure 4: Dependence of QBER in an atmospheric communication channel on its length for $r_C = 1$ m (Left), $r_C = 0.1$ m (Right)

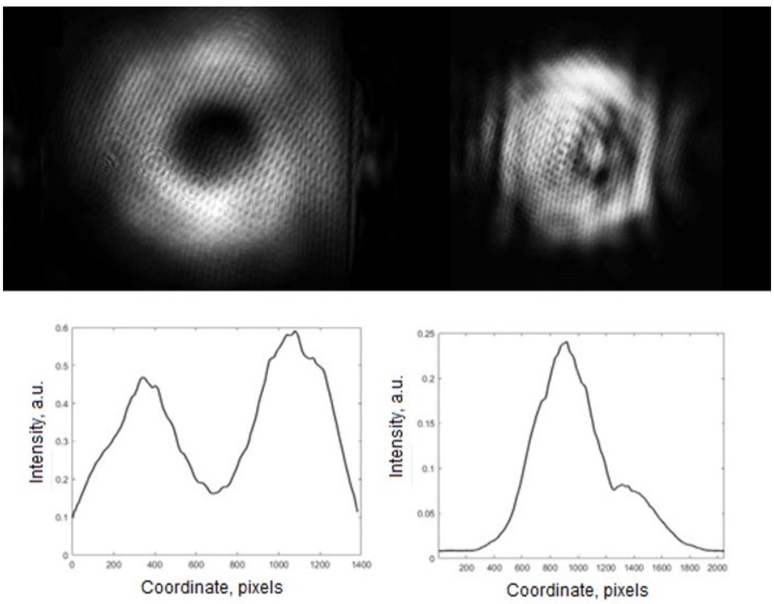

Figure 5: (top left) Profile of a vortex beam modulated on the fork-grating; (bottom left) cross section of the modulated vortex beam; (top right) profile of the Gaussian beam demodulated on the fork-grating; (bottom right) cross section of the demodulated Gaussian beam

0 or π radians, and the second laser beam by the mirror (M1) was directed to beamsplitter (BS2) on the exit of interferometer. Next, the first beam went through the described above process of modulation and demodulation of the optical vortex on two fork-gratings (FG1 and FG2). The distance between these gratings was 42 cm and the first-order diffraction angle was 1.8 degrees. As a result, the obtained demodulated Gaussian beam by the mirror (M2) was directed to beamsplitter (BS2) on the exit of interferometer, where it interfered with the second beam. The interference pattern was recorded using a camera (C) placed at one of the outputs of the beamsplitter (BS2). The intensity profiles of the obtained interference patterns at different values of the phase delay, which were additionally averaged over 60 frames to compensate the phase fluctuations in the interferometer, are shown in Fig. 7. From the obtained results, it can be seen that the value of the introduced phase delay is equivalently reflected in the recorded interference pattern. As a result, it can be concluded that the process of modulation and demodulation of the optical vortex does not affect the process of phase encoding and can be used in the QKD systems with phase encoding.

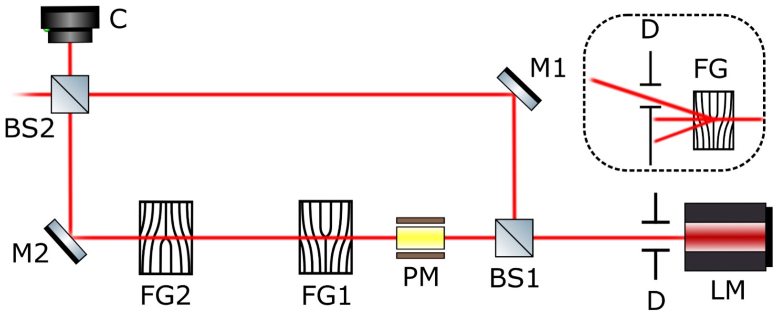

Figure 6: Mach-Zehnder interferometer on demodulated vortex beam; (in the dotted frame) selection of the first order diffraction on fork-grating

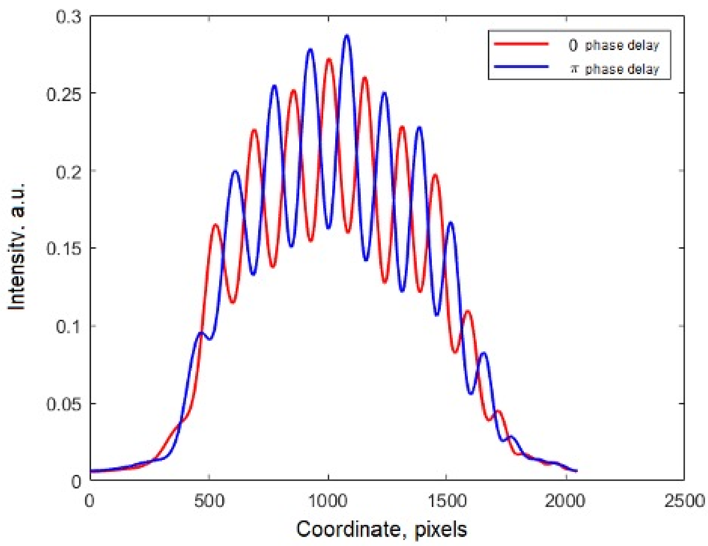

Figure 7: Cross section of the interference pattern at a phase delay of 0 and π radians, averaged over 60 frames

References

[1] *A. Gleim, V. Egorov, Y. V. Nazarov, S. Smirnov, V. Chistyakov, O. Bannik, A. Anisimov, S. Kynev, A. Ivanova, R. Collins,* et al., "Secure polarization-independent subcarrier quantum key distribution in optical fiber channel using bb84 protocol with a strong reference," *Optics express*, vol. 24, no. 3, pp. 2619–2633, 2016.

[2] *D. Y. Vasylyev, A. Semenov, and W. Vogel*, "Toward global quantum communication: beam wandering preserves nonclassicality," *Physical review letters*, vol. 108, no. 22, p. 220501, 2012.

[3] *S. M. Kynev, V. V. Chistyakov, S. V. Smirnov, K. P. Volkova, V. I. Egorov, and A. V. Gleim,* "Free-space subcarrier wave quantum communication," *Journal of Physics: Conference Series*, vol. 917, no. 5, 2017.

[4] *G. P. Miroshnichenko, A. V. Kozubov, A. A. Gaidash, A. V. Gleim, and D. B. Horoshko*, "Security of subcarrier wave quantum key distribution against the collective beam-splitting attack," *Optics Express*, vol. 26, p. 11292, apr 2018.

[5] *M. Faleeva and I. Popov*, "Entanglement transmission through turbulent atmosphere for modes of gaussian beam," *Quantum Information Processing*, vol. 19, no. 2, pp. 1–9, 2020.

[6] *J.-P. Bourgoin, B. L. Higgins, N. Gigov, C. Holloway, C. J. Pugh, S. Kaiser, M. Cranmer, and T. Jennewein*, "Free-space quantum key distribution to a moving receiver," *Optics Express*, vol. 23, no. 26, p. 33437, 2015.

[7] *A. Conrad, S. Isaac, R. Cochran, D. Sanchez, B. Wilens, A. Gutha, T. Rezaei, D. J. Gauthier and P. Kwiat*, "Drone-based quantum key distribution: QKD," *Proc. SPIE, Free-Space Laser Communications XXXIII*, 11678, 116780X (2021). *doi: 10.1117/12.2582376.*

[8] *A. D. Hill, J. Chapman, K. Herndon, C. Chopp, D. J. Gauthier, and P. Kwiat*, "Drone-based quantum key distribution," *Urbana*, vol. 51, pp. 61801–63003, 2017.

Schrödinger cat states of a certain parity from continuous variable gate with non-Gaussian resource state: mixed output state and fidelity.

Baeva A.V.*, **Sokolov I.V.**

St Petersburg State University, 7/9 Universitetskaya nab., 199034, St. Petersburg, 199034 Russia
*E-mail: alexandrabaeva@mail.ru

Abstract

Shrödinger cat states in the form of two high-fidelity "copies" of the target state on the phase plane can be obtained using a quantum measurement-induced gate based on entanglement with the ideal cubic phase state used as a non-Gaussian resource [N.I. Masalaeva, I.V. Sokolov, Phys. Lett. A **424**, 127846 (2022)]. In our work, we use a non-ideal cubic phase state generated from a finitely squeezed state as a resource and present an exact solution for the output state of such a logical element. We consider a more realistic case where the output state is mixed due to the acceptance interval, and analyze the fidelity of this state with an "ideal" cat state.

In recent years, the quantum information theory of continuous variables systems (CV) has been actively developing, both theoretically and experimentally, especially in the context of Gaussian states [1–4], which naturally arise in quantum optics. However, there are situations in which Gaussian operations are not sufficient. To achieve universal quantum computing, it is necessary to introduce non-Gaussian logical elements [1, 2]. They naturally occur due to the nonlinearity of the system. At the same time, the minimal nonlinearity sufficient for the preparation of non-Gaussian resource states is cubic.

In our work, we consider a logical gate based on quantum entanglement and projective homodyne measurement [5, 6], for which the simplest non-Gaussian resource can be a cubic phase state generated by cubic nonlinearity [7]. The key feature of such a gate is that the measurement result of the ancillary oscillator provides multivalued information about the canonical variables of the output state, which means it allows one to generate Schrödinger cat-like states.

We present an exact solution for the output state of the logical element, taking into account the finite squeezing of the resource state, and show how the squeezing parameter affects the probability of obtaining states similar to Schrödinger cat states and their fidelity (Fig. 1). It is easy to see that an increase in squeezing will not lead to an increase in fidelity, starting from a certain threshold. At the same time, as can be seen in Fig. 1b, squeezing significantly increases the probability of the expected measurement result. This is due to the fact that the probability density per unit momentum interval of the ancillary oscillator, initially prepared in a cubic state, significantly depends on squeezing.

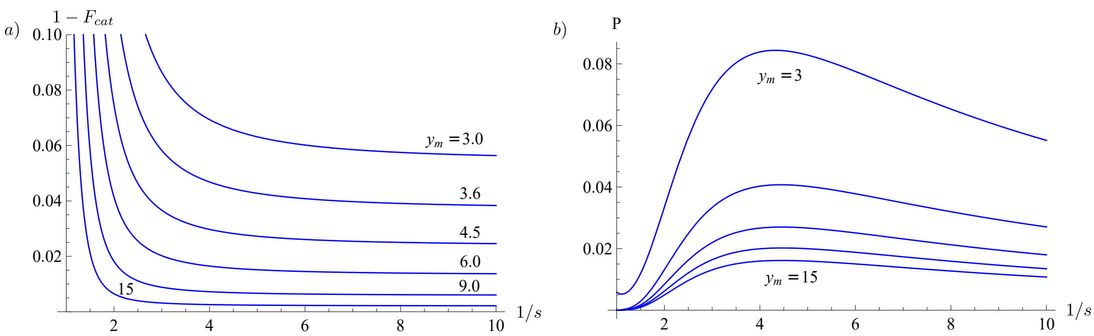

Figure 1: a) The infidelity $1 - F_{cat}$ between the actual output state and the state of an ideal Schrödinger cat. b) Probability density $P(y_m)$ of the measurement outcome depending on the initial squeeze of the ancillary state. Here $1/s \geq 1$ is the stretching factor of the ancilla coordinate quadrature.

Since in a possible experiment the measurement result is determined with a certain precision we consider a mixed output state. This state occurs when the observed ancilla momentum falls within an acceptance interval with the width d centered at y_m. The target cat state $\psi^{(t)}_{cat}(x)$ is in the center of the acceptance interval (i.e., when $y_m = \overline{y}_m$) and has a certain amplitude α and phase θ. Numerical calculation of the fidelity $F^{(t)}(y_m)$ between the target state and the pure output state obtained by a projective measurement with a certain result y_m (Fig. 2a), shows that due to the oscillatory behavior of the phase within a large acceptance interval, both "even" and "odd" cat states are possible. Thus, if one has a target "even" cat state, then at certain values of the measured momentum y_m, the fidelity $F^{(t)}(y_m)$ almost vanishes. It is a purely phase effect. As follows from Fig. 2b, in order to preserve high fidelity $F^{(mix)}(y_m; d)$ in the case of a mixed state, it is necessary to use a narrower acceptance interval.

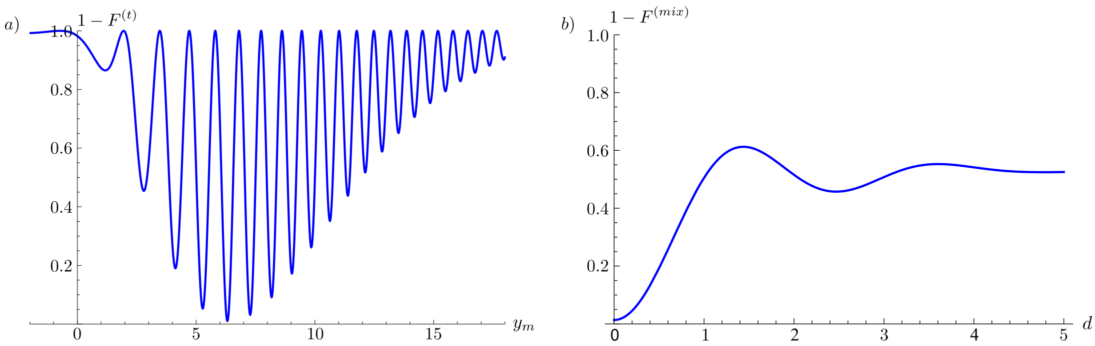

Figure 2: a) Infidelity $1 - F^{(t)}(y_m)$ between the target even cat state at $\overline{y}_m = 6.33$ and pure state that correponds to current measurement outcome y_m. b) Infidelity $1 - F^{(mix)}(y_m; d)$ between the target even cat state at $\overline{y}_m = 6.33$ and the corresponding mixed state in dependence on the acceptance interval width d.

With the use of non-Gaussian states as a resource, there is a problem of quantifying the deviation of probability distribution shape from the Gaussian, the so-called non-Gaussian measures of quantum states [8, 9], and their applicability to assess the efficiency of quantum gates. One would expect that a non-Gaussian resource state, for which a correctly chosen measure is larger, would be able to take more efficiently the result of quantum evolution out of the class of Gaussian schemes with optimal use. In our case, for the non-Gaussian measures considered, the "amount of non-Gaussianity" in the output cat state becomes almost independent of the squeezing parameter with a sufficiently large squeezing degree if the measured ancillary momentum y_m falls within the range specified before the measurement. However, to assess the output state, it is necessary to take into account not only the fidelity the prepared states, but also the probability of obtaining the necessary measurement result. This means that the use of a cubic phase state with a large non-Gaussianity and Wigner negativity can make the gate less efficient.

References

[1] *S. Lloyd, S.L. Braunstein*, Quantum computation with continuous variables. Phys. Rev. Lett. **82**, 1784 (1999).

[2] *S.L. Braunstein, P. van Loock*, Quantum information with continuous variables. Rev. Mod. Phys. **77**, 513 (2005).

[3] *A. Furusawa, J.L. Sørensen, S.L. Braunstein, C. A. Fuchs, H. J. Kimble, E. S. Polzik*, Unconditional quantum teleportation. Science **282**, 706 (1998).

[4] *X. Li, Q. Pan, J. Jing, J. Zhang, C. Xie, K. Peng*, Quantum dense coding exploiting a bright Einstein-Podolsky-Rosen beam. Phys. Rev. Lett. **88**, 047904 (2002).

[5] *I. V. Sokolov*, Schrödinger cat states in continuous variable non-Gaussian networks. Phys. Lett. A **384**, 126762 (2020).

[6] *N. I. Masalaeva and I. V. Sokolov*, Quantum statistics of Schrödinger cat states prepared by logical gate with non-Gaussian resource state. Phys. Lett. A **424**, 127846 (2022).

[7] *D. Gottesman, A. Kitaev, and J. Preskill*, Encoding a qubit in an oscillator. Phys. Rev. A **64**, 012310 (2001).

[8] *R. Takagi and Q. Zhuang*, Convex resource theory of non-Gaussianity. Phys. Rev. A **97**, 062337 (2018).

[9] *F. Albarelli, M.G.Genoni, M.G.A.Paris, and A.Ferraro*, Resource theory of quantum non-Gaussianity and Wigner negativity. Phys. Rev. A **98**, 052350 (2018).

The effect of dissipation on the entangled quantum states of two coupled superconducting qubits in strong driving fields

Marina Bastrakova[1,2*], **Vyacheslav Munyaev**[1]

[1] *Lobachevsky State University of Nizhny Novgorod, Nizhny Novgorod, Russia*
[2] *Russian Quantum Center, Moscow, Russia*
*E-mail: bastrakova@phys.unn.ru

Abstract

The conditions for the generate and destruction of the entanglement state in two coupled flux superconducting qubits during the formation of regions of the multiphoton transitions due to the interference of Landau-Zener-Stuckelberg-Majorana are found. Based on the solution of the Floquet–Markov equation, a technique is proposed to adjust the amplitudes of driving fields for effective control of the entanglement between qubit states while taking into account the effects of decoherence.

Dynamic entanglement control is one of the main tasks in quantum information applications. In recent years, strategies based on the creation of stationary entanglement have been actively discussed theoretically and experimentally. Initially, the mechanisms of controlled generation of dissipative nonequilibrium dynamics were based on weak resonant excitations to adapt relaxation processes [1, 2, 3]. However, recently, in the framework of amplitude spectroscopy, the processes of stabilization and entanglement control have been actively studied in the case of strong external periodic influences [4], when interesting non-perturbative processes arise.

In this paper, a new technique is proposed for the flexible control of entangled states in a system of coupled flux superconducting qubits, taking into account the connection with the environment. This control is based on the Landau-Zener-Stuckelberg-Majorana interference (LZSM) [4], where by adjusting the amplitudes of *dc* and *ac* fields, we can both create and control the entanglement in the qubit system. To explain these effects, we have developed an analytical approach to the Floquet-Markov solution in the framework of perturbation theory based on tunnel constants of flux qubits for calculating concurrence in fields of arbitrary amplitude.

We get the Floquet–Markov master equation for two coupled flux qubits:

$$\frac{\partial \hat{\rho}}{\partial t} = -i\left[\hat{H}\left(t\right), \hat{\rho}\right] + \hat{\Gamma}\hat{\rho}, \tag{1}$$

with the global Hamiltonian:

$$\hat{H}\left(t\right) = -\frac{1}{2}\sum_{q=1}^{2}\left(\epsilon_q(t)\sigma_z^{(q)} + \Delta_q\sigma_x^{(q)}\right) - \frac{g}{2}\sigma_z^{(1)}\sigma_z^{(2)}, \tag{2}$$

where $\sigma_z^{(q)}$, $\sigma_x^{(q)}$ are the Pauli matrices, with $q = 1, 2$ the index of each qubit. We take $\hbar = 1$ in this work. The parameter Δ_q is the tunnel splitting of the qubit levels: $\left|\downarrow^{(q)}\right\rangle$ (ground state) and $\left|\uparrow^{(q)}\right\rangle$ (excited state), which defines the computational basis. The strength of the interaction between qubits is defined as g. The qubit is driven by a time dependent bias $\epsilon_q(t) = \epsilon_q + v_q\left(t\right)$, where ϵ_q is the static bias component of external field, and $v_q\left(t\right) = A_q\cos\left(\omega t - \varphi_0\right)$ is the harmonic variable part of the magnetic flux of the microwave amplitude field, A_q, and frequency, ω, applied to each qubit.

The dissipative operator in Eq. (1) is defined by:

$$\hat{\Gamma} = \sum_{q=1}^{2}\left(\Gamma_{\varphi_q}\hat{D}\left[\hat{\sigma}_z^{(q)}\right] + \Gamma_q\hat{D}\left[\hat{\sigma}_-^{(q)}\right] + \Gamma'_q\hat{D}\left[\hat{\sigma}_+^{(q)}\right]\right), \tag{3}$$

where Γ_{φ_q}, Γ_q and Γ'_q are dephasing, relaxation and excitation incoherent rates, respectively; $\hat{D}[\hat{a}]\,\hat{\rho} \equiv \hat{a}\hat{\rho}\hat{a}^\dagger - \frac{1}{2}\left\{\hat{a}^\dagger\hat{a}, \hat{\rho}\right\}$ and the Lindblad operators $\hat{\sigma}_z^{(q)}$, $\hat{\sigma}_+^{(q)}$, $\hat{\sigma}_-^{(q)}$ are expressed via computational basis (as if there were no coupling, $g = 0$, and field, $v_q\left(t\right) = 0$. Note that the Eq. (1) is valid in the case

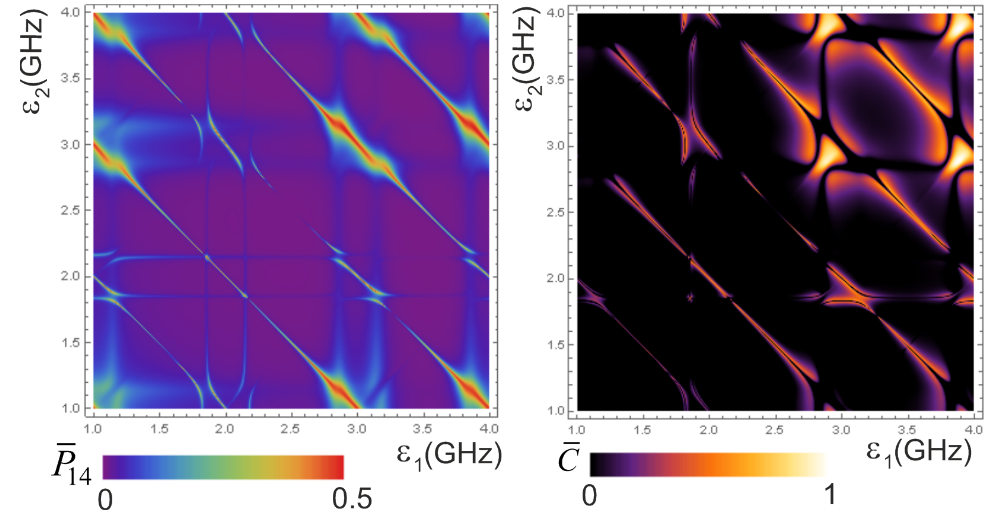

Figure 1: Dependence of the probability of a multiphoton transition $\bar{P}_{14}$ and concurrence $\bar{C}$ as a function of the *dc* fields ϵ_1 and ϵ_2. Here are the parameters: $g = 0.15$ GHz, $\Delta_2 = 1.5\Delta_1 = 0.2$ GHz, $A_1 = A_2 = 5$ GHz, $\omega = 1$ GHz, $\Gamma_{\varphi_1} = \Gamma_{\varphi_2} = 0.0001$ GHz, $\Gamma_1 = \Gamma_1 = 0.005$ GHz, and $\tau_\beta = 30$ mK.

the incoherent rates are much smaller than all coherent energy scales (approximation of independent rates). At the reservoirs fundamental temperature τ_B, the relaxation and excitation parameters are related as $\Gamma'_q = \Gamma_q \exp\left(-\Delta E^{(q)}/\tau_B\right)$, where $\Delta E^{(q)}$ is the energy gap of the q-th qubit. We calculate the average entanglement measure as a concurrence: $\bar{C}\left(\rho\right) = \max\left\{0, \lambda_4 - \lambda_3 - \lambda_2 - \lambda_1\right\}$, where λ_i's are real numbers in decreasing order and correspond to the eigenvalues of the matrix $R = \sqrt{\sqrt{\rho}\tilde{\rho}\sqrt{\rho}}$, with $\tilde{\rho} = \sigma_y^{(1)} \otimes \sigma_y^{(2)} \rho^* \sigma_y^{(1)} \otimes \sigma_y^{(2)}$.

Our study shows that the creation of dynamic entanglement is carried out due to the coherent superposition of states induced by external fields at multiphoton resonances [4, 5]. As can be seen on Fig. 1, the maximum value of concurrence, $\bar{C}$, occurs when the control bias parameters, ϵ_1 and ϵ_2, approaches the regions of multiphoton resonances of the transition $\left|\downarrow^{(1)}\downarrow^{(2)}\right\rangle \to \left|\uparrow^{(1)}\uparrow^{(2)}\right\rangle$: $\epsilon_{1,2} + g + k\omega \approx 0$, $\epsilon_1 + \epsilon_2 + k\omega \approx 0$, which were obtained by us in the work [5]. To explain the discovered effects, we have developed an analytical theory for calculating concurrence based on the resonant perturbation theory for the smallness of the tunnel energies of qubits in Eq. (1) with Hamiltonian (2). A good coincidence of numerical and analytical results is demonstrated, taking into account decoherence processes.

The work was supported by UNN within the framework of the strategic academic leadership program “Priority 2030” of the Ministry of Science and Higher Education of the Russian Federation.

References

[1] *F. Reiter, L. Tornberg, G. Johansson, and A.S. Sørensen*, Steady-state entanglement of two superconducting qubits engineered by dissipation. Phys. Rev. A **88**, 032317 (2013).

[2] *M.E. Kimchi-Schwartz, L. Martin, E. Flurin, C. Aron, M. Kulkarni, H.E. Tureci, and I. Siddiqi*, Stabilizing Entanglement via Symmetry-Selective Bath Engineering in Superconducting Qubits. Phys. Rev. Lett. **116**, 240503 (2016).

[3] *A.L. Gramajo, D. Domínguez, and M.J. Sánchez*, Amplitude tuning of steady-state entanglement in strongly driven coupled qubits. Phys. Rev. A **98**, 042337 (2018).

[4] *O.V. Ivakhnenko, S.N. Shevchenko, F. Nori*, Nonadiabatic Landau–Zener–Stückelberg–Majorana transitions, dynamics, and interference. Phys. Rep. **995**, 1-89 (2023).

[5] *V.O. Munyaev and M.V. Bastrakova*, Control of spectroscopic features of multiphoton transitions in two coupled qubits by driving fields. Phys. Rev. A **104**, 012613 (2021).

Two-qudit logical transformations on atomic-field modes with orbital angular momentum

Elizaveta Bashmakova*, Evgenii Vashukevich, Tatiana Golubeva, Yuri Golubev

St. Petersburg State University, St. Petersburg, Russia
*E-mail: bashmakova.elizaveta@mail.ru

Abstract

In this work, we propose a method for implementing multipartite interaction based on a quantum nondemolition interaction protocol between multimode light with orbital angular momentum and an ensemble of cold atoms. We have demonstrated an original method of logical encoding atomic-field subsystems by the parity of the orbital angular momentum, which makes it possible to introduce a logical basis that belongs to the space of two-qubit states. We have shown that, the resulting two-qubit transformation is equivalent to the SWAP transformation operation under the certain physical conditions.

Today there has been significant interest to high-dimensional ($d-$dimensional) quantum systems (qudits) due to the possibility of increasing the information capacity of the channel – the amount of information that can be encoded in one physical carrier. That turns out to be very useful in the problems of quantum communication and quantum information processing [1]. Nevertheless, there are still blind spots in the problem of efficient manipulation of multidimensional quantum states.

The orbital angular momentum (OAM) is one of the exciting resource for constructing a qudit since the OAM can take any integer values, which allows us to work in the Hilbert space of high dimension [2]. A significant factor is also that Laguerre–Gaussian modes with OAM show high stability and a relatively high decoherence time when propagating in a turbulent atmosphere [3].

To achieve the universality of quantum computation, it is necessary to be able to implement a universal set of quantum logical operations. Moreover, in order to create quantum gates, we need to find the appropriate physical system for the gates' realization, and the ability to organize efficient interaction between quantum objects. In this work, the multimode light with orbital angular momentum (OAM) and atomic ensemble are considered as a physical systems, and quantum nondemolition (QND) interaction [4] is applied.

In this work, we have studied in detail the mechanism of interaction between multimode light with orbital angular momentum and an atomic ensemble in the dipole approximation. First, we described a model for the interaction of an ensemble of cold atoms with a non-resonant field, which is a superposition of modes with certain angular momentum in the presence of a control field (see Fig. 1). And then we analyzed the interaction Hamiltonian in this model, which contains all the information about the evolution of the field and atomic variables. Moreover, one of our aims was to search for the certain physical conditions under which the interaction is reduced to the mechanism of quantum nondemolition interaction.

We have shown that phase-sensitive excitation transfer from the even field modes to odd medium modes and vice versa can be achieved selecting a control field whose OAM is equal to ± 1. In other words, in our system we classify all quantum states into states with either even or odd OAM values. This structure of the atomic-field subsystems allowed us to use the parity modes for the original encoding of logical states. Therefore, we have deeply studied states with OAM in the framework of quantum nondemolition interaction in terms of discrete variables. We analyzed the quantum nondemolition interaction of multidimensional atomic-field systems. In this work, we present the results of the simplest example, the qubit consideration.

In our analysis, the logical states "0" and "1" encode as a superposition of atomic-field states when excitations are distributed among the subsystems of different parity. Generally, the nondemolition interaction of atomic-field systems does not belong to the computational basis of qubits, since the excitation bunching effect can take place. However, we managed to find a logical basis that belongs to the two-qubit space.

We have demonstrated that the implemented type of logical operation on atomic-field qubits depends on the effective interaction constant, therefore, determined by the interaction geometry. We obtained that when the value of the interaction constant is equal to 2, the considered logical operation is equivalent to the SWAP transformation operation. Then, it can be provide an entangling two-qubit gate $\sqrt{SWAP}$ by manipulating the interaction time. Then we want to apply the developed apparatus of multimode QND interaction to $d-$dimensional systems.

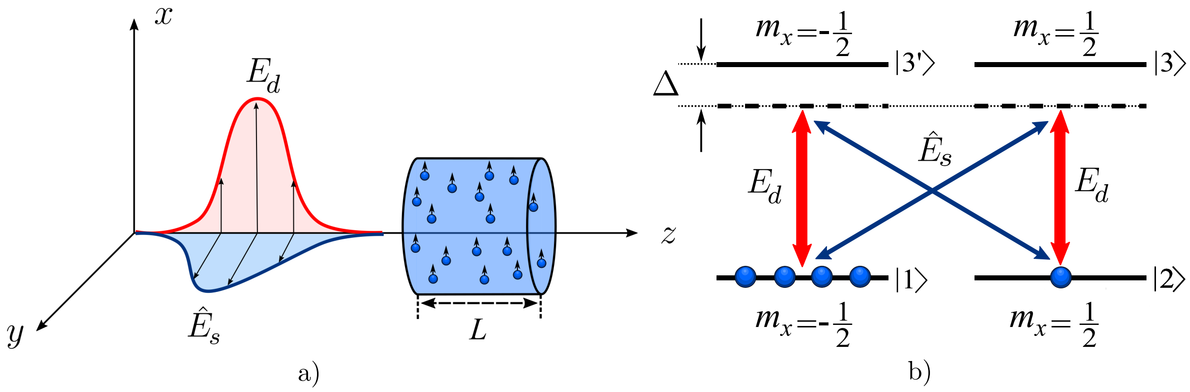

Figure 1: The schematic draw of the system under consideration: a) a cell with a cloud of four-level atoms represented as a cylinder with a length of L along the z axis interacts with a strong driving field $\vec{E}_d$ and a weak signal field $\hat{E}_s$; b) the energy levels diagram of an ensemble of atoms interacting with quantum signal field $\hat{E}_s$ and driving $\vec{E}_d$ fields in a quantum nondemolition interaction. The frequencies of the fields are detuned from the frequencies of the atomic transitions, respectively, by Δ. For the quantization axis along x the value m_x is total angular momentum quantum number.

This research was supported by Russian Science Foundation (project No. 22-22-00022).

References

[1] *M. Erhard, R. Fickler, M. Krenn and A. Zeilinger*, Twisted photons: new quantum perspectives in high dimensions. Light Sci. Appl. **7**, 17111 (2018).

[2] *L. Allen, M. W. Beijersbergen, R. J. C. Spreeuw and J. P. Woerdman*, Orbital angular momentum of light and the transformation of Laguerre-Gaussian laser modes. Phys. Rev. A. **45**, 8185 (1992).

[3] *S. Li, S. Chen, C. Gao, A.E. Willner and J. Wang*, Atmospheric turbulence compensation in orbital angular momentum communications: Advances and perspectives Opt. Commun. **408**, 68 (2018).

[4] *K. Hammerer, A. S. Sørensen and E. S. Polzik*, Quantum interface between light and atomic ensembles. Rev. Mod. Phys. **82**, 1041 (2010).

Cost-efficient low-loss four-channel active demultiplexer for single photons

M. Dryazgov[1], Yu. Biriukov[2], I. Dyakonov[2], A. Korneev[1,2], S. Straupe[2], S. Kulik[3,4]

[1] *National Research University Higher School of Economics, Moscow, Russia*
[2] *Quantum technology centre, Lomonosov Moscow State University, Moscow, Russia*
[3] *Lomonosov Moscow State University, Moscow, Russia*
[4] *Laboratory of quantum engineering of light, South Ural State University (SUSU), Russia, Chelyabinsk, 454080, Prospekt Lenina 76*

Abstract

We report a design and implementation of a cost-effective spatial demultiplexer which produces 4 indistinguishable photons with efficiency 39.7% per channel. Our scheme is based on a free-space storage/delay line which accumulates 4 photons and releases them by a controlled polarization rotation with a single Pockels cell.

Introduction

Linear-optical quantum computing requires an efficient method of on-demand generation of a definite number of indistinguishable photons which can be used to encode qubits, e.g. fed into a photonic chip performing a quantum algorithm. The majority of the reported experimental implementations make use of either spontaneous parametric down-conversion (SPDC) in bulk crystals or by four-wave mixing in waveguides in order generate single photons. Recent advances in semiconductor quantum dot (QD) sources [2] and emergence of commercially available QD source chips propelled the integration of this type of sources to the optical quantum computing domain. Fabrication of a set of identical QD source is the notoriously hard task and hence the experimental challenge of using a single QD as a multiphoton source has upsprung.

In this work we present a cost-efficient four-beam demultiplexer requiring only one fast optical switch (Pockels cell). Although our demultiplexer does not increase the probability to produce a photon at the output, it drastically reduces the amount of fast switches required for splitting the input photon sequence and eliminates the necessity to assemble long fiber delay lines in order to compensate for large delay times between output photon bursts in each channel.

Experimental method

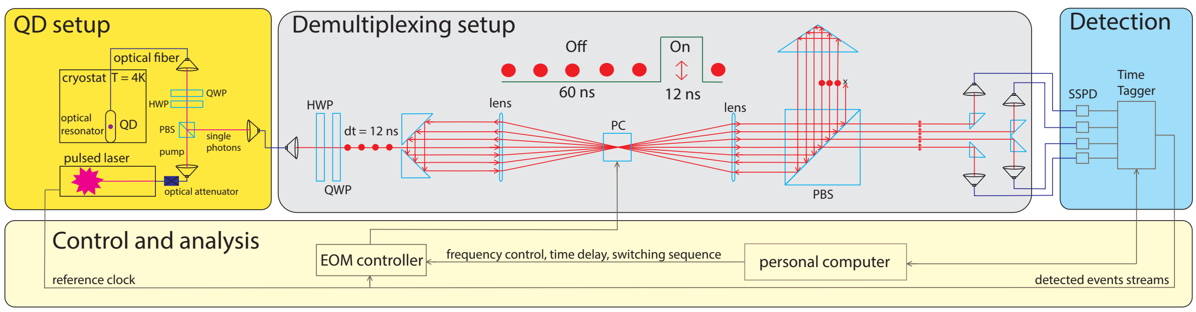

Figure 1: A schematic illustration of the experiment with the QD setup, the demultiplexing setup, the detection setup, and control and analysis setup.A detailed description of the setup is found in Sec. **??**

We exploit a simple idea of storing and releasing a bunch of photons inside an optical loop. Our setup is presented in Fig. 1. We use a semiconductor QD source in the micropillar configuration [1].

We pump the QD in cross-polarized scheme using resonant picosecond pulses emitted with 82.6 MHz repetition rate at 918.83 nm wavelength. The single photons are coupled to a single-mode optical fibre and fed into the demultiplexer through the output coupler. The demultiplexer is an optical loop with round-trip time equal to the time difference $\Delta t = 12.1$ ns between the consecutive pump pulses. Each round-trip shifts the beam transversely in a horizontal direction by 3 mm on average. A 1:1 telescope inside the loop serves two purposes: it minimizes the diffraction effect on the beam passing multiple times through a loop and focuses all the beams through the 3 mm aperture of the PC. The currently used geometry of the optical components allows to store only 4 photons inside the loop. The half-wave and quarter-wave plates at the input adjust the polarization of the input photons to a horizontal state. After passing through the PC each photon reflects of the polarization beam splitter (PBS) and the right-angle prism and completes the round trip by passing the PC again. Each sixth clock cycle the PC rotates the polarization of the photons in the loop and hence releases a just arrived (the fourth) photon and three previously stored ones. Ideally switching has to be done each fourth cycle however hardware restrictions imposed by the high-voltage driver allow a minimal interval between consecutive switching events of 70 ns. The high-voltage driver (BME Bergmann) switches the cell using a 12 ns long voltage pulse. The driver is controlled by a homebuilt FPGA-based circuit which uses the pump laser as a source of the reference clock signal. The voltage pulse peak is synchronized to the moment when all four photons pass through the Pockels cell and the rise and fall fronts do not affect the neighbouring photons. The photons with rotated polarization pass through the PBS and enter the circuit where each beam is separated from the other using knife-edge reflective prisms. After that photons are coupled to the single mode fibres. Each fiber coupler is mounted onto a translation stage in order to compensate for slight differences of the output channel lengths including the lengths of optical fibers. The output of each fiber coupler is sent either to superconducting single-photon detectors (SSPD) or to a balanced fiber beamsplitter which enables Hong-Ou-Mandel type quantum interference.

Results

Firstly, we characterized the QD itself. Figure 2(a) presents the auto-correlation function $g^{(2)}(\tau)$ for our QD pumped in resonant regime in cross-polarized configuration. The observed single-photon purity is $g^{(2)}(0) = 0.024 \pm 0.001$. The indistinguishability of the photons was asserted using a Hong-Ou-Mandel interferometer with $\Delta t = 12.1$ ns delay introduced into one of the arms. The average photon count rate detected using the SSPD was about 5 MHz.

Then, we measured auto-correlation functions for each output channel, the result is presented in Fig. 2(b–f). Small parasitic peaks can be witnessed between the demultiplexed photons. They originate from the imperfect polarization switching and PBS extinction ratio. Our configuration implies passing four beams through a single PC and each beam travels in a slightly different direction due to focusing. For this reason it is impossible to reach optimal performance of the PC for each of the beams. We decided to use the second output channel as a reference one because it was easier to find the best orientation of the PC. Thus the second channel auto-correlation function exhibits minimal effect from the parasitic peaks.

Next we tested the indistinguishability of the photons after they have been split into different channels. We connected a balanced fiber beamsplitter to the outputs of a selected pair of channels and measured the second-order cross-correlation function $g^{(2)}(\tau)$. Since we used single-mode fiber, which doesn't preserve the polarization state, we had to place an additional pair of half- and quarter-waveplates to each channel and vary their orientation to compensate the unknown polarization rotation inside the fibers. The measurement results indicate that the indistinguishability of the photons remains on the same level as for the photons tested directly from the QD source. We used a correction formula from [2] to infer the estimated value of the Hong-Ou-Mandel interference visibility.

Finally, Fig. 4(a) illustrates the detection rates of multiphoton events at the output of the demultiplexer. We used the data to get the estimate of the efficiency across all output channels. The probabilities to detect n-photon events were fitted with an exponential function p^n, where p is the probability to detect a photon at the output of the demultiplexer. The value p is related to the source brightness $B = \nu/r$, where ν is the detected single-photon count rate at the output of the source and r is the repetition rate of the pump laser. The ratio $e = p/B$ expresses the efficiency of each demultiplexer channel. Then, for the described scheme, $e = 0.225$, which does not include the efficiency of the detectors (0.85 on average), and photon losses due to the maximum possible frequency of the Pockels cell (4/6). With this in mind,

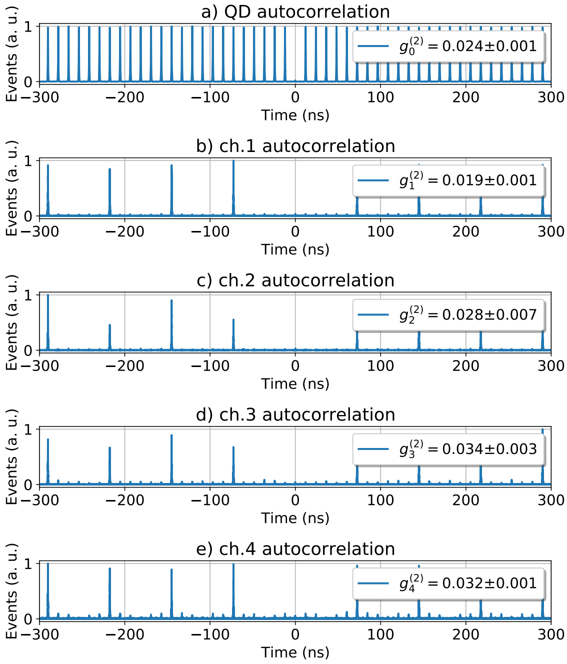

Figure 2: (a) Auto-correlation function for the QD. (b-e) Auto-correlation functions for each of 4 channels of the demultiplexer.

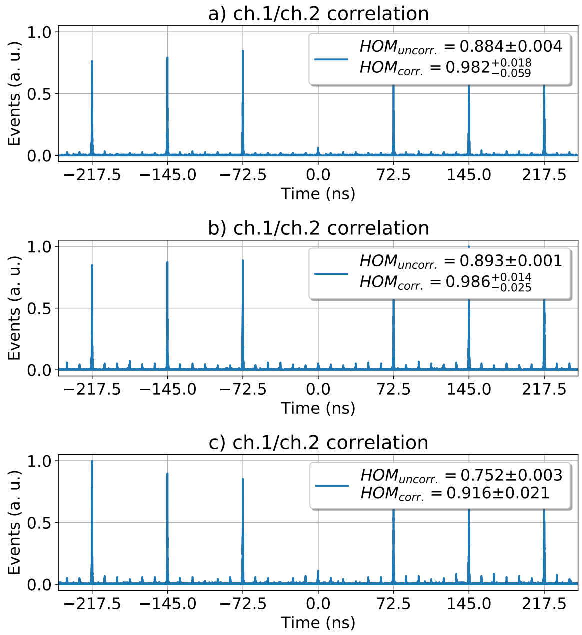

Figure 3: Uncorrected and corrected indistinguishability of the photons for (a) channels 1-2, (b) channels 1-3 and (c) channels 1-4 of the demultiplexer.

the efficiency increases to $e = 0.397$. This value is due to losses in polarizing beam splitters, other optical elements of the circuit, the efficiency of optical couplers and multiple passages through the Pockels cell.

Acknowledgements

The work was supported by Russian Science Foundation grant 22-12-00353 (https://rscf.ru/en/project/22-12-00353/) in part of demultiplexer design and characterization, and by Rosatom in the framework of the Roadmap for Quantum computing (Contract No. 868-1.3-15/15-2021 dated October 5, 2021 and Contract No.P2154 dated November 24, 2021).

References

[1] M.V. Rakhlin, A.I. Galimov, I.V. Dyakonov, N.N. Skryabin, G.V. Klimko, M.M. Kulagina, Yu.M. Zadiranov, S.V. Sorokin, I.V. Sedova, Yu.A. Guseva, D.S. Berezina, Yu.M. Serov, N.A. Maleev, A.G. Kuzmenkov, S.I. Troshkov, K.V. Taratorin, A.K. Skalkin, S.S. Straupe, S.P. Kulik, T.V. Shubina, and A.A. Toropov. Demultiplexed single-photon source with a quantum dot coupled to microresonator. *Journal of Luminescence*, 253:119496, 2023.

[2] N. Somaschi, V. Giesz, L. de Santis, J. C. Loredo, M. P. Almeida, G. Hornecker, S. L. Portalupi, T. Grange, C. Antón, J. Demory, C. Gómez, I. Sagnes, N. D. Lanzillotti-Kimura, A. Lemaítre, A. Auffeves, A. G. White, L. Lanco, and P. Senellart. Near-optimal single-photon sources in the solid state. *Nature Photonics*, 10(5):340–345, May 2016.

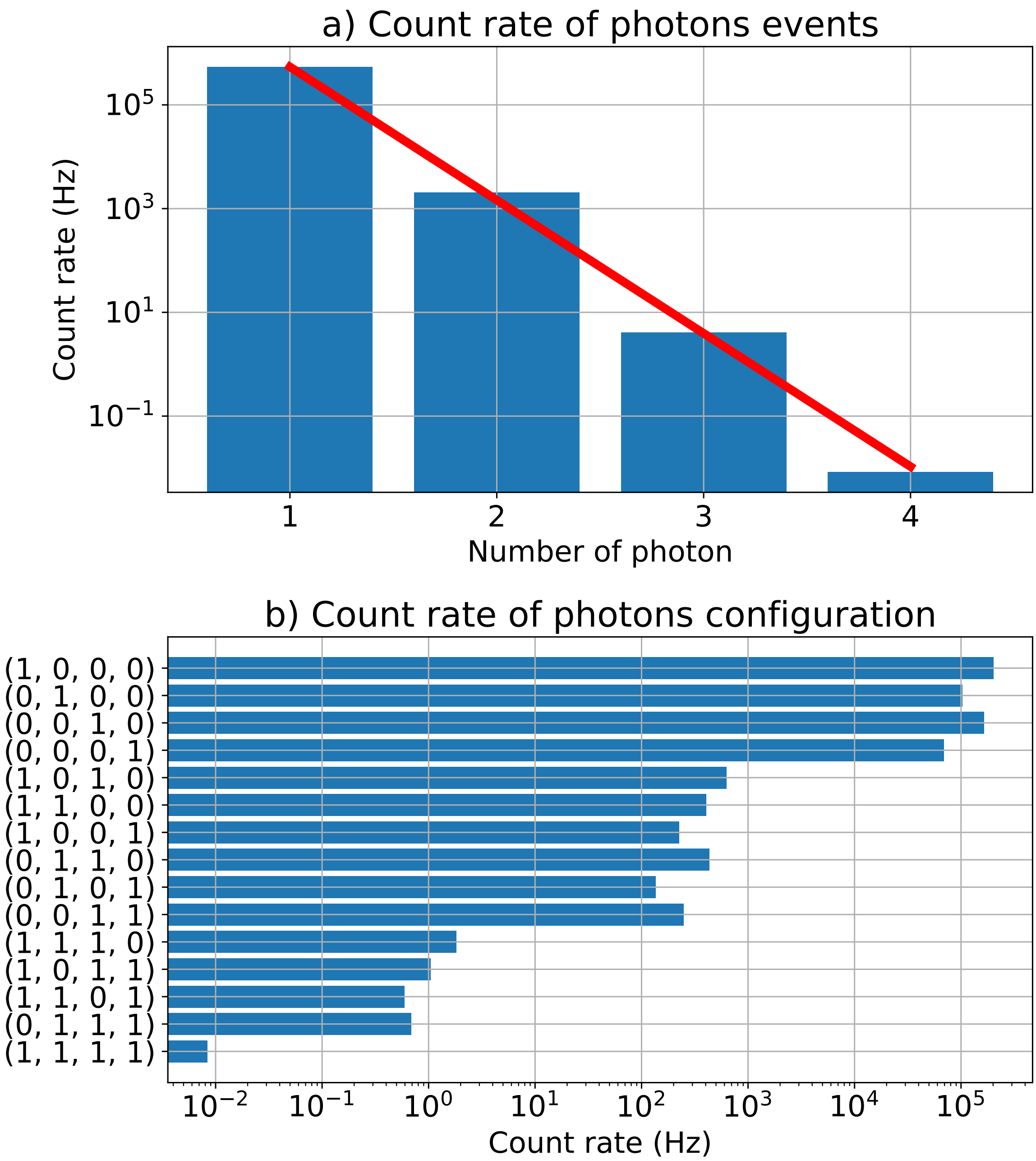

Figure 4: Count rates of (a) photons events and (b) different configurations of photon distributions among channels. Red line – approximation by an exponential function p^n

Emulation of Quantum Measurements using Mixtures of Coherent States

Svetlana Vlasenko[1*], **Alexander Mikhalychev**[1], **Dmitri Mogilevtsev**[1]

[1] *B. I. Stepanov Institute of Physics, NAS of Belarus, Nezavisimosti ave. 68, 220072 Minsk, Belarus*
*E-mail: svetlana.vlasenko@yahoo.com

Abstract

The approach to emulate quantum experiments using a mixture of coherent states is proposed. This allows one to reproduce fundamental quantum effects using resources which can be much more feasible in the laboratory. The method is applied to emulation of Hong-Ou-Mandel effect, as well as for the emulation of experiments with bright non-classical states.

It is known that density operators can be decomposed over coherent states. At the same time, if such a representation comprises even a small number of states, it still may have a high accuracy. Such a decomposition has already demonstrated its usefulness in quantum tomography and allowed one to avoid calibrating detectors [1]. The tomography deals with an unknown state which needs to be reconstructed using the results of its measurements. Here, we solve an opposite problem: using a known but unavailable state, one needs to reproduce (emulate) measurement results with it. Since the state is known, the representation can be efficiently optimized and enables using just a small set of states.

The essence of emulation

The essence of the proposed emulation method [2] is representation of a quantum state ρ_{true} to be emulated as a mixture of probe states ρ_j (usually, coherent state projectors $\rho_j = |\alpha_j\rangle\langle\alpha_j|$):

$$\rho_{true} \approx \rho = \sum_j c_j \rho_j, \quad \sum_j c_j = 1. \tag{1}$$

Here, it is essential that, if the state ρ is nonclassical, at least one of the coefficients c_j should be negative. The probe (coherent) states are randomly sampled from the constructed set. Besides, they are marked by an additional degree of freedom (an ancillary quantum object in two mutually orthogonal states $|+\rangle$ and $|-\rangle$) according to the sign of their weight $\operatorname{sgn} c_j$ (classical bit of information) and subjected to the measurements. The sign is decoded by introducing an observable $A \propto (|+\rangle\langle+| - |-\rangle\langle-|)$ over the ancillary particle and performing the joint measurement of the observable $O \otimes A$, where O is the observable, measurement of which is to be emulated. Such a procedure provides the same expectation values for an emulated experiment compared to the experiment with the original initial state. Thus, even without having the quantum state itself, we can reproduce (emulate) the measurement results with it.

Emulation of Hong-Ou-Mandel effect

Using the proposed approach, one can emulate experiments with single-photon, two-photon and even entangled (NOON) quantum states using a finite set of phase-averaged coherent states.

In order to obtain the coefficients c_j in the representation (1), one must solve the problem of fidelity maximization. If $\rho_{true} = |1\rangle\langle 1|$ is a sigle-photon state, the set of probes can be chosen in the form of five phase-averaged coherent states with the amplitudes $\alpha_j = \{0,\, 0.25,\, 0.5,\, 0.75,\, 1.0\}$. Then, the coefficients are $c_j = \{-21.8,\, 25.6,\, -3.1,\, 0.33,\, -0.0028\}$. The fidelity of the constructed representation for the single-photon state exceeds 0.9996. Similarly, using seven phase-averaged coherent states enables representation of two-photon Fock states with the representation fidelity exceeding 0.998.

The emulated states can be used to demonstrate important quantum effects. In this contribution, we apply them to reproduce (emulate) Hong-Ou-Mandel effect and interferometric phase measurement for NOON-states. In Fig. 1a, the scheme of Hong-Ou-Mandel effect with real single-photon state is presented, while in Fig. 1b the corresponding emulation scheme is shown. As one can see, the emulation schemes can be quite easily realized experimentally using a set of simple optical devices such as beam splitters

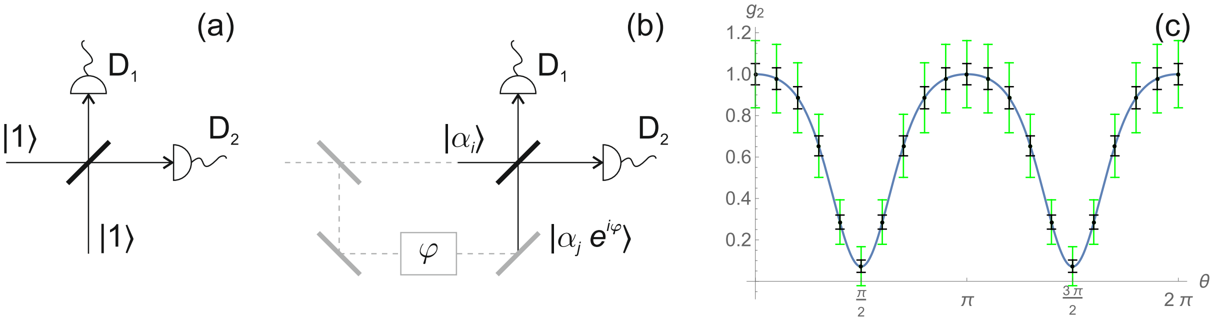

Figure 1: (a) Scheme of observing Hong-Ou-Mandel effect with the single photon and (b) the setup for its classical emulation. (c) Dependence of normalized coincidence rates $g_2(\theta)$ on the measured phase shift θ. Solid lines indicate the dependence for interference of two single-photon states. Points and error bars show the values and the standard deviations for classically emulated single-photon states for $N = 3 \times 10^7$ (green bars) and $N = 3 \times 10^8$ (black bars) repetitions.

and phase shifters. Here, we estimated to which extent the representation is more expensive in terms of the necessary number of state copies, since it is quite important for an experimental realization. In Fig. 1c, the errors for 3×10^7 and 3×10^8 copies are given.

Emulation of "collapses" and "revivals" with bright sub-Poissonian states

The emulation procedure can be quite useful for the emulation of the effects with bright non-classical state. We do not encounter serious problems when we deal with few-photon states: there are a lot of methods of generating them. However, the situation is different when we need to make experiments using states with larger number of photons – only special classes of such states can be generated. Here, the possibility to emulate such experiments may help to overcome these difficulties. We demonstrated the emulation of effects characteristic for bright sub-Poissonian states, in particular "collapses" and "revivals" for two-level system in the Jaynes-Cummings model.

Sub-Poissonian states with the following photon number distribution

$$\rho_{nn} = \frac{1}{2\pi(Q+1)\langle n\rangle} \exp\left[-\frac{(n-\langle n\rangle)^2}{2(Q+1)\langle n\rangle}\right] \tag{2}$$

where $\langle n\rangle$ is the average photon number and $Q = \Delta n/\langle n\rangle - 1$ is the Mandel parameter, can be in a robust and scalable way decomposed in terms of phase-averaged coherent states and, thus, emulated. The emulation provides good coincidence with the behavior of real sub-Poissonian states. However, if one limits himself by a reasonable number of the probe states and of the measurement repetitions, the achievable values of Q are limited from below by $Q \gtrsim -0.5$.

Conclusions

We proposed the approach to emulate (reproduce) quantum experiments using classical states. The described approach is an efficient tool in a number of applications. It is useful for demonstrating fundamental quantum experiments, which, among other applications, can be used for preparation of laboratory works for students — real quantum sources can be quite expensive or unavailable at all. Also, the method can provide the possibility to test detecting equipment for fundamental quantum experiments even before the required nonclassical states become available.

References

[1] *J. Rehacek,D. Mogilevtsev, and Z. Hradil*, Operational tomography: fitting of data patterns. Phys. Rev. Lett., 105(1), 010402(2010).

[2] *A. Mikhalychev, Y.S. Teo, H. Jeong, A. Stefanov, and D. Mogilevtsev*, Emulation of quantum measurements with mixtures of coherent states. Phys. Rev. A, 105(5), 052206 (2022).

Resonant Dynamical Casimir Effect in Waveguide-coupled Qubit Arrays

Egor S. Vyatkin[1*], **Alexander V. Poshakinskiy**[1], **Alexander N. Poddubny**[1]

[1] *Ioffe Institute, St. Petersburg 194021, Russia*
*E-mail: `egor.vyatkin@bk.ru`

Abstract

We have developed a theory of parametric photon generation from arrays of modulated qubits. Such generation can be interpreted as a dynamical Casimir effect. We demonstrate numerically and analytically how the emission directionality and photon-photon correlations can be controlled by the phases of qubits frequency modulation. The emission spectrum is shown to be strongly dependent on the anharmonicity parameter. Single- and double-excited state resonances have been identified in the emission spectrum.

Waveguide quantum electrodynamics, describing photon interaction with natural or artificial atoms coupled to the waveguide, is now rapidly developing. This platform allows controllable generation of quantum light [1], and control over lifetimes [2] and entanglement [3] of coupled atom-photon excitations. Even more possibilities are opened in the structures with the parameters dynamically modulated in time. Such temporal modulation has been recently realized, for example, for the superconducting transmon qubit platform [4]. One more fundamental physical effect, that becomes possible in such structures, is the parametric generation of photon pairs, which can also be interpreted as a dynamical Casimir effect [5].

In this work, we present a general theory of parametric photon generation from arrays of qubits, coupled to the waveguide. The qubit resonance frequencies are periodically modulated in time with the

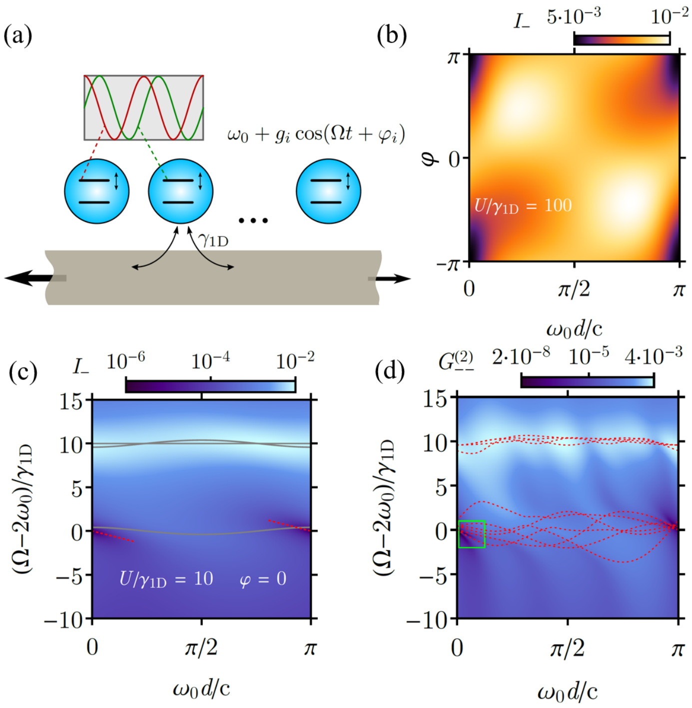

Figure 1: (a) Scheme of the structure under consideration. The array of qubits with modulated resonant frequencies coupled to a waveguide. (b) The photon emission intensity to the left I_- for a pair of qubits as a function of distance between qubits d and the modulation phase φ for the modulation frequency $\Omega = 2\omega_0 + U$. (c) The photon emission intensity to the left I_- for two qubits as a function of d and Ω. (d) The second order correlation function $G^{(2)}_{--}$ for an array of four qubits in the case of frequency modulation of the first qubit only.

frequency Ω. The setup is schematically illustrated in Fig. 1(a) Our calculation has been performed using two independent approaches, that yield equivalent results: the master equation for the density matrix and the diagrammatic Green-function technique. We have studied the dependence of the photon emission spectrum and photon-photon correlation functions depending the anharmonicity of the qubit potential U, the distance between the neighboring qubits and the relative modulation phase φ.

The interference between photons emitted from different qubits can be controlled by relative phase of their frequency modulation. Our calculation shows how this can be used to obtain directional photon pair emission [Fig. 1(b)], similarly as it happens for non-parametric quantum photon sources. We have obtained compact analytical expressions for the emission directionality.

The calculated emission spectrum is very sensitive to the anharmonicity parameter. The anharmonicity controls the relative weight of the spectral features around the single-excited state resonances at $\omega \approx \omega_0$ (ω_0 is the qubit frequency) and the double excited qubit resonances at $2\omega_0 + U$, see Fig. 1(c). The latter become more prominent with the increase of the anharmonicity. When the number of qubits is $N = 4$ or larger, additional sharp spectral features, corresponding to the double-excited subradiant states, appear in the spectrum, shown in Fig. 1(d). We hope that our results will be useful to understand the parametric quantum emission for the waveguide-coupled qubit arrays.

References

[1] *A.S. Prasad, J. Hinney, S. Mahmoodian, K. Hammerer, S. Rind, P. Schneeweiss, A.S. Sørensen, J. Volz, and A. Rauschenbeutel*, Correlating photons using the collective nonlinear response of atoms weakly coupled to an optical mode. Nature Photonics **14**, 719 (2020).

[2] *M. Zanner, T. Orell, C.M.F. Schneider, R. Albert, S. Oleschko, M.L. Juan, M. Silveri, and G. Kirchmair*, Coherent control of a multi-qubit dark state in waveguide quantum electrodynamics, Nature Physics **18**, 538 (2022).

[3] *N.V. Corzo, J. Raskop, A. Chandra, A.S. Sheremet*, B. Gouraud, and J. Laurat, Waveguide-coupled single collective excitation of atomic arrays, Nature **566**, 359 (2019).

[4] *E.S. Redchenko, A. V. Poshakinskiy, R. Sett, M. Zemlicka, A. N. Poddubny, and J. M. Fink*, Tunable directional photon scattering from a pair of superconducting qubits, arxiv:2205.03293 (2022).

[5] *C.M. Wilson, G. Johansson, A. Pourkabirian, M. Simoen, J. R. Johansson, T. Duty, F. Nori, and P. Delsing*, Observation of the dynamical casimir effect in a superconducting circuit, Nature **479**, 376 (2011).

Investigation of CPT Resonances in the Ground State of NV Centers in diamond

S.Drofa[1,2,3,*], **S. Bolshedvorskii**[1,2,3], **V. Soshenko**[1,2], **O. Rubinas**[1,2,4], **E. Primak**[1,2,3], **P. Vilyuzhanina**[1,2,5], **A. Smolyaninov**[2], **V. Sorokin**[1,4], **A. Akimov**[1,4,6]

[1] *P.N. Lebedev Physical Institute, 53 Leninskij Prospekt, Moscow, 119991 Russia*
[2] *Spin Sensor Technology, Str. Nobel b.7, The territory of Skolkovo Innovation Center, Moscow, 143026, Russia*
[3] *Moscow Institute of Physics and Technology, 9 Institutskiy per., Dolgoprudny, Moscow Region, 141700, Russia*
[4] *Russian Quantum Center, 100 Novaya St., Skolkovo, Moscow, 143025, Russia*
[6] *National Research Nuclear University MEPhI, 31 Kashirskoye sh., Moscow, 115409,*
[5] *Texas A M University, College Station, TX 77843, USA*
*E-mail: drofa.sm@phystech.edu

Abstract

Forbidden transitions in NV centers allow to perform nuclear spin polarization and coherent population trapping of nuclear spins. This becomes useful in terms of quantum memory or in a field of quantum sensors, where nuclear spins state preparation is important.

NV centers in diamond are a promising platform for quantum computing or sensorics due to them having optically detected magnetic resonance (ODMR) in the visible spectrum, and electron spin long coherence times at room temperature [1]. In terms of both quantum computing and sensorics it is important to manipulate electron and nuclear spins of the defect.

Traditionally this is solved by polarizing electron spin in external magnetic field, coaxial to the axis of defect. The polarization is done via non-resonant laser excitation and utilizes relaxation of the excited state through intermediate states. Nuclear spin polarization is performed first by exchange of the nuclear and electron spins and then by polarization of the last one.

However in arbitrary magnetic field there is a way to polarize nuclear spin through forbidden transitions, exchanging nuclear and electron spin in the ground state of NV center, so-called electron-to-nuclear spin transitions (ENST). These transitions are shown on the Fig. 1 and colored blue, while main transitions are represented by red arrows. Furthermore, possibility of coherent population trapping (CPT) of nuclear spin allows to restrict depolarization through these transitions [2].

We study CPT resonances in bulk diamond with NV centers concentration of ∼3 ppm, grown by high-pressure-high-temperature method (HPHT) and natural carbon isotopic content. Under green laser radiation (532 nm) we observe ODMR in arbitrary transverse magnetic field. In that part of spectrum, where forbidden transitions are expected to be found, we observe three main transitions of NV centers with 13C isotope in the vicinity instead, as shown on Fig. 2.

In strong transverse and weak longitudal field fine splitting of three main transitions will be small, and forbidden transitions can be observed. One of these transitions, if paired with main transition, for example, “1” and “a” (see Fig. 1) transitions, forms a lambda-type CPT, which traps polarized nuclear spin and conserves it for a long duration.

References

[1] *V. V. Soshenko, S. V. Bolshedvorskii, O. Rubinas, V. N. Sorokin, A. N. Smolyaninov, V. V. Vorobyov, and A. V. Akimov*, Nuclear Spin Gyroscope based on the Nitrogen Vacancy Center in Diamond. Phys. Rev. Lett. **126**, 197702 (2021).

[2] *P. Huillery, J. Leibold, T. Delord, L. Nicolas, J. Achard, A. Tallaire, and G. Hétet*, Coherent microwave control of a nuclear spin ensemble at room temperature. Phys. Rev. B. **103**, L140102 (2021).

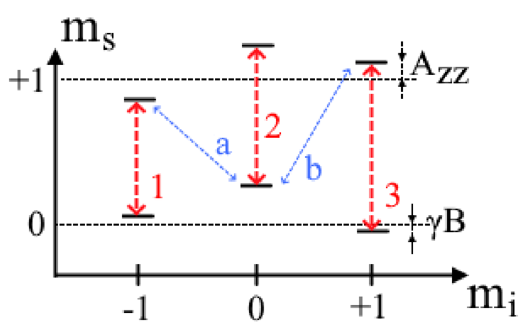

Figure 1: Energy levels for fine and hyperfine splitting of the ground state of NV center in diamond with magnetic field at angle to defect axis. Forbidden transitions are colored blue.

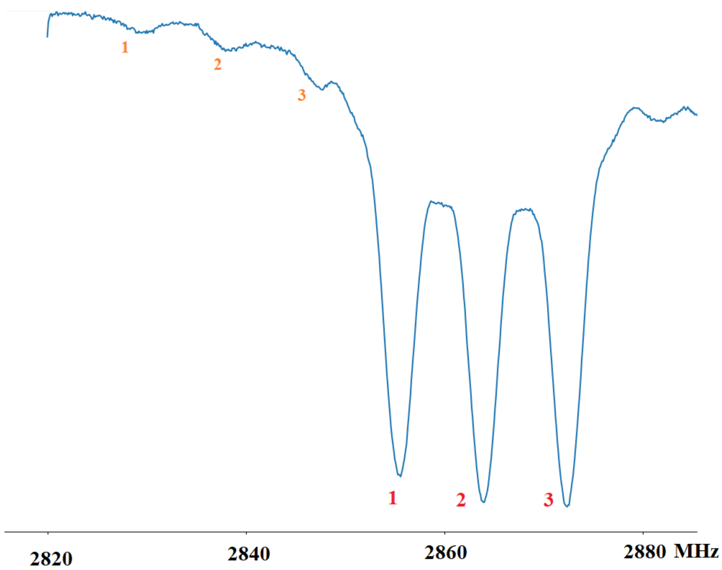

Figure 2: NV centers ensemble ODMR in longitudal magnetic field. Red numbers represent fine splitting transitions with no 13C isotopes in the vicinity of NV centers while orange numbers are for NV centers with one 13C atom nearby.

Laser noises influence on Raman oscillations of rydberg atoms

A.P.Gordeev*, **D.Schepanovich, I.B.Bobrov, Kovlakov E.V., Straupe S.S., Kulik S.P.**

Quantum technology centre, Faculty of Physics M.V. Lomonosov Moscow State University, Moscow, Russia
*E-mail: ar1emg0rdeev@gmail.com

Abstract

One of the factors restricting fidelity of quantum gates implementation in quantum computers based on cold atoms is laser technical noise. This work presents methods for measuring laser noises via signal from Pound–Drever–Hall system and heterodyne spectroscopy and provides a numerical model of rydberg atom excitation by solving Schrodinger equation using electric field noises recreated from experimental data in order to estimate quantum gate fidelity.

Rydberg atoms are promising platform for quantum simulation and computing as well as rydberg blockade is a practical way to entangle qubits by exciting high n states in two atoms simultaneously. Error sources for these systems are the following: finite lifetime of atomic states, Stark effect, thermal motion of atoms and noises in laser radiation. We provide description of experimental setup (detailed specification will be shown during presentation) for lasers' noise measurement and numerical simulation of Raman oscillations.

For practical purposes we used 2 lasers (red and blue) to excite rydberg states. Lasers' noise spectra were obtained via three methods: measurement of laser intensity with fast photodiode (so called intensity noise), heterodyne spectroscopy (lasers' spectra)[1] and signal from PDH-locking system (frequency noise spectra[2]).

For numerical simulation of the process there are two possible ways. First is to directly solve Schrodinger's equation for three level atom with following Hamiltonian

$$\widetilde{H} = UHU^\dagger + i\hbar\partial_t(U)U^\dagger =$$

$$= \begin{pmatrix} 0 & 0 & \sum \Omega_{1,i}e^{-i\Delta_{1,i}t+\phi_{1,i}} \\ 0 & 0 & \sum \Omega_{2,i}e^{-i\Delta_{2,i}t+\phi_{2,i}} \\ \sum \Omega_{1,i}e^{i\Delta_{1,i}t-\phi_{1,i}} & \sum \Omega_{2,i}e^{i\Delta_{2,i}t-\phi_{2,i}} & 0 \end{pmatrix},$$

where $\Delta_{1(2),i}$ is detuning of i-th spectral component from atomic resonance, $\Omega_{1(2),i}$ - Rabi frequency produced by i-th component, ϕ_i - random phases and indices 1 and 2 correspond to red and blue lasers.

Second way is to use adiabatic approximation[3] reducing three level system to two levels and solve Schrodinger's equation Hamiltonian:

$$\hat{H} = \hat{H}_0 + \hat{H}_1 = \frac{\hbar\Delta}{2}\sigma_z + \frac{\hbar\Omega}{2}\sigma_x + \frac{\hbar\nu(t)}{2}\sigma_z + \frac{\hbar\Omega\varepsilon(t)}{2}\sigma_x,$$

where $\nu(t)$, $\varepsilon(t)$ - functions proportional to oscillation of frequency and amplitude of lasers with mean values equal to 0. This method allows to compare modeling result with perturbation theory results[4] applied to two level system.

Using numerical simulation we demonstrated insignificant influence of low-frequency (intensity) noise and high-frequency ($>$ 10 MHz) noise in our experimental setup, whereas mid-frequency noises have considerable impact which can be reduced from 0.2% to 0.1% infidelity for red laser and from 0.5% to 0.3% by adding Fabri-Perot resonator to the model. Comparison with alternative theories gave estimations of $\sim$ 1% errors for high-frequency and also an insignificant influence of low-frequency noise [5].

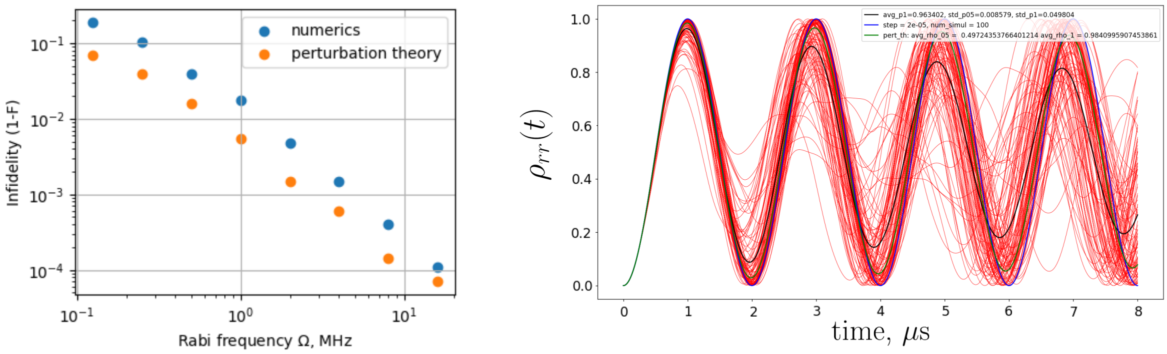

Figure 1: (a) - Infidelity of π-impulse at different Rabi frequencies in comparison with perturbation theory, (b) - Evolution of rydberg state obtained by numerics (Rabi freuency $\Omega = 0.5$ MHz). Red lines corresponds solutions with different sets of random phases ϕ_i, black line is their average, blue line shows evolution without noise and green line represents perturbation theory for red laser spectra measured from PDH-locking signal.

References

[1] *Hanne Ludvigsen and Mikael Tossavainen and Matti Kaivola*, Laser linewidth measurements using self-homodyne detection with short delay. **180-186**, 155 (1998)

[2] *E. Black*, An introduction to Pound-Drever-Hall laser frequency stabilization. American Journal of Physics **79-87**, 69 (2001).

[3] *D.A. Steck*, Quantum and Atom Optics, **269** (2007).

[4] *A. Kale*, Towards High Fidelity Quantum Computation and Simulation with Rydberg Atoms. Defended 5 June 2020.

[5] *X.Jiang, J.Scott, M.Friesen, M. Saffman*, Sensitivity of quantum gate fidelity to laser phase and intensity noise, arXiv:2210.11007v2 (2022)

Integrated photonics as an element base of promising infocommunication systems

Grigory Voronkov[1]*, **Yana Aleksakina**[1], **Elizaveta Grakhova**[1], **Ruslan Kutluyarov**[1]

[1] *Ufa University of Science and Technology, Ufa, Russia*
*E-mail: voronkov.gs@ugatu.su

Abstract

The article discusses the concept of integrated photonics, as well as the issue of its importance in modern realities and prospects, provides examples of the work on its basis of various devices (such as liquid, gas and vortex sensors, interrogators, integrated circuits), including modeling, calculation and testing of PIC.

The implementation of various devices using photonic integrated circuits (PICs) or completely based on them is currently the subject of a large number of topical studies. The use of FIS provides an increase in energy efficiency, a reduction in the mass and dimensions of products [1]. In the applications of sensor systems, the use of PSIs makes it possible to implement compact, cheaper mass production, explosion-proof, highly sensitive sensors, the dimensions and characteristics of which provide them with a wide range of applications, including environmental monitoring and medical diagnostics. Such a transition will make devices more flexible and multifunctional, opening a new page in the development of Internet of Things (IoT) systems [2], simplifying their implementation in hazardous industries [3]. In the field of infocommunication technologies (ICT), the volume of transmitted and processed information is constantly increasing, which requires increasing network bandwidth and new approaches to computing. On the one hand, integrated photonic devices provide the necessary speeds, on the other hand, they allow the implementation of a new class of computing devices, including neural networks [4]–[8]. Also, integrated photonics has prospects in the field of quantum systems, since they require ever smaller sizes to implement a system on a chip [9], [10].

The areas of application of PIC use are also shown in Fig.1.

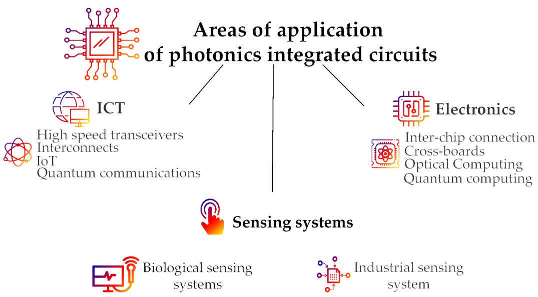

Fig. 1: Areas of application of PIC

The integrated photonic devices that our laboratory is working on are refractive sensors [11], [12], interrogators [11]–[13], and integrated systems in general [11], [12]. The study begins with the calculation stage: the characteristics of the device are calculated and they are optimized for specific tasks. After that, the numerical simulation stage begins in the Ansys Lumerical environment using the Finite-difference time-domain method (FDTD), Interconnect and Mode software modules. This is followed by system modeling, which allows you to evaluate the performance and parameters of the system as a whole. This is followed by the development of the PIC topology for sending to production and subsequent testing. For this, a measuring laboratory is equipped, which includes an experimental setup of an original design for testing FIS, an optical spectrum analyzer, a tunable laser source of optical radiation, a BER tester, an optical oscilloscope.

The laboratory team developed a PIC topology for measuring liquid parameters on a silicon-on-insulator platform, which makes it possible to implement in an integrated form both a sensor and a device for its interrogation [11]. Here, sensitivity to a change in the refractive index was tested, which can be further interpreted as a change in temperature, composition, or concentration of impurities in the liquid. In addition, the structure of the PIC on the silicon-on-insulator platform for a multichannel refractometric sensor system is proposed, which allows you to create fully integrated devices of the "laboratory-on-a-chip" type for use in medical and industrial sensor systems, including systems microfluidics. It should be noted that this scheme differs from its analogues in a non-standard "interrogator-sensor" sequence. PIC topologies on silicon-on-insulator platforms have also been developed for refractometric measurements of the parameters of gaseous media [12]. The possibility of implementing this sensor system on the Si3N4 platform is analyzed. In both cases, gases toxic to humans, such as mercury vapor, nitric oxide, carbon tetrachloride, and others, were considered.

Also, the laboratory developed an innovative system for interrogating integrated sensors [13], based on the use of an optoelectronic oscillator (OEO), which makes it possible to increase the sensitivity of the sensor system by more than 50% compared to the traditional intensity interrogation system.

In addition, fully integrated systems have been developed [11], [12], demonstrating that when using an interrogator based on OEO, not only the polling scheme is simplified, but the quality of the entire system is also improved: the intrasystem detection limit can be reduced by 5 orders of magnitude.

One of the promising areas of work in sensor applications is fiber-optic sensors based on light beams that transfer the orbital angular momentum (vortex beams) to determine various parameters of the medium. Our research laboratory focuses on the prospect of these applications for creating sensors based on photonic integrated circuits [14]–[18]. The principle of measurement is either to analyze the change in the order of the vortex, or to interfere with the optical vortex beam with the Gaussian beam to detect the phase difference. Thanks to these capabilities, OAM beams can be used to develop high-performance sensors.

As part of the research, a non-coherent transceiver was developed that provides a data transfer rate of 200 Gb / s. This speed is achieved using four-level pulse amplitude modulation (PAM4) with frequency and spatial channel multiplexing [19].

Multi-channel interrogation for liquid sensors is currently being researched and high-speed temperature sensors are being calculated. These sensors can be used in medicine [20], [21], in production [3], [22], and in environmental monitoring [23].

The creation of sensor interrogation systems (interrogation) on the PIC allows you to move to fully integrated photonic sensor systems, which allows you to translate integrated photonic technologies into the field of application of Internet of things systems, for which dimensions and energy efficiency are key indicators.

The study was carried out as part of the work on the state assignment of the Ministry of Education and Science of Russia for the Federal State Budgetary Educational Institution of Higher Education "USATU" (scientific topic code ♯/ FEUE-2021-0013, agreement No. 075-03-2021-014) in the youth research laboratory of the REC integrated photonics".

References

[1] *H. Wong, V. Filip, C. K. Wong, and P. S. Chung*, Silicon integrated photonics begins to revolutionize. Microelectronics Reliability **47**, 1 (2007).

[2] *T. H. Szymanski*, Securing the industrial-tactile Internet of Things with deterministic silicon photonics switches. IEEE Access **4** (2016).

[3] *H. Wang et al.*, Gas sensing materials roadmap. J. Phys.: Condens. Matter **33**, 303001 (2021).

[4] *C. Doerr*, Silicon photonic integration in telecommunications. Frontiers in Physics **3** (2015).

[5] *M. Romagnoli et al.*, Graphene-based integrated photonics for next-generation datacom and telecom. Nat Rev Mater **3** (2018).

[6] *Z. Wang, L. Chang, F. Wang, T. Li, and T. Gu*, Integrated photonic metasystem for image classifications at telecommunication wavelength. Nat Commun **13** (2022).

[7] *J. He, T. Dong, and Y. Xu*, Review of Photonic Integrated Optical Phased Arrays for Space Optical Communication. IEEE Access **8** (2020).

[8] *Y. A. Vlasov*, Silicon CMOS-integrated nano-photonics for computer and data communications beyond 100G. IEEE Communications Magazine **50** (2012).

[9] *G. Moody et al.*, 2022 Roadmap on integrated quantum photonics. J. Phys. Photonics **4**, 012501 (2022).

[10] *A. W. Elshaari, W. Pernice, K. Srinivasan, O. Benson, and V. Zwiller*, Hybrid integrated quantum photonic circuits. Nat. Photonics **14** (2020).

[11] *G. Voronkov et al.*, Design and Modeling of a Fully Integrated Microring-Based Photonic Sensing System for Liquid Refractometry. Sensors **22** (2022).

[12] *G. S. Voronkov et al.*, Enhancing the Performance of the Photonic Integrated Sensing System by Applying Frequency Interrogation. Nanomaterials **13** (2022).

[13] *В. В. Иванов et al.*, Частотный интеррогатор на основе фотонной интегральной схемы для оптических датчиков акустической эмиссии. Электромагнитные волны и электронные системы **6** (2022).

[14] *I. V. Stepanov et al.*, Wavelength-Tunable Vortex Beam Emitter Based on Silicon Micro-Ring with PN Depletion Diode. Sensors **22** (2022).

[15] Р. В. Кутлуяров, В. С. Любопытов, Д. М. Фатхиев, И. В. Степанов, and А. Х. Султанов, Генерация сигналов, переносящих орбитальный угловой момент, средствами интегральной фотоники. Материалы IX Молодежной международной научно-технической конференции молодых ученых, аспирантов и студентов "Прикладная электродинамика, фотоника и живые системы-2022" **1** (2022).

[16] *D. M. Fatkhiev, V. S. Lyubopytov, R. V. Kutluyarov, E. P. Grakhova, and A. K. Sultanov*, A Grating Coupler Design for Optical Vortex Mode Generation in Rectangular Waveguides. IEEE Photonics Journal, **13** (2021).

[17] *V. S. Lyubopytov, R. V. Kutluyarov, V. K. Bagmanov, N. Neumann, and A. K. Sultanov*, A Grating Coupler Design for Optical Vortex Mode Generation in Rectangular Waveguides. IEEE Photonics Journal, **13** (2021).

[18] *V. S. Lyubopytov, R. V. Kutluyarov, V. K. Bagmanov, N. Neumann, and A. K. Sultanov*, Modeling and Optimization of Vortex Modes Propagation in Rectangular Dielectric Waveguides. IEEE Photonics Journal, **12** (2020).

[19] *I. V. Stepanov, R. V. Kutluyarov, D. M. Fatkhiev, V. S. Lyubopytov, E. P. Grakhova, and A. Kh. Sultanov*, Integrated Transceiver of Optical Vortex Signals with PAM-4. 2022 IEEE 23rd International Conference of Young Professionals in Electron Devices and Materials (EDM), Altai, Russian Federation (2022).

[20] *G. Yang et al.*, TiO 2 based sensor with butterfly wing configurations for fast acetone detection at room temperature. Journal of Materials Chemistry C, **7** (2019).

[21] *H. Tai, S. Wang, Z. Duan, and Y. Jiang*, Evolution of breath analysis based on humidity and gas sensors: Potential and challenges. Sensors and Actuators B: Chemical, **318**, 128104 (2020).

[22] *J.S. Noh, J. M. Lee, and W. Lee*, Low-Dimensional Palladium Nanostructures for Fast and Reliable Hydrogen Gas Detection. Sensors, **11** (2011).

[23] *Butt, M. A., Voronkov, G. S., Grakhova, E. P., Kutluyarov, R. V., Kazanskiy, N. L., Khonina, S. N.*, Environmental Monitoring: A Comprehensive Review on Optical Waveguide and Fiber-Based Sensors. Biosensors, **12**, 1038 (2022).

The excitation spectrum of a multi-level atom coupled with a dielectric nanostructure

N.A. Moroz[1], **L.V. Gerasimov**[1], **A.D. Manukhova**[2], **and D.V. Kupriyanov**[1,3,*]

[1] *Quantum Technology Centre, M.V. Lomonosov Moscow State University Leninskiye Gory 1-35, 119991, Moscow, Russia*
[2] *Department of Optics, Palacký University, 17. Listopadu 12, 771 46 Olomouc, Czech Republic*
[3] *Department of Physics, Old Dominion University 4600 Elkhorn Avenue, Norfolk, Virginia 23529, USA*
*E-mail: `kupriyanov@quantum.msu.ru`

Abstract

We present a microscopic calculation scheme for the interaction of a single atom with dielectric nanostructures. The proposed scheme is not limited by simplifying assumptions about the initial energy structure of the atom. In addition, the method is applicable to nanostructures of arbitrary geometric configuration. Using illustrative examples, we demonstrate how the original atomic excitation spectrum changes in the presence of the nanostructure.

The coupling of quantum emitters with nanostructures, in particular, of cold atoms with dielectric waveguides and resonators of sub-wavelength scale, considerably extends the existing opportunities of quantum technologies. The directed light emission into a specific scattering channel, with effectively enhanced coupling strength for the interaction of light with atoms, and being controllable at a single photon level, is a crucial requirement for developing the quantum interface units. At present, a number of prototypes of nanophotonic devices which implement the coupling of atoms with microcavities, photonic crystals, and nanofibers, have been fabricated, see recent review [1]. Such physical systems could provide the emission of a single photon and any specific quantum state of light into the stored or guided mode of a mesoscopic cavity or waveguide.

Here we develop a microscopic calculation scheme for the interaction of a single atom with a nanoscale dielectric sample. Our approach expands beyond the common assumptions about atomic energy structure, such as its constraint by two or three levels, and is applicable to nanoscale objects of arbitrary geometric shapes. By several Illustrative examples, we show how the presence of nanostructure dramatically modifies the original atomic excitation spectrum and we present supporting calculations of the respective radiative shifts and decay rates.

This work was supported by the Russian Science Foundation under Grant No. 18-72-10039 and by Rosatom in the framework of the Roadmap for Quantum computing (Contract No. 868-1.3-15/15-2021 dated October 5, 2021 and Contract No.P2154 dated November 24, 2021).

References

[1] *Chang, D. E. and Douglas, J. S. and González-Tudela, A. and Hung, C.-L. and Kimble, H. J.*, Colloquium: Quantum matter built from nanoscopic lattices of atoms and photons Rev. Mod. Phys. **90**, 031002 (2018).

Calculation of quasiprobability distributions of bright "banana" states

Boulat Nougmanov[1*]

[1] *Moscow Institute of Physics and Technology, Dolgoprudny, Russia*
[1] *Russian Quantum Center, Moscow, Russia*
*E-mail: nougmanov.bn@phystech.edu

Abstract

Due to the nonlinear self-phase-modulation effect, coherent states of light in optical media having cubic nonlinearity evolve to non-Gaussian so-called "banana" states. We develop a fast and convenient formalism of calculation of quasiprobability distributions of bright (multiphoton) banana states.

The problem

It is known that when light, prepared in the coherent quantum state, propagates through an optical medium having cubic (Kerr) nonlinearity, its quantum state, due to the self-phase modulation (SPM) effect, evolves into the non-Gaussian so-called "banana state" (this peculiar name is due to the characteristic shape of the corresponding Wigner function). This process can be used for preparation of bright highly nonclassical quantum states of light. Therefore, the problem of calculation of quasiprobability distributions of the "banana" state $|\psi\rangle$ is of significant interest for quantum optics.

For a small number of quanta $|\alpha|^2 \lesssim 10^2$ this problem can be solved by the direct numerical calculation, see Ref. [1]. At the same time, for the large number, $|\alpha|^2 \sim 10^6$, at which nonlinear effects of real crystals are manifested [2], the direct calculation leads to overflow. Here we develop an effective formalism of calculation of quasiprobability distributions of bright (multiphoton) banana states.

Let the state $|\alpha\rangle$ be fed to the input of a crystal with the Kerr nonlinearity. The banana state $|\psi\rangle$ at the output effectively depends on the dimensionless parameter Γ proportional to the time of passage through the crystal [2]. Its Husimi function, being much simpler than the Wigner one from the point of view of the direct calculations, was considered in the work [3]. Its explicit form for the case of the "banana" state is the following:

$$Q(\beta) = \frac{|\langle\psi|\beta\rangle|^2}{\pi} = \frac{e^{-|\alpha|^2-|\beta|^2}}{\pi}\left|\sum_{n=0}^{\infty}\frac{(\alpha\beta^*)^n\, e^{-i\Gamma n(n-1)}}{n!}\right|^2 \tag{1}$$

The direct numerical calculation of this function according to these formulas require the summation of $O(|\alpha|)$ terms (taking into account that the most meaningful part of the Husimi function is in the region $|\beta| \sim |\alpha|$).

Here we propose an asymptotic approach to calculating quasi-probability functions, increasing the calculation speed of the Husimi function to $O(1)$ and the Wigner function to $O(\alpha)$. The calculations will be carried out in two stages: first, we find the asymptotics of the Husimi function at $\left|\alpha^2\Gamma\right| \gtrsim 1$, and then we find a decomposing the Wigner function into a series consisting of the values of the Husimi function.

Husimi and Wigner functions

The series (1) can be converted to an integral:

$$\sum_{n=0}^{\infty}\frac{(\alpha\beta^*)^n\, e^{-i\Gamma n(n-1)}}{n!} = \frac{e^{-\frac{i\pi}{4}}}{2\sqrt{\pi\Gamma}}\int\limits_{-\infty}^{\infty}\exp\left(i\frac{z^2}{4\Gamma} + \alpha\beta^* e^{i\Gamma + iz}\right)dz\,. \tag{2}$$

To calculate this intergral, the saddle-point method can be used. The greatest difficulty from the point of view of mathematics here is the deformation of the integration contour passing through an infinite set of the saddle points, see Fig. 1. However, examination of the obtained expressions shows that the

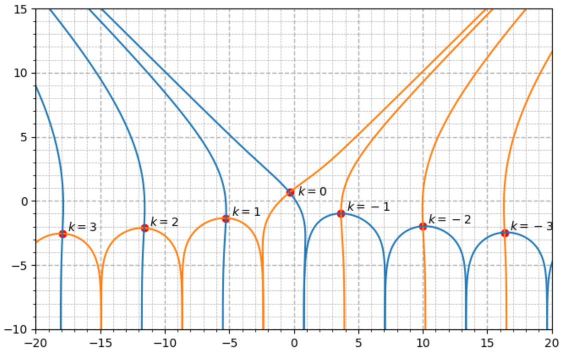

Figure 1: Red dots mark the points of the pass in (2) at $\Gamma\alpha\beta^* e^{i\Gamma} = \frac{e^{-\frac{i\pi}{4}}}{\sqrt{2}}$. Blue indicates the curves of the steepest descent at $\Gamma < 0$ and orange at $\Gamma > 0$.

main contribution is made by the pass through only one of the saddle points. Therefore, Eq. (2) can be converted to

$$\sum_{n=0}^{\infty} \frac{(\alpha\beta^*)^n e^{-i\Gamma n(n-1)}}{n!} = e^{\frac{i\pi}{4}} \frac{\exp\left(\frac{i - i\left(W_{\bar{k}}\left(2\Gamma i\alpha\beta^* e^{i\Gamma}\right)+1\right)^2}{4\Gamma}\right)}{\left(-i - iW_{\bar{k}}\left(2\Gamma i\alpha\beta^* e^{i\Gamma}\right)\right)^{\frac{1}{2}}} \left(1 + O(\Gamma^2)\right) \tag{3}$$
$$\bar{k} = -\operatorname{sgn}\Gamma\left[\frac{1}{2\pi}\left(2|\Gamma\alpha\beta^*| + \left|\arg\left(\Gamma\alpha\beta^*\right) + \frac{\pi}{2}\operatorname{sgn}\Gamma\right|\right)\right],$$

reducing the complexity of calculations to $O(1)$. Here W_k are the branches of Lambert W function.

Strictly speaking, the real complexity is $O(1+|\alpha\Gamma|)$. However, under the condition of $|\alpha\Gamma| \ll 1$, which is met when $|\alpha| \sim 10^3$ and $|\Gamma| \sim 10^{-6}$, it is possible to neglect members of the order of $O(e^{-\left(8\pi|\alpha\Gamma|^2\right)^{-1}})$ compared to $O(\Gamma^2)$.

We use a simple connection between the Husimi and Wigner functions through characteristic functions or, equivalently, through the Fourier transform:

$$C_s(z) = \mathcal{F}\{W\}(z) = e^{\frac{|z|^2}{2}}\mathcal{F}\{Q\}(z) = e^{\frac{|z|^2}{2}}C_a(z), \tag{4}$$

where C_s and C_a are the symmetric-ordered and antinormally-ordered characteristic function of the quantum state. Substituting the Husimi function in the form (1) and taking numerous Gaussian integrals, we reduce the calculation of the Wigner function to a one-time summation:

$$W(\beta) = 2e^{2|\beta|^2} \sum_{m=0}^{\infty} \frac{\left(-|\alpha|^2\right)^m}{m!} Q(2\beta e^{2i\Gamma m}) \tag{5}$$

This expression uses the values of the Husimi function, which generated in the previous step and it can be cast to a form that does not lead to overflow.

References

[1] *Stobińska, Magdalena*, Wigner function evolution of quantum states in the presence of self-Kerr interaction. Phys. Rev. A. Vol. 78. — P. 013810, (2008)

[2] *SN Balybin, F Ya Khalili, DV Strekalov et al.*, On perspectives of generating quasi-Fock state via resonant self-phase-modulation. Quantum and Nonlinear Optics VII / SPIE. — Vol. 11558 — Pp. 9–24, (2020)

[3] *Miranowicz, A., R. Tanas, and S. Kielich*, Generation of discrete superpositions of coherent states in the anharmonic oscillator model. Quantum Optics: Journal of the European Optical Society Part B 2.3: 253, (1990)

Resonant Laser Excitation of the Luminescence of Silicon-Vacancy centers in Nanodiamonds at Low Temperature

Dmitrii Pasternak[1*], **Dmitry Kalashnikov**[2], **Victor Leong**[2], **Claven Chia**[2], **Alexey Romshin**[1], **Sergey Kuznetsov**[1], **Artem Martyanov**[1], **Vadim Sedov**[1], **Leonid Krivitsky**[2], **Igor Vlasov** [1]

[1] *Prokhorov General Physics Institute of the Russian Academy of Sciences, 38 Vavilova str, Moscow, Russia*
[2] *Institute of Materials Research and Engineering Agency for Science Technology and Research (A*STAR), Singapore*
*E-mail: dg.pasternak@physics.msu.ru

Abstract

The application of the technique of resonant laser excitation of photoluminescence at low temperatures using a narrow-band tunable laser significantly expands the possibilities of spectral investigation of individual luminescent centers in nanodiamonds, even in conditions of high concentrations of such centers. In this paper, a comparative analysis of the spectral characteristics of individual Silicon-Vacancy centers (SiVs) in spontaneously nucleated CVD nanodiamonds grown on germanium and silicon substrates is carried out. Studied nanoparticles have a characteristic size of 300 nm and contain large ensembles of SiV centers. It was found that during the transition from silicon substrates, which are traditionally used in the CVD synthesis of diamonds, to germanium substrates, the spectral characteristics of the photoluminescence of SiV centers almost do not change.

1. Introduction

Negatively charged Silicon-Vacancy centers (SiV), along with other luminescent point defects in diamond, are extremely popular sources of both single-photon and classical radiation in the visible spectral region, respectively, for quantum and biomedical technologies [1-4]. The most common method of synthesis SiV-containing diamonds is Chemical Vapor Deposition (CVD)method. Usually, in the CVD synthesis of both individual diamond particles and polycrystalline films, pre-seeding of the substrate on which the synthesis takes place with ultra-small diamond nanoparticles is used. Recently, for the production of luminescent diamond nano- and micro-particles, scientific groups from Russia and France have been actively developing alternative approaches based on spontaneous diamond nucleation under CVD synthesis conditions [5-6], which was first described in the work of Professor B.N. Spitsyn et al. [7]. In this paper, a comparative analysis of the spectral characteristics of individual SiV centers in spontaneously nucleated CVD nanodiamonds grown on germanium and silicon substrates is carried out. The studied nanoparticles have a characteristic size of 300 nm and contain large ensembles of SiV centers. Nevertheless, the low temperature (15 K) and resonant laser excitation of luminescence make it possible to characterize individual SiV centers.

2. Experimental Methods

Synthesis of nanodiamond (ND) particles doped with silicon was carried out in the microwave CVD reactor “ARDIS-100” (Optosystems Ltd.). Polished Si (100) and Ge (111) plates were used as substrates. Further, for convenience, we will call NDs grown on silicon - “Si”-ND, and on Germany - ”Ge”-ND. Both types of samples were grown in the mode of spontaneous nucleation of diamond on the surface of germanium and silicon substrates [6]. To stimulate diamond nucleation on the Ge surface, the substrates were treated in a 25% aqueous ammonia solution before synthesis: the substrates were dipped into an ammonia solution for a few seconds, then washed in distilled water and dried. For the CVD synthesis of ND, a methane/hydrogen gas mixture was used at a pressure of 75 torr. In preliminary experiments, we found that with a volume ratio of $CH_4/H_2 = 6\%$ the maximum possible nucleation density of diamond particles on both substrates is achieved, and this ratio was chosen for the synthesis of ND. The temperature of the substrates during the growth of NA was measured with a Micron M770 pyrometer. The formation of SiV centers in the "Si"-ND was carried out mainly due to uncontrolled etching of the Si substrate in hydrogen plasma. In the "Ge" sample, the formation of SiV occurred when a small amount of silane (SiH4) was added to the methane-hydrogen mixture, which made it possible to control the formation of luminescent centers in this sample. The main parameters of CVD growth on two different substrates are shown in Table 1.

Table 1: CVD growth condition.

Substrate	Gas pressure [torr]	Microwave plasma power [kW]	CH4/H2 [%]	Source of Si [%]	Growth time [min]	Substrate temperature [oC]
Si	75	3	6	Silicon substrate etching	15	850
Ge	75	3	6	SiH4/CH4=0.1	20	800

A Jeol 7001F scanning electron microscope (SEM) was used to determine the morphology and lateral size of the grown specimens.

The spectral characteristics of photoluminescence (PL) of SiV centers were studied at cryogenic temperatures in the modes of non-resonant and resonant laser excitation. In the first mode, the PL was excited by a diode laser at a wavelength of 660 nm (L660P120, Thorlabs). In the second mode, a tunable continuous Ti: Sapphire laser (Solstice, MSquared) with a line width of less than 5 MHz and a tunable wavelength range from 700 to 800 nm was used. For cooling, the sample was placed in a closed-cycle cryostat chamber (attoDRY 800, Attocube). The temperature of the sample holder has stabilized at 15,0 with a precision of 0,1 K. The cryostat was combined with a homemade confocal scanning microscope. The pump laser beam was focused on the sample using a cryo-compatible microscope lens (x 100, NA= 0.82, Attocube). The position of the pumping laser beam on the sample was controlled using a galvo mirror (FSM 300, Newport). The PL signal was collected into a single-mode fiber (SM600, Thorlabs), and then directed either to a single-photon avalanche photodetector (SPAD, SPCM-AQRH-15, Perkin Elmer) or to a spectrometer (IsoPlane 160, with a resolution of 0.07 nm, Princeton Instruments). In an experiment with resonant excitation, the PL spectra were recorded based on the dependence of the intensity of the phonon component of the PL (30% of the total radiation), which was isolated using filter sets in the range of 750-795 nm, on the wavelength of the exciting radiation in the range of 700-750 nm. For express recording of resonant spectra, the step size was 500 MHz, for recording high-resolution spectra - 40 MHz. The second-order autocorrelation function g^2 (t) was determined using a standard Brown-Twiss interferometer using a time-to-digital converter (quTAU) with a time resolution of 81 ps.

3. Results and Discussions

The synthesis time was chosen in such a way that the characteristic sizes of individual diamond particles on both substrates were close to 300 nm. This size is chosen for the convenience of optical visualization and identification of the studied particles during the transition from one method of their characterization to another. The SEM images of the analyzed samples confirm that the NDs grown on Si and Ge substrates have a characteristic size of about 300 nm (Figure 1a and 1b, respectively). Note that the morphology of "Ge" - ND particles is somewhat different from "Si" - ND: the Ge substrate is dominated by particles having a polycrystalline structure, whereas the Si substrate is dominated by particles with a well-defined singular facet, i.e., single crystals.

Before cooling, the PL spectra of the samples were recorded at room temperature under laser excitation at a wavelength of 532 nm. It was found that the ratio of the peak intensity of the SiV zero-phonon (ZPL) line near 738 nm to the intensity of the raman scattering line of diamond (at raman frequency of 1332 cm-1) for a number of studied nanoparticles on both substrates varied from 2 to 7, which indicates a close degree of silicon doping of both samples on.

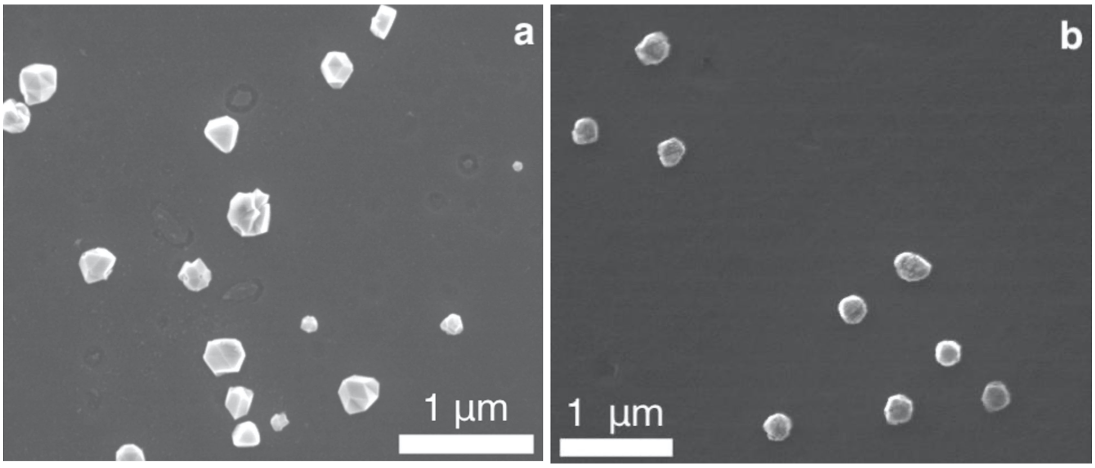

Figure 1: SEM-images of CVD ND particles grown on Si (a) and Ge (b) substrates

Characteristic PL spectra recorded in the mode of non-resonant laser excitation with a power of 1 mW at a wavelength of 660 nm at 15 K for individual particles on "Si" - ND and "Ge" - ND are shown in Figures 2a and 2b, respectively. In the spectra, there are many non-overlapping and overlapping narrow lines in the range of 735-750 nm, which indicates a high content of SiV centers in one 300-nm particle. The frequency distibution of individual SiV emitters within a single particle is explained by the presence of internal local stresses in it [6]. This fact facilitates the observation of luminescence lines from individual SiV even when working with sufficiently large ensembles of these centers. Nevertheless, the spectral resolution of the spectrometer (0.13 nm) used to register SiV FL under non-resonant excitation significantly exceeds the minimum possible line width (approximately 100 MHz) from individual SiV, which does not allow for detailed investigation of their spectral characteristics.

The application of the technique of resonant excitation of PL using a narrow-band tunable laser with a line width of 5 MHz significantly expands the possibilities of spectral study of individual SiV centers. The PL spectrum recorded with a large scanning step (see details in Section 2) with resonant excitation in the range of 735-740 nm is shown in Figure 2c. Note that the spectra in Figures 2b and 2c are shown for the same particle on Ge. There is significantly less overlap between individual lines than in the case of non-resonant excitation: the lines with the smallest width are more likely to belong to separate SiV centers. Figures 2d and 2e show the spectra obtained with a small scanning step for the narrowest luminescence lines in the samples "Si" - ND and "Ge" - ND, respectively. The spectra were recorded at the maximum power of resonant excitation, which does not cause broadening of the spectral line due to heating of the sample: approximately 100 nW. From the approximation of SiV-lines by the Lorentz profile, it follows that their FWHMs are close for both samples and are about 2.1 GHz (for Si) and 2.6 GHz (for Ge).

To prove that the selected SiV lines really correspond to single emitters, their polarization sensitivity was analyzed (Figure 2f) and the second-order autocorrelation function (g^2 (t)) was measured (Figure 2g). For the polarization measurements, a half-wave plate was used to rotate the polarization angle of the laser radiation in the sample plane. For an individual SiV center, which is a radiating dipole, a sinusoidal change in the intensity of the observed luminescence is expected when the polarization angle of the exciting radiation changes. Indeed, the PL line shown in Figure 2e demonstrates high polarization sensitivity (Figure 2f). For the same SiV line, the measured depth of failure of the second-order autocorrelation function exceeded 50%, which satisfies the criterion of a single-photon source (Figure 2g).

We also note the extremely high photostability of the studied SiV lines: their short-term blinking is insignificant; the initial intensity level is maintained for tens of hours of laser irradiation.

4. Conclusions

A comparative analysis of the characteristic spectral position and luminescence linewidth of individual SiV centers within a single diamond nanoparticle for CVD ND samples grown on germanium and silicon substrates has been carried out. It is shown that during the transition from silicon substrates, which are

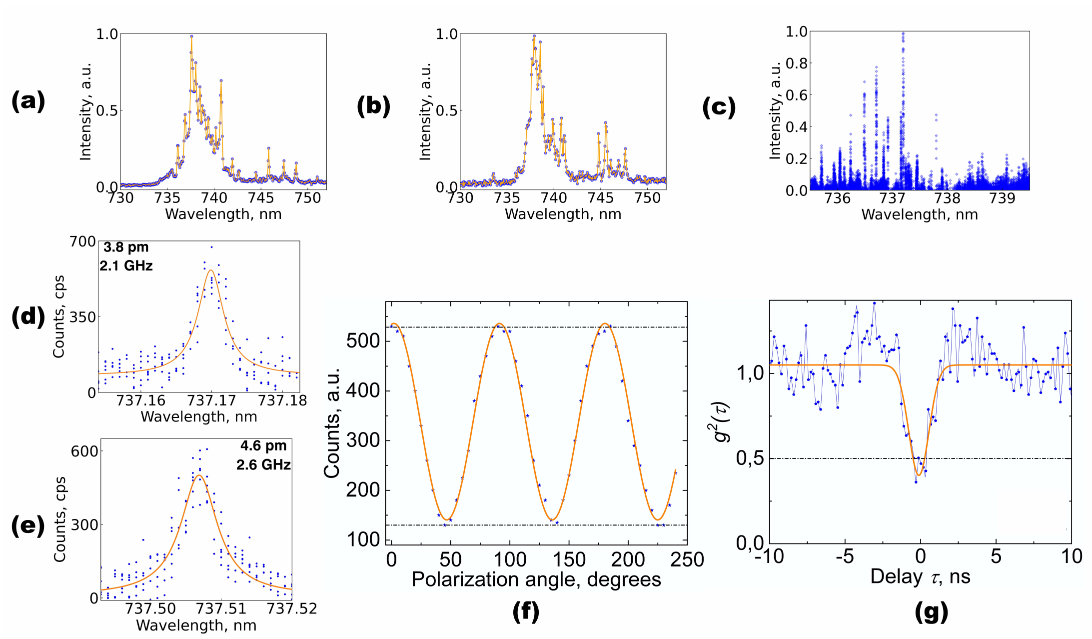

Figure 2: Characterization of the SiV-luminescent properties of individual color centers in NDs at low temperature. PL spectra under non-resonant excitation with a continu¬¬ous laser with a wavelength of 660 nm for a single diamond nanoparticle of about 300 nm in size on Si (a) and Ge (b) substrates. An example of a characteristic PL (c) spectrum recorded at a large scanning step by resonant laser excitation in the spectral range of 735-740 nm. Profiles of SiV-lines of individual centers in NDs on Si (d) and Ge (e) substrates recorded with high spectral resolution during resonant laser scanning. Polarization sensitivity (f) of a single SiV line shown in graph (e). Second-order autocorrelation function g^2 (t) (g), confirming the targeted spectral reference to a single-photon SiV source, with a spectrum (e) under resonant laser excitation. All experimental data presented in graphss (a-g) are represented by blue dots, while: in the case of (a) and (b) – experimental data are connected by orange lines for clarity, for graphs (d-g), approximation dependencies are represented by orange contours.

traditionally used in the CVD synthesis of diamonds, to germanium substrates, the spectral characteristics of the photoluminescence of SiV centers practically do not change. At the same time, the usage of Ge substrates with weak adhesion to diamond opens up new opportunities in the formation of SiV centers and their application: it allows controlled doping of NDs with silicon, facilitates the transfer of diamond particles from the growth substrate into optical chips, microresonators, photonic crystals and other photonic circuits. It should also be noted that individual SiV centers formed in CVD diamond nanoparticles, due to their high photostability and rather narrow width of the luminescence line, are promising candidates for creating single photon sources based on them, operating at room temperatures.

Acknowledgements

The research was partially carried out at the expense of the grant of the Russian Science Foundation No. 22-19-00324 (I.I.Vlasov)

Conflict of Interest

The authors declare no conflict of interest.

References

[1] *F. Jelezko, J. Wrachtrup*, Single defect centres in diamond: A review. physica status solidi (a) **203**, 017402 (2006).

[2] *O.A. Shenderova, A.I. Shames, N.A. Nunn, M.D. Torelli, I.I. Vlasov, A. Zaitsev*, Review Article: Synthesis, properties, and applications of fluorescent diamond particles. Journal of Vacuum Science and Technology B **37**, 030802 (2019).

[3] *M. K. Bhaskar, R. Riedinger, B. Machielse, D. S. Levonian, C. T. Nguyen, E. N. Knall, H. Park, D. Englund, M. Lončar, D. D. Sukachev, M. D. Lukin*, Experimental demonstration of memory-enhanced quantum communication. Nature **580**, 60 (2020).

[4] *K. Bian, W. Zheng, X. Zeng, X. Chen, R. Stöhr, A. Denisenko, S. Yang, J. Wrachtrup, Y. Jiang*, Nanoscale electric-field imaging based on a quantum sensor and its charge-state control under ambient condition. Nature Communication **12**, 2457 (2021).

[5] *M. Feudis, A. Tallaire, L. Nicolas, O. Brinza, P. Goldner, G. Hétet, F. Bénédic, J. Achard*, Large-Scale Fabrication of Highly Emissive Nanodiamonds by Chemical Vapor Deposition with Controlled Doping by SiV and GeV Centers from a Solid Source. Advanced Materials Interfaces **7**, 1901408 (2019).

[6] *D.G. Pasternak,J. Dai,D.A. Kalashnikov,V.S. Sedov,A.K. Martyanov,V.G. Ralchenko,L.A. Krivitsky,I.I. Vlasov*, Low-Temperature Silicon-Vacancy Luminescence of Individual Chemical Vapor Deposition Nanodiamonds Grown by Seeding and Spontaneous Nucleation. Physica status solidi (a) **218**, 2000274 (2018).

[7] *B.V. Spitsyn, L.L. Bouilov, B.V. Derjaguin*, Vapor growth of diamond on diamond and other surfaces. Journal of Crystal Growth **52**, 219 (1981).

X-rays in diamond photonics: a new way to control charge states of color centers

Eduard Sektarov[1,2*], Vadim Sedov[3],
Viktor Ralchenko[3], Kirill Boldyrev[1,2]

[1] *Institute of Spectroscopy of the Russian Academy of Sciences, Troitsk, Moscow, Russia*
[2] *Higher School of Economics, Moscow, Russia*
[3] *Prokhorov General Physics Institute, Russian Academy of Sciences, Moscow, Russia*
*E-mail: sektarov_es@mail.ru

Abstract

This work is focused on the investigation of the X-ray's interaction with the color centers charge states in diamond. We show that X-rays irradiation of diamond can changes the charge states of its defects, including Silicon-Vacancy (SiV) and Nitrogen-Vacancy (NV) color centers. Low-temperature absorption spectra are shown that negatively charged SiV^- and NV^- centers partially transform into neutrally charged SiV^0 and NV^0 centers, accordingly. In addition, we registered new absorption lines, which may belong to other charge states of color centers. The results open a new way for the study of charge states for defects in diamonds and control the charge state of color centers for diamond-based quantum optics.

Crystals with color centers are widely used in various fields of industry and science. They can be applied to optical quantum memory, quantum sensorics and quantum cryptography. Color centers are a defect in the crystal lattice that absorbs and/or radiates in the wavelength range outside the intrinsic absorption of the crystal. In this work, we studied the charge states changing of nitrogen (NV) and silicon-centers (SiV) before and during irradiation with X-rays. The study of color centers in the X-rays was carried out on a Bruker IFS 125HR high-resolution Fourier spectrometer with a cryogenic attachment based on an X-ray tube BSV-30 with a copper anode, with a nominal power of 500 W and a characteristic radiation Cu Kα 8027 eV. The results of the research were absorption spectra obtained at a temperature of 10 K. The absorption method is a well-resolved structure of lines in the spectra, which makes it possible to quantify the concentration of color centers. The obtained spectra illustrate that after X-ray exposure, the absorption line intensities change at wavelengths of 946 nm (SiV^0), 737 nm (SiV^-), 575 nm (NV^0), 637 nm (NV^-) corresponding to color centers. A change in the SiV and NV centers was noted, the increase in the concentration of SiV^0 is proportional to the decrease in SiV^-. A more complex interaction is observed between NV^0 and NV^- because other charge states such as NV^+, NV^{2+} or unknown states may be involved in the process as the appearance of new lines after irradiation was found. For samples with NV and SiV, changes in defect concentrations (x) were calculated using formula 1) from [1]. Calibration coefficients k_{zpl} [1] for SiV and [2] for NV, the integral intensity I_{zpl} of absorption lines was calculated using the OPUS software.

$$I_{zpl} = k_{zpl} x, \tag{1}$$

Acknowledgement

This work was supported by the grant of the Russian Science Foundation No. 19-72-10132.

References

[1] *U. F. S. D'Haenens-Johansson, A. M. Edmonds, M. E. Newton, J. P. Goss, P. R. Briddon, J. M. Baker, P. M. Martineau, R. U. A. Khan, D. J. Twitchen, and S. D. Williams*, EPR of a defect in CVD diamond involving both silicon and hydrogen that shows preferential alignment. Phys. Rev. B. **82**, 155205 (2010).

[2] *G. Davies*, Current problems in diamond: towards a quantitative understanding. Physic: Condensa. Matter **273**, 15 (1999).

[3] E. Sektarov, V. Sedov, V. Ralchenko, K. Boldyrev, X-Rays in Diamond Photonics: A New Way to Control Charge States of Color Centers. phys. status solidi (a), 2200283 (2022)

Reducing current crowding effect with diamond-shaped nanowire for superconducting single photon detectors

I.A. Stepanov[1,2], **E.V. Sergeev**[1,2], **D.V. Kushnev**[2], **A.S. Baburin**[1,2], **S.S. Avdeev**[1,2], **A.O. Melekhina**[2], **I.A. Ryzhikov**[2], **and I.A. Rodionov**[1,2]

[1]*Dukhov Automatics Research Institute, Federal State Unitary Enterprise, (VNIIA), Moscow, Russia*
[2]*FMN Laboratory, Bauman Moscow State Technical University, Moscow, Russia*
*E-mail: `stepanovia@bmstu.ru`

Abstract

A diamond-shaped SNSPD nanowire is proposed to reduce current crowding. It is experimentally proven that in diamond-shaped nanowire current crowding is less observed compared to the meander and spiral nanowire, that makes it the most preferable for SNSPDs with high detection efficiency and low dark count rate.

Superconducting nanowire single photon detectors (SNSPDs) are currently known for their outstanding characteristics, such as high detection efficiency, low jitter, high count rates and low dark count rates. However, it is still a challenge to achieve high detection efficiency with a low dark count rate. One of the main factors limiting these characteristics is the presence of regions with increased current density at nanowire bends, also known as current crowding effect. It appears predominantly in the bends of the traditional meander nanowire. Areas with increased current density reduce the critical current of the nanowire, which makes it impossible to bias SNSPD with a current sufficiently close to the depairing current on a straight section of the nanowire. Since the detection occurs predominantly in the straight section of the nanowire, current crowding significantly reduces the detection efficiency. Furthermore, in regions with an increased current density, the barrier to the entry of vortices into the nanowire is reduced, and therefore the current crowding increases the dark count rate [1]. To achieve high SNSPD performance it is important to optimize the geometry of the nanowire to reduce current crowding.

There are plenty of published methods for reducing the current crowding, including spiral nanowires [2] or meander with variable thickness [3, 4]. These methods still have some issues to be solved. The spiral includes an area in the center with poor properties for detection, which reduces the detection efficiency when positioning the fiber in the center of the active area. The nanowires with variable thickness suffer from the complexity of fabrication, which could lead to low reproducibility of the technology.

Diamond-shaped nanowire

We have previously proposed a new SNSPD diamond-shaped nanowire topology capable of reducing current crowding without complicating the fabrication technology [5]. Moreover, diamond nanowire allows to increase the filling factor without increasing current density at the bends. Fig. 1(a) shows overall view of diamond-shaped nanowire.

To reduce current crowding, at each bend the cross-sectional area is increased due to nanowire broadening and the inner radius is increased as shown in Fig. 1(b, c). We expect that due to the described geometric features the maximum current density at the bend will be close to the current density in the straight section, thus, the bias current will not be limited by the current crowding effect.

Device fabrication

To prove that diamond-shaped nanowire can most effectively suppress the current crowding effect, a sample was made, including four SNSPD topologies: meander, spiral, diamond, and a bridge as a reference. The critical current of a bridge is determined by the properties of the material as well as the cross-sectional area, while in other nanowire topologies the critical current also depends on the current crowding due to the presence of bends. All fabricated nanowire topologies had the same width, so the difference in critical currents will only defined by the current crowding effect.

Sample fabrication began with the deposition of an ultrathin NbN film on a Si substrate by reactive magnetron sputtering. Estimated film thickness was 5 nm. After that, contact pads were formed. Then

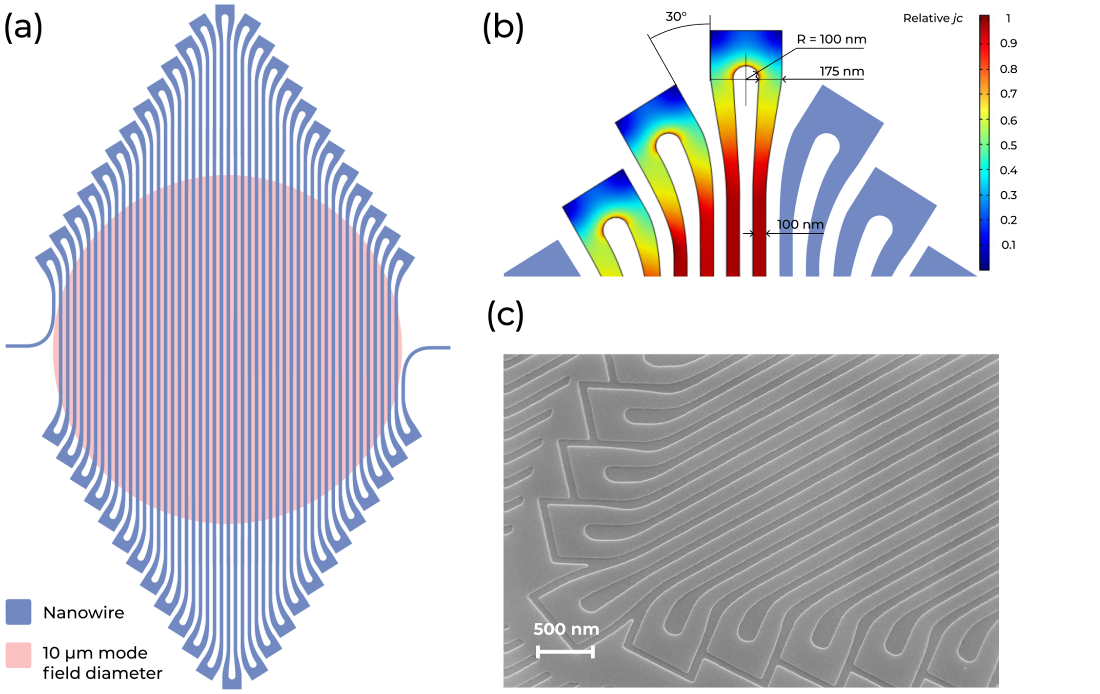

Figure 1: (a) Overall view of diamond-shaped nanowire. (b) Simulated current density distribution on a fragment of the diamond-shaped nanowire. (c) SEM-image of a fragment of diamond-shaped nanowire

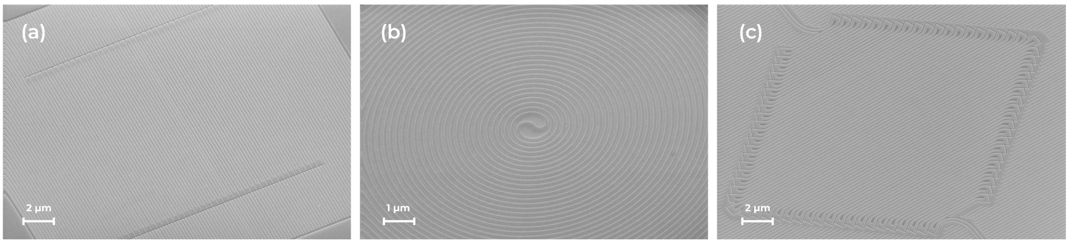

Figure 2: SEM-images of fabricated structures: (a) meander, (b) spiral, (c) diamond

four nanowire topologies were written using electron beam lithography and patterns were transferred to the NbN film using reactive ion etching. Fig. 2 shows SEM-images of fabricated structures.

Measurement setup

To evaluate the effect of current crowding on a bias current limit, the critical currents of four structures were measured. Measurements were performed at 2.5 K in a closed-cycle cryostat. The current was applied to the sample and the voltage was measured by a current source using the four-probe method. A self-made commutation box provided the ability to switch lines from the source to the required structure in the cryostat to provide measurement of four topologies in one cooldown cycle. Measurement setup is shown in Fig. 3.

Results and discussion

We have measured the critical currents of the meander, spiral and diamond nanowires to compare their relative currents, i.e. the ratio of the critical current of the structure to the critical current of the

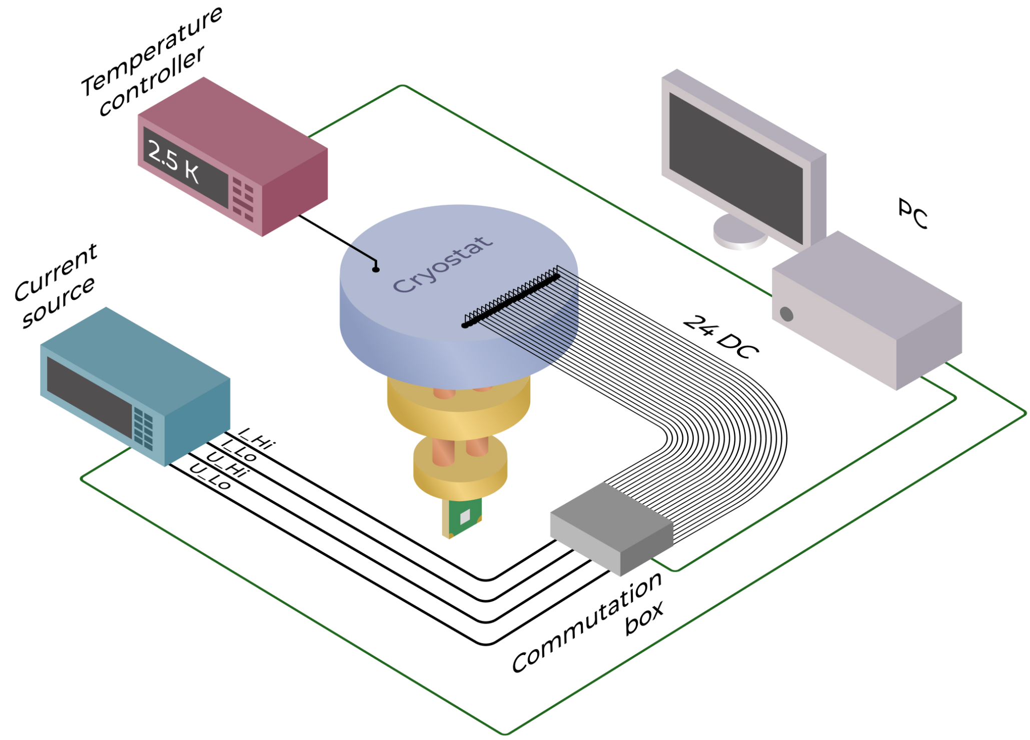

Figure 3: Critical current measurement setup

bridge. Since the decrease in the critical current of different topologies relative to the bridge is associated with current crowding, the closer the critical current of the topology is to the critical current of the bridge, the less current crowding is present in it.

As expected, the bridge showed the highest critical current, and the diamond-shaped nanowire showed the one closest to it.

The experiment results showed that the current crowding effect is least observed in diamond-shaped nanowire, which makes it the most preferable for the creation of SNSPD with high detection efficiency and a low dark count rate.

Conclusion

We have demonstrated that the current crowding is less observed in the diamond nanowire compared to the traditional meander and spiral, which makes its usege for SNSPD the most justified.

Devices were made at the BMSTU Nanofabrication Facility (FMN Laboratory, FMNS REC, ID 74300).

References

[1] *J. Clem, and K. Berggren*, Geometry-dependent critical currents in superconducting nanocircuits. Physical Review B **84**, 174510 (2011).

[2] *I. Charaev, A. Semenov, S. Doerner, G. Gomard, K. Ilin, and M. Siegel*, Current dependence of the hot-spot response spectrum of superconducting single-photon detectors with different layouts. Superconductor Science and Technology **30**, 025016 (2016).

[3] *R. Baghdadi, E. Schmidt, S. Jahani, I. Charaev, M. Müller, M. Colangelo, D. Zhu, K. Ilin, A. Semenov, Z. Jacob, M. Siegel, and K. Berggren*, Enhancing the performance of superconducting nanowire-based detectors with high-filling factor by using variable thickness. Superconductor Science and Technology **34**, 035010 (2021).

[4] *J. M. Xiong, W. J. Zhang, G. Z.Xu, L. X. You, X. Y. Zhang, L. Zhang, C. J. Zhang, D. H. Fan, Y. Z. Wang, L. Hao, and Z. Wang*, Reducing current crowding in meander superconducting strip single-photon detectors by thickening bends. Superconductor Science and Technology **35**, 055015 (2022).

[5] *I. A. Stepanov, V.A. Zheltikov, E.V. Sergeev, A.S. Baburin, S.S. Avdeev, A. O. Melekhina, I.A. Ryzhikov, and I.A. Rodionov*, Superconducting Single-photon detector design optimization. International Conference Laser Optics (ICLO), IEEE (2022)

Atom Chip Loading from Atomic Beam

D. V. Bykova[1,2*], P. I. Skakunenko[1,3,4], A. E. Afanasiev[1], A. S. Kalmykov[1], V. I. Balykin[1]

[1]*Institute of Spectroscopy, Russian Academy of Sciences, Troitsk, Moscow, Russia*
[2]*National Research University Higher School of Economics, Moscow, Russia*
[3]*Moscow Institute of Physics and Technology (National Research University), Dolgoprudnyi, Moscow region, Russia*
[4]*Skolkovo Institute of Science and Technology, Skolkovo, Moscow, Russia*
*E-mail: dvbykova@edu.hse.ru

Abstract

For quantum sensors based on an atomic chip it is necessary to reduce the cooling time for an ensemble of localized atoms in order to increase the accuracy of the sensors. This can be achieved by using a load from a beam of pre-cooled atoms. However, due to beam expansion, atoms are trapped inefficiently. It is proposed to use focusing of a low-velocity atomic beam into the trapping region of a chip, based on a two-dimensional magneto-optical trap (2D MOT) in the beam propagation path. Calculations show that for effective focusing to a region of a characteristic size of about 1 mm, it is necessary to use the sub-Doppler cooling in a 2D MOT, since the momentum diffusion decreases at a larger frequency detuning from the cooling transition.

Atom chip is a universal platform for quantum sensors, such as atomic clocks, gravimeters, gradiometers, accelerometers and gyroscopes, which are distinguished by increased accuracy that surpasses classical analogs. The use of localized atoms near the surface of an atom chip makes it possible to create compact systems that can be used on board of aircraft, satellites and other portable platforms [1].

The critical parameters of quantum sensors affecting their accuracy and convenient application are the number and temperature of cooled atoms, spatial dimensions of the atomic ensemble, and measurement time. Modern quantum sensors operate in a periodic regime, which is determined by the periodic regime of the formation of the ensemble of cold atoms: cooling of thermal atoms, their localization, additional cooling in an atomic trap, optical pump to a certain magnetic sublevel, and the interaction of the prepared atomic ensemble with a given sequence of laser (in the case of the gravimeter and gradiometer) or microwave (in the case of atomic clocks) pulses. The total measurement time depends on the operating time at each of the stages of the experimental sequence. The critical parameters are the cooling rate of thermal atoms and the formation time of the primary ensemble of cold atoms localized in the magneto-optical trap. This stage is the longest and determines the acquisition time of data measured by a quantum sensor. The reduction of the cooling time of atoms in the magneto-optical trap decreases the total number of atoms, which finally increases noise of the signal measured by the quantum sensor.

One approach to reduce the cooling time is to use pre-cooled atoms to load the trap. A possible use of pre-cooling is the loading of atoms from a pre-cooled atomic beam. This approach is widely used not only for loading atom chip, but also for loading classical 3D MOT. For this, loading from a low-velocity intense source of atoms (LVIS) is widely used [2]. One of the features of such systems is the formation of the atomic beam with a low longitudinal velocity. Unfortunately, since the residual transverse velocity exists and the time of flight from the LVIS to the atom chip is long in this approach, the diameter of the atomic beam near the chip can increases to several millimeters because the longitudinal velocity is low. This circumstance is essential when loading single-layer chips with a small localization area [3], where it becomes necessary to reduce the transverse velocities of the low-velocity beam.

One way to control the transverse velocity is to focus the atomic beam using a two-dimensional magneto-optical trap [4, 5]. It is a two-dimensional analog of the three-dimensional pulsed compression of the magneto-optical trap considered in [4], the schematic diagram of the experiment is shown in Fig. 1. The main feature of this method is that the focusing point of atoms in the beam in the longitudinal direction is independent of their transverse velocity because the atom in the field of the 2D MOT at the saturation of the atomic transition can be treated as an overdamped oscillator.

In [6] it is calculated, that the focusing region is about 250 μm. A more accurate calculation taking into account the momentum diffusion shows that the focusing region has a characteristic size of about 8 mm, which is much larger than the typical chip localization area [3] (~ 1 mm). However, the transition

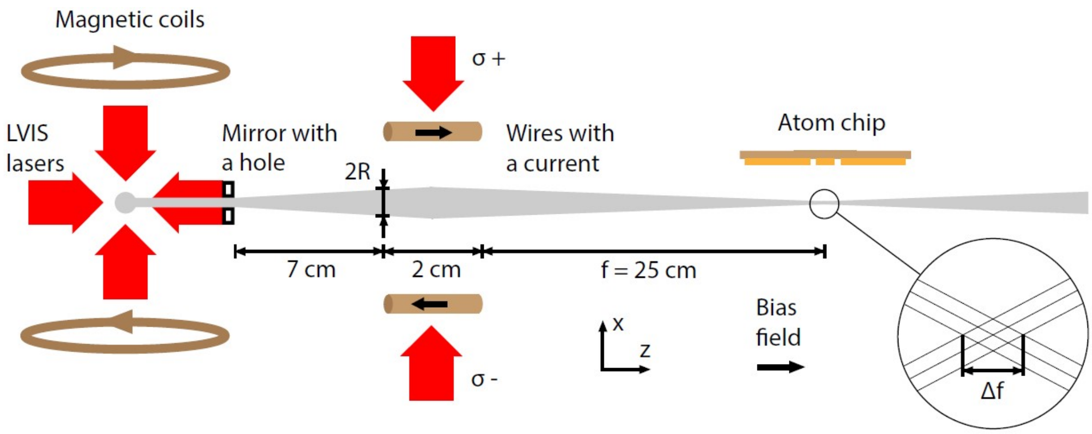

Figure 1: Scheme of focusing an atomic beam formed from LVIS into the localization region of an atom chip [6].

to the sub-Doppler cooling mechanism in a 2D MOT makes it possible to effectively reduce the momentum diffusion and narrow the focus region to 1.6 mm.

The combination of these approaches makes it possible to increase the efficiency of loading traps for cold atoms near the atomic chip. Such systems can be used to create a new generation of quantum sensors, which will be characterized by increased sensitivity.

This work was supported by the Russian Foundation for Basic Research (19-29-11004) and (23-22-00255).

References

[1] *M. Keil, O. Amit, S. Zhou, D. Groswasser, Y. Japha, and R. Folman*, Fifteen years of cold matter on the atom chip: promise, realizations, and prospects. J. Mod. Opt. **63**, 1840 (2016).

[2] *Z. T. Lu, K. L. Corwin, M. J. Renn, M. H. Anderson, E. A. Cornell, and C. E. Wieman*, Low-Velocity Intense Source of Atoms from a Magneto-optical Trap. Phys. Rev. Lett. **77**, 3331 (1996).

[3] *A. E. Afanasiev, A. S. Kalmykov, R. V. Kirtaev, A. A. Kortel, P. I. Skakunenko, D. V. Negrov, and V. I. Balykin*, Single-layer atom chip for continuous operation: Design, fabrication and performance. Opt. Laser Technol. **148**, 107698 (2022).

[4] *V. I. Balykin*, Pulsed magnetooptic compression of cold atoms. JETP Lett. **66**, 349 (1997).

[5] *P. N. Melentiev, P. A. Borisov, S. N. Rudnev, A. E. Afanasiev, and V. I. Balykin*, Focusing of an atomic beam by a two-dimensional magneto-optical trap. JETP Lett. **83**, 14 (2006).

[6] *A. E. Afanasiev, D. V. Bykova, P. I. Skakunenko and V. I. Balykin* , Focusing of an Atomic Beam for the Efficient Loading of an Atom Chip. JETP Lett. **115**, 509 (2022).

Phosphorus incorporation into silicon by PBr_3 adsorption on Si(100)

Vladimir Shevlyuga[1], **Yulia Vorontsova**[1,2*], **Tatiana Pavlova**[1]

[1] *Prokhorov General Physics Institute of the Russian Academy of Sciences, Moscow, Russia*
[2] *HSE University, Moscow, Russia*
*E-mail: `y.vorontsova@alumni.nsu.ru`

Abstract

The phosphorus incorporation into silicon with atomic precision is a key problem in the development of quantum devices based on single impurities in silicon. The PBr_3 molecule is compatible with the halogen mask on Si(100), which has been proposed as an alternative to the hydrogen mask currently in use. Here we studied the PBr_3 adsorption on Si(100) using STM and DFT. We have shown that heating of a PBr_3-dosed sample leads to phosphorus incorporation into silicon. Thus, we proved that the PBr_3 molecule can be used for P incorporation into Si(100) through the halogen mask.

Phosphine is currently used as a source of phosphorus to create all elements of an atom-based silicon quantum chip (qubits, single-electron transistors, and contacts) [1, 2]. PH_3 is compatible with a hydrogen monolayer resist, from which a mask is created by removing single hydrogen atoms in a scanning tunneling microscope (STM). An alternative to the hydrogen resist can be a halogen monolayer. The halogen monolayer can be used as a mask by removing single atoms [3]. Moreover, the halogen monolayer better protects the silicon surface from unwanted incorporation of phosphorus from a halogen-containing molecule than the hydrogen monolayer [4].

As a source of phosphorus compatible with the halogen resist, a halogen-containing molecule such as PBr_3 can be used. In this work, we study the adsorption of the PBr_3 molecule on the Si(100) surface and the subsequent incorporation of phosphorus into silicon. The experiments were carried out in an ultra-high vacuum (UHV) system with a base pressure of 5×10^{-11} Torr. The STM measurements were performed with GPI CRYO (SigmaScan Ltd.) operated at 77 K. The identification of objects after PBr_3 adsorption and the calculation of activation barriers of PBr_3 dissociation were carried out on the basis of the density functional theory (DFT).

Figure 1a shows a clean Si(100) surface before PBr_3 adsorption. After PBr_3 adsorption, various objects were observed on the surface (Fig. 1b). The atomic resolution STM image of the most frequently observed object is shown in the inset to Fig. 1b. This object occupies three adjacent Si dimers. Based on DFT calculations, we found that this object is a completely dissociated molecule. We calculated one of the possible paths for the complete dissociation of the PBr_3 molecule and found that the process should occur with a time scale of about 10 seconds at room temperature.

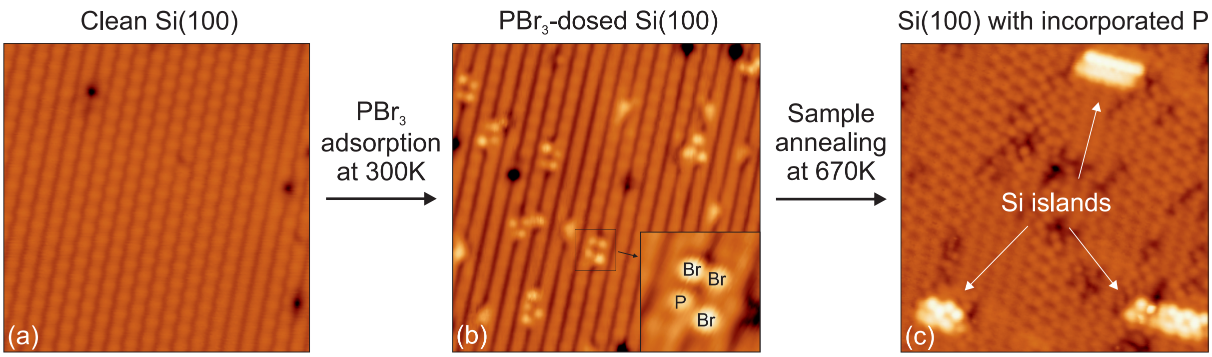

Figure 1: The STM images ($14.3\times14.3\,\mathrm{nm}^2$) of the Si(100) surface before PBr_3 adsorption (a), after PBr_3 adsorption at room temperature (b), and after sample annealing at 670 K (c). (b) Inset: the most frequently observed object on the PBr_3-dosed Si(100) surface, which is a completely dissociated PBr_3 molecule.

To incorporate phosphorus into silicon as a substitutional impurity, the sample must be heated [5]. After heating the sample with adsorbed PBr_3 to 670 K for 5 minutes, small islands appeared on the surface (Fig. 1c). We believe that the islands are formed from silicon, since the height of the islands is equal to the height of the Si(100) atomic step, and Si buckling is visible on them. Silicon ejected to the surface indicate the incorporation of phosphorus into silicon [5].

Our results demonstrate that the PBr_3 molecule can be used to insert phosphorus atoms into silicon. For incorporation of single phosphorus atoms, a halogen monolayer mask compatible with this halogen-containing precursor molecule can be used. In addition, we can conclude that the maximum window size in the mask is three Si dimers, since three dimers are required for complete dissociation of the PBr_3 molecule on the clean Si(100) surface.

This work was supported by the Russian Science Foundation under the grant No. 21-12-00299. We thank the Joint Supercomputer Center of RAS for providing the computing power.

References

[1] *Y. He, S.K. Gorman, D. Keith, L. Kranz, J.G. Keizer, M.Y. Simmons*, A two-qubit gate between phosphorus donor electrons in silicon. Nature **571**, 371 (2019).

[2] *M. Fuechsle, J. A. Miwa, S. Mahapatra, H. Ryu, S. Lee, O. Warschkow, L. Hollenberg, G. Klimeck, M. Y. Simmons*, A single-atom transistor. Nat. Nanotechnol. **7**, 242 (2012).

[3] *T. Pavlova, V. Shevlyuga, B. Andryushechkin, K. Eltsov* Dangling bonds on the Cl- and Br-terminated Si(100) surfaces. Appl. Surf. Sci. **591**, 153080 (2022).

[4] *T. V. Pavlova, K. N. Eltsov* Reactivity of the Si(100)-2×1-Cl surface with respect to PH_3, PCl_3, and BCl_3: comparison with PH_3 on Si(100)-2×1-H. J. Phys.: Condens. Matter **33**, 384001 (2021).

[5] *S.R. Schofield, N.J. Curson, M.Y. Simmons, F.J. Rue, T. Hallam, L. Oberbeck, and R.G. Clark*, Atomically Precise Placement of Single Dopants in Si. Phys. Rev. Lett. **91**, 136104 (2003).

Trapping and Laser Cooling of Yb Ions in a Multipole Trap for Future Implementation in Microwave Frequency Standard

Igor Zhuravlev[1,2,3*], **Andrey Korolkov**[1,3], **Ilia Semerikov**[1,3], **Ilia Zalivako**[1], **Alexander Borisenko**[1], **Mikhail Aksenov**[1], **Pavel Sidorov**[1], **Nikita Semenin**[1], **Vasilii Smirnov**[1,2,3], **Ksenia Khabarova**[1], **Nikolai Kolachevskiy**[1,3]

[1] *P.N.Lebedev Physics Institute of the RAS, Moscow, Russia*
[2] *Moscow Institute of Physics and Technology (National Research University), Dolgoprudny, Russia*
[3] *Russian Quantum Center, Skolkovo, Russia*
*E-mail: `zhuravlev.ia@phystech.edu`

Abstract

The use of multipule traps in ion–based frequency standards makes it possible to significantly control the frequency shifts caused by the Doppler effect. It allows to reduce the non–exclusive systematic error of the standard and increase its accuracy. In this paper we numerically calculated the density of ion cloud in a multipole trap in order to take into account the second–order Doppler shift from micro motions. With the obtained results we demonstrate the advantages of using a multipole trap in comparison with a quadrupole trap during the excitation of a clock transition. The fully built up experimental setup and laser cooled ion crystal are also presented.

Linear Paul traps are usually used to capture charged particles in experiments on quantum logic and spectroscopy. These traps with a number of electrodes $2k$ use alternating electric fields, capturing a particle of charge $+e$ and mass m in effective pseudopotential [1]

$$\Psi(r) = \frac{k^2}{4}\frac{e^2}{m\Omega^2}\frac{V_0^2}{r_0^2}\hat{r}^{2k-2}, \quad \hat{r} = \frac{r}{r_0} \tag{1}$$

near their axis, where V_0 is an amplitude of AC voltage, Ω is its angular frequency, and r_0 is an inner radius of the trap. The radial density $n(r)$ of ions in such a potential at temperature T is described by the Boltzmann distribution

$$n(r) = n(0)\exp\left\{\frac{-\Psi(r) - e\varphi_{\mathrm{sc}}(r)}{k_B T}\right\}, \tag{2}$$

where k_B is the Boltzmann constant, and the potential of space charge $\varphi_{\mathrm{sc}}(r)$ obeys the Poisson's equation

$$\nabla^2\varphi_{\mathrm{sc}}(r) = -en(r)/\varepsilon_0. \tag{3}$$

Thus, we can obtain a non–linear ODE on radial density $n(r)$ of the ion cloud [2]

$$n''(r) + \frac{n'(r)}{r} - \frac{n'(r)^2}{n(r)} - \frac{n(r)^2}{n_0\lambda_D} = -k^2(k-1)^2\frac{n(r)}{4\lambda_D^2}\hat{r}^{2k-4}, \tag{4}$$

where $n_0 = 2\varepsilon_0 m\Omega^2/e^2$ is a saturation density or a pseudo charge density, and $\lambda_D^2 = k_B T/(2m\Omega^2)$ is the Debye length. We solved the Boltzmann equation for the density profile numerically and compared results for quadrupole and multipole traps. Assuming Yb ions at 700 K temperature we have also plotted the normalized second order Doppler shift from the two dimensional micromotion vs radial position (see Fig. 1). This is defined as follows

$$\frac{-\left\langle\dfrac{v^2}{2c^2}\right\rangle}{-\dfrac{k_B T}{mc^2}} = \frac{k^2}{8}\frac{m\Omega^2 r_0^2}{k_B T}\hat{r}^{2k-2} \equiv F_d^k. \tag{5}$$

Finally, we can compute the total second order Doppler shift for the trapped ions with density profile $n(r)$

$$\frac{\Delta\nu}{\nu} = -\frac{3k_B T}{2mc^2}\left(1 + \frac{2}{3}N_d^k\right), \quad \text{where } N_d^k = \frac{\int n(r) r F_d^k(r) dr}{\int n(r) r dr}. \tag{6}$$

We evaluate this expression for both ion traps used in our experiment. As it is shown in Fig. 1, the changes in ion number in 16–pole trap influence the total 2^{nd} order Doppler shift more that 17 times less than the same change in the quadrupole trap at the same temperature.

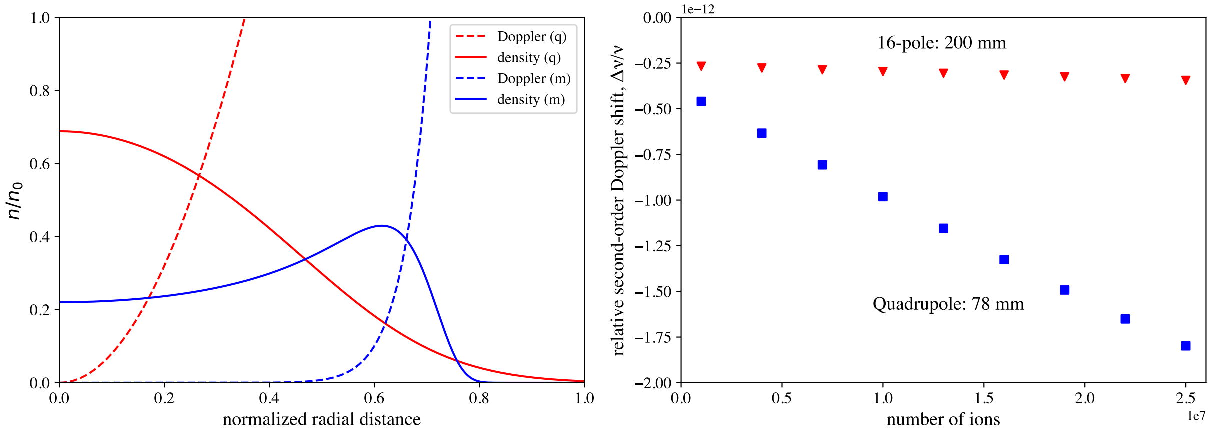

Figure 1: **left:** Normalized ion density inside a quadrupole and 16–pole traps at 700 K temperature. **right:** Second order Doppler shift dependence on number of ions inside two traps.

In our experiment we use a two–section linear trap which combines 78–mm quadrupole and 200–mm 16–pole trap (see Fig. 2). Due to the dense arrangement of electrodes in multipole trap, there is no optical access to the ion cloud there. Since that the quadrupole trap is used to prepare and detect the quantum state while the multipole section is applied during the excitation of clock transition ($^2S_{1/2}|F=0\rangle \rightarrow^2 S_{1/2}|F=1\rangle$) via external microwave source. The ion transition between the sections is carried out using the end cap electrodes and takes about 300 µs for quadrupole→multipole case and about 35 ms for multipole→quadrupole case due to the length of multipole section.

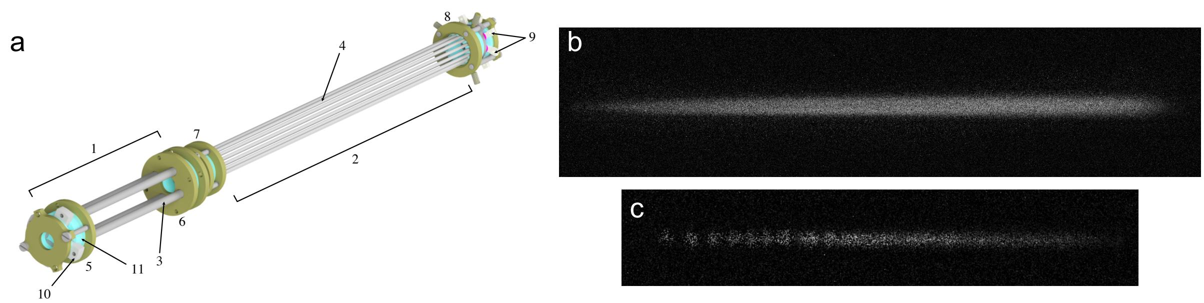

Figure 2: Combined linear trap (**a**). Trapped and laser cooled ion cloud (**b**) and ion chain of approximately 25 ions (**c**) in quadrupole section.

The first stage of preparation of the trapped Yb–ion ensemble is Doppler laser cooling which occurs on $^2S_{1/2} \leftrightarrow^2 P_{1/2}$ transition near the wavelength of 369 nm with a 935–nm repumping laser. It allows to operate with ion crystals (see Fig. 2) at a low temperature, reducing the linear Doppler shift. Thus, the whole period of the operation of frequency standard consists of laser cooling, optical pumping of the ground state, excitation of the clock transition, and state detection.

References

[1] *Dieter Gerlich*, Inhomogeneous RF Fields: A Versatile Tool for the Study of Processes with Slow Ions (1992).

[2] *Prestage, J.D., Tjoelker, R.L. and Maleki, L.*, Higher pole linear traps for atomic clock applications. (Cat. No. 99CH36313) (Vol. 1, pp. 121–124). IEEE. 1999, April.

Two-qubit quantum photonic processor manufactured by femtosecond laser writing

Ilya Kondratyev[1*], **Nikolay Skryabin**[1], **Ivan Dyakonov**[1], **Oksana Borzenkova**[2], **Sergey Kulik**[1,3] **and Stanislav Straupe**[1,2] ,

[1] *Quantum Technology Centre and Faculty of Physics, M.V. Lomonosov Moscow State University, 1 Leninskie Gory Street, Moscow 119991, Russian Federation*

[2] *Russian Quantum Center, Russia, Moscow, 121205, Bol'shoy bul'var 30 building 1*

[3] *Laboratory of quantum engineering of light, South Ural State University (SUSU), Russia, Chelyabinsk, 454080, Prospekt Lenina 76*

*E-mail: `iv.kondratjev@physics.msu.ru`

Abstract

In this work we have manufactured, investigated and tested the two-qubit integrated photonic processor in fused silica glass. Fidelity of single qubit operations was no less than 97%. Quantum process tomography of the inner two-qubit CNOT gate was performed and showed 94.4% fidelity of its' operation. We showed the potential of practical use of the manufactored processor by launching a variational quantum eigensolver algorithm to estimate the bound energy curve of the hydrogen H_2 molecule.

Programmable integrated optical circuits believed to be a promising platform for scalable quantum computation in future [1]. One of the technologies for manufacturing such integrated optical circuits is femtosecond laser writing of waveguiding structures in optically transparent samples, which is a simple, fast and not expensive technology for prototyping low and medium scale integrated photonic devices, which can be usefully exploited [2].

In this work we have fabricated reconfigurable six mode integrated optical chip in fused silica glass by femrosecond laser writing, which in couple with a pair of single photons at the input and a single photon detectors at the output serving as a two qubit photonic quiantum processor. This work is based on a recently uploaded article [3], which is currently under the reviewing process.

The structure of the quantum photonic processor is demonstrated in Fig 1 and consisted of two pairs of single qubit gates and one two qubit CNOT gate in between. Each qubit was dual rail encoded with a single photon. Thermo-optical switching was used for the reconfiguration of the processor.

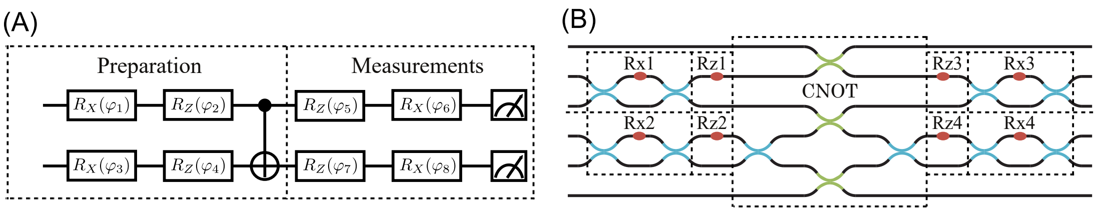

Figure 1: (A) Quantum circuit of the two qubit processor, which is consisted o eight single qubit rotation gates and one two qubit CNOT gate. (B) Schematic of a waveguide structure of the integrated interferometer realizing the photon encoded quantum processor. Black lines represent the optical single mode waveguides. Balanced 50:50 directional couplers are shown with blue colour and 33:66 directional couplers are shown with green. Red circles stand for the thermo-optical heaters used for the chips' reconfiguration.

Spontaneous parametric down conversion (SPDC) source with a PPKTP crystal was used for the generation of two indistinguishable single photons, which were injected into the chip through optical single mode fiber arrays. An avalanche photo diode detectors (Laser Components COUNT modules) were used for output photons counting.

Thermo-optical heaters were calibrated allowing for realising an arbitrary single qubit operations by each of four Mach-Zander interferometers. All single qubit gate operations were estimated to be not less

Table 1: Mean fidelities and standard deviations for each single qubit gate.

Gate	R_{x1}	R_{z1}	R_{x2}	R_{z2}	R_{x3}	R_{z3}	R_{x4}	R_{z4}
Mean	0.995	0.993	0.997	0.993	0.994	0.997	0.988	0.986
Std	0.003	0.003	0.001	0.005	0.003	0.002	0.007	0.008

than 97%. Mean fidelities and their standard deviations for each single qubit gate are presented in Table 1.

A quantum process tomography of the inner two qubit CNOT gate was performed resulting in 94.4% gate fidelity. The fidelity value was estimated according to:

$$F(U_e, U_t) = \frac{|Tr(U_e^{\dagger} U_t)|^2}{Tr(U_e^{\dagger} U_e) Tr(U_t^{\dagger} U_t)}, \tag{1}$$

where U_e - experimentally obtained χ-matrix and U_t - theoretical. Experimentally obtained CNOT process χ-matrix is shown in Fig 2 (A).

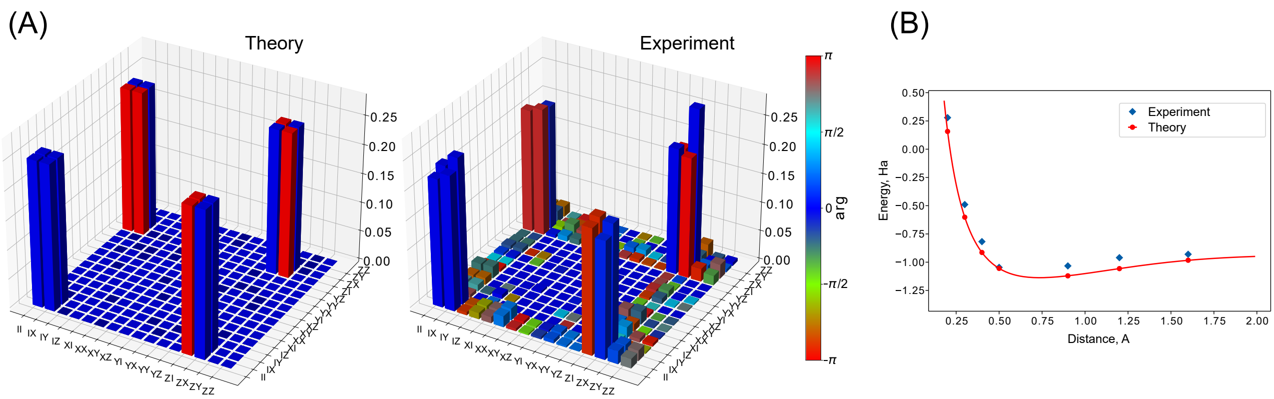

Figure 2: (A) Experimentally obtained CNOT process χ-matrix (on the right) and in theory (on the left). (B) Measured on a two qubit photonic quantum processor bound energy curve of the hydrogen molecule H_2.

For demonstration of the potential practical usability of our processor we conducted a variational quantum eigensolver algorithm for bound energy estimation of the hydrogen molecule H_2. Measured bound curve is depicted in Fig 2 (B).

We believe this work will prove the potential feasibility of integrated optical chips manufactured by femtosecond laser writing in optically transparent samples for quantum processing problems solving.

References

[1] *G. Moody, V. J. Blumenthal, et al*, 2022 Roadmap on integrated quantum photonics. Journal of Physics: Photonics, **4**(1), 012501 (2022).

[2] *Li, Lingqi and Kong, Weijin and Chen, Feng*, Femtosecond laser-inscribed optical waveguides in dielectric crystals: a concise review and recent advances. Society of Photo-Optical Instrumentation Engineers, **4**(2), 024002 (2022).

[3] *N.N. Skryabin, I.V. Kobdratyev, I.V. Dyakonov, O.V. Borzenkova, S.P. Kulik and S.S. Straupe*, Two-qubit quantum photonic processor manufactured by femtosecond laser writing. arXiv preprint arXiv:2212.05931, (2022).

Phonon influence on shot noise in resonant tunneling

Igor Krainov, Alexander Dmitriev, Nikita Averkiev

Ioffe Institute, St. Petersburg, 194021, Russia
*E-mail: igor.kraynov@mail.ru

Abstract

Most studies to date have found, by means of various approximate or phenomenological methods, that the Fano factor or the shot noise in a double barrier structure are insensitive to dephasing caused by inelastic scattering. In this work, the authors explore the status of this statement by deriving a general Landauer-Büttiker-type formula that expresses the current noise and the Fano factor in a one-dimensional conductor through inelastic scattering amplitudes.

One of the key factors affecting the scaling of quantum logic devices is the presence of dephasing sources. The study of dephasing processes helps to better understand it and, as a result, the possibilities for their optimization. In particular, it is important to study their influence on quantum coherent processes. As is known, the violation of the phase coherence of electron waves due to inelastic scattering processes plays a key role in low-dimensional transport: as the intensity of these collisions decreases, the system passes from the classical mode of transport to the quantum mode, when interference effects become dominant. One of the simplest and most important effects for practical applications is resonant tunneling through a quantum dot with tunneling contacts, which exhibits narrow peaks in conductivity when the Fermi level crosses the level of quantum confinement of states in QDs and at low temperatures.

In this work [1] the influence of inelastic scattering processes on the Fano factor was studied, a value characterizing current noise in one-dimensional transport. Current noise consists of two contributions: thermal, proportional to temperature, and shot, observed in a non-linear mode, when the applied voltage exceeds the temperature. For a one-dimensional two-barrier system with resonant tunneling, the Fano factor in the nonlinear regime is: $F = (\Gamma_L^2 + \Gamma_R^2)/(\Gamma_L + \Gamma_R)^2$, where Γ_L and Γ_R are the barrier strengths. Until now, there is no exact answer to the question of the effect of the dephasing rate on the Fano factor of a two-barrier structure. This issue has been widely discussed in the literature and investigated by various methods, for example, using kinetic equations (i.e., completely incoherent transport), Langevin forces, and lead to the above expression. In the case of the picture of quantum transport, and calculation using the quantum kinetic equation or non-equilibrium Green's functions, the same result is obtained. Also, there are a number of works demonstrating deviations from this result. However, in all works, certain approximations and simplifications were used. For an unambiguous answer to this question, it is necessary to accurately take into account inelastic processes in the quantum interference pattern of electron transport.

To answer this question, a general expression was obtained for the current noise in a one-dimensional conductor with an inelastic scatterer in terms of exact inelastic scattering amplitudes, which is a new result and allows you to accurately analyze the effect of phase failure. As a next step, accurate scattering amplitudes were obtained for a two-barrier structure with a given random non-stationary potential acting between the barriers. As a random potential, the case of phonons as a source of phase failure was analyzed in detail. For one-dimensional phonons, random additions to the electron wave function phase are diffusion like $\langle \varphi_f^2 \rangle \sim t/\tau_\varphi$, while for two-dimensional or three-dimensional phonons they lead to non-diffusion type phase dynamics $\langle \varphi_f^2 \rangle \sim \ln(t/\tau_\varphi)$. For these types of phase failures, the transmission coefficients were calculated. For the diffusion type of phase failure, it is described by one energy scale $\Gamma_\Sigma + h/\tau_\varphi$ and has a standard Lorentzian profile. Whereas the logarithmic type of dephasing leads to an unusual transmission coefficient profile with two characteristic energy scales determined by the barrier transparencies and the phonon correlation time. The Fano factor was calculated for these types of dephasing. This study made it possible to answer the question about the effect of wave phase dephasing on the Fano factor.

This work was supported by Rosatom in the framework of the Roadmap for Quantum Computing (Contract No. 868-1.3-15/15-2021 dated 5 October 2021 and Contract No. R2152 dated 19 November 2021).

References

[1] *I.V. Krainov, A.P. Dmitriev and N.S. Averkiev*, Shot noise in resonant tunneling: Role of inelastic scattering. Phys. Rev. B **106**, 245421 (2022).

Multi-qubit gate implementation on qudit-based trapped-ion processors

A.S. Nikolaeva[1,2*], E.O. Kiktenko[1,3], A.K. Fedorov[1,3]

[1] *Russian Quantum Center, Skolkovo, Moscow 121205, Russia*
[2] *Moscow Institute of Physics and Technology, Dolgoprudny, Moscow Region 141700, Russia*
[3] *National University of Science and Technology "MISIS", Moscow 119049, Russia*
*E-mail: anastasiia.nikolaeva@gmail.com

Abstract

In this work, we propose multiqubit gate decomposition techniques for qudit-based trapped-ion processors. We develop N-qubit Toffoli gate decomposition on qutrits with $2N-3$ $\mathsf{MS}(\pi/2)$ gates. We also show how to decompose generalized N-qubit controlled phase gate with MS gate on ququarts, when the space of ququart is considered as a space of two qubits.

Recent advances in the development of quantum processors [1, 2] based on qudits, d-level quantum systems, make it essential to examine possible ways to use increased computational spaces. It was shown that a substantial improvement in the realization of qubit algorithms on qudit processors can be achieved using qudits for simplifying multi-qubit gate decompositions. The use of qudits, in particular, allows one to reduce the number of two-particle interactions in such decompositions [3, 4]. However, most of the proposed qudit-based decompositions use controlled phase CZ as a basic two-particle operation. Despite its popularity, the CZ gate is not included in the native set of gates for trapped-ion processors. Typically, the Mølmer–Sørensen (MS) gate is a native two-qudit gate for the trapped-ion based qudit processors. Therefore, additional research is needed to find efficient multi-qubit gate decompositions with qudit MS gates as a basic gate.

Native gate set for two qudit-based trapped-ion processors, which were presented last year [1, 2], is given by single-qudit rotations

$$R_{\varphi}^{\alpha,\beta}(\theta) = \exp(-\imath\theta\sigma_{\varphi}^{\alpha,\beta}/2) \tag{1}$$

where $\varphi \in \{x, y, z\}$, $\sigma_{\varphi}^{\alpha,\beta}$ – extended Pauli matrices, and α, β indicate transition in the qudit, and a two-qudit Mølmer–Sørensen gate:

$$\mathsf{MS}(\chi) = \exp\left(-\imath[\sigma_x^{0,1} \otimes \sigma_x^{0,1}]\chi\right). \tag{2}$$

The main feature of this gate set is that the two-particle gate in the extended qudit space applies additional phases on higher levels compared to the qudit version of the CZ gate, which applies phase factor -1 only to the two-qudit state $|11\rangle$. For this reason, earlier proposed qudit-based decompositions of multiqubit gates, which relies on qudit CZ gate, cannot be directly used on the trapped-ion qudit processors.

In this work, we investigate the problem of multi-qubit gate construction with a qudit-based (MS) gate. The N-qubit generalized Toffoli gate $\mathsf{C}^{N-1}\mathsf{X}$ and generalized controlled-phase gate $\mathsf{C}^{N-1}\mathsf{Z}$ gate are used as examples of a multi-qubit gates. These gates are frequently used in quantum algorithms as basic multi-qubit gates, for example, they are contained in both parts of Grover's algorithm: the oracle and diffusion operator.

Although trapped-ion platform provides us up to 7 levels in each qudit [1, 2], we focus our attention on qutrits ($d = 3$) and ququarts ($d = 4$). We have developed a separate decomposition technique for each dimension of qudit. Following earlier proposed approach to consider qutrit's space as a space of qubit with ancillary level [4], we show how generalized Toffoli gate can be constructed with $2N-3$ two-qutrit $\mathsf{MS}(\pi/2)$ gates (see Fig. 1). We also analyze the ququart case, where ququart's space is considered as the space of two qubits. In this case, CZ gate between two qubits in a singe ququart is implemented as a sequence of singe-qudit $R_{\varphi}^{\alpha,\beta}(\theta)$ gates. To examine the realization of two-qubit gates between qubits located in different qudits, we discuss the action of extended in ququart space MSgate. Then we demonstrate how CZ gate between two qubits located in different ququarts can be realized with $\mathsf{MS}(\pi)$ gate. On the basis of single-qubit operations within the single qudit and two-qubit CZ gate between arbitrary pair of qubits located in qudits, multi-qubit gate decomposition can be constructed. One of the possible approach is to use standard qubit decomposition of multi-qubit gates can be used as

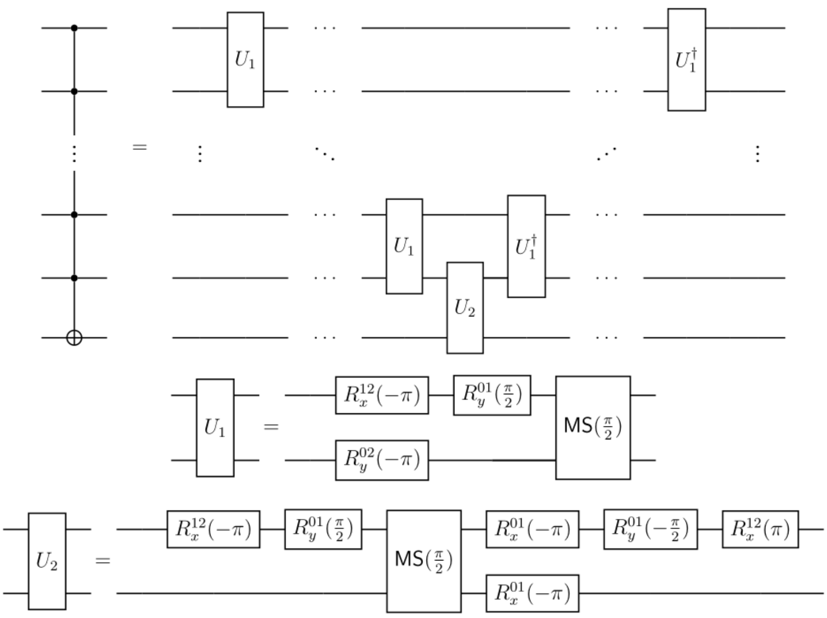

Figure 1: Generalized Toffoli gate decomposition on qutrits with $2N-3$ two-qutrit $\mathsf{MS}(\pi/2)$ gates.

a template and to match qubit gates from them with qudit ones [5]. We expect these techniques to have a strong potential to improve the transpilation process of qubit algorithms to native qudit sets of gates on rapidly developing trapped-ion-based qudit processors.

The research is supported by RSF grant No. 19-71-10091.

References

[1] M. A. Aksenov, I. V. Zalivako, I. A. Semerikov, et al. Realizing quantum gates with optically-addressable ^{171} Yb $^{+}$ ion qudits. arXiv preprint arXiv:2210.09121. (2022).

[2] *M. Ringbauer, M. Meth, L. Postler, et al.*, A universal qudit quantum processor with trapped ions. Nat. Phys. **18**, 1053–1057 (2022).

[3] *A.S. Nikolaeva, E.O. Kiktenko, and A.K. Fedorov*, Decomposing the generalized Toffoli gate with qutrits. Physical Review A **105**, 032621 (2022).

[4] *E.O. Kiktenko, A.S. Nikolaeva, P. Xu, G.V. Shlyapnikov, and A.K. Fedorov*, Scalable quantum computing with qudits on a graph. Physical Review A **101**, 022304 (2020).

[5] *A.S. Nikolaeva, E.O. Kiktenko, and A.K. Fedorov*, Efficient realization of quantum algorithms with qudits. arXiv preprint arXiv:2111.04384. (2022).

Parallel coupling of trapped ions in multiple individual wells

A. Podlesnyy[1*], Y Suleimen[1], L. A. Akopyan[1], O. Lakhmanskaya[1], K. Lakhmanskiy[1]

[1]*Russian Quantum Center, Skolkovo, Moscow 143025, Russia*
*E-mail: a.podlesnyy@rqc.ru

Abstract

In this paper we offer a new surface trap design capable of coupling the ion motion in the selected wells among ten by adjusting the DC-voltages on a set of electrodes. We demonstrate and characterize a variety of phonon mode spectra for different voltage sets for 10 ion-architecture for two types of ions Ca and Be. We found that it is possible to unite the ions into segments with unique phonon mode frequencies to perform parallel MS-gate operations. We also model the fidelity of the MS-gate operation for a segment comprise of two ions accounting the two main contributions to the gate infidelity: the limited frequency difference between phonon frequencies of the segments and the finite drift of the phonon frequencies expected in experiment. Additionally, we investigate how the number of ions per individual trap and an anharmonic potential terms affect the coupling between the two wells.

Trapped ions are one of the leading technology platforms for large-scale Quantum Computing (QC). However, practical realizations of QC require the ability to increase the number of simultaneously trapped ions while maintaining the ability to control and measure them individually with high fidelity. For single linear arrays of ions the speed and performance of two-qubit gates generally decreases as the total number of ions grows. A promising approach around these issues is to break a single long ion chain into segments. Each such a segment or module can trap a restricted number of ions to maintain high fidelity and high-speed operations. The challenge, then, becomes how to move quantum information between the modules. The coupling between the ions in separated segments can be achieved in different ways: through transport, through effective spin-spin interactions, shared electrically floating electrode or controlled orientation of the secular modes. Here we focus on the alternative method: the exchange of the phonons between separate wells. Proof-of-principle investigations demonstrated its efficiency for two trapping regions. In this paper [1] we offer a new surface trap design capable of coupling the ion motion in the selected wells among ten by adjusting the DC-voltages on a set of electrodes (see Fig. 1).

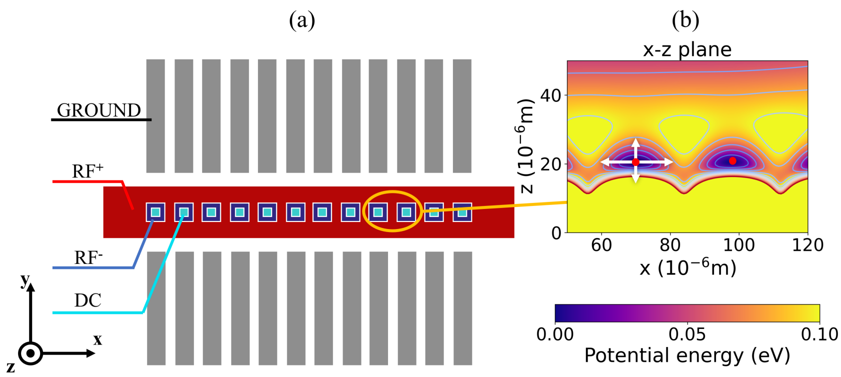

Figure 1: (a) A surface ion trap geometry, used for simulations in the paper. The trap forms 12 distinct trapping potential wells. Ion confinement with predetermined height is achieved by the single red RF^+ electrode and 12 dark-blue RF electrodes with π phase delay. 12 light-blue DC electrodes in the middle of squares are utilized for secular frequency optimization. The side DC electrodes, depicted in gray, are essential for stray field compensation. (b) Potential distribution above two individual traps. This design has a trap depth of 60-100 meV in the authorized DC voltage range. The principal axes of oscillation are illustrated by white arrows.

We account the possible issues related to anomalous heating rate typical for such traps and determine the optimum range of voltages and frequencies to negotiate this effect. Namely, we demonstrate and characterize a variety of phonon mode spectra for different voltage sets for 10 ion-architecture for two types of ions: Ca and Be. We found that it is possible to unite the ions into segments with unique phonon mode frequencies to perform parallel MS-gate operations (see Fig. 2c-d). We also model the fidelity of the MS-gate operation for a segment comprised of two ions accounting the two main contributions to the gate infidelity: the limited frequency difference between phonon frequencies of the segments and the finite drift of the phonon frequencies expected in experiment (see Fig. 2a-b). Additionally, we investigate how the number of ions per individual trap and an anharmonic potential terms affect the coupling between the two wells.

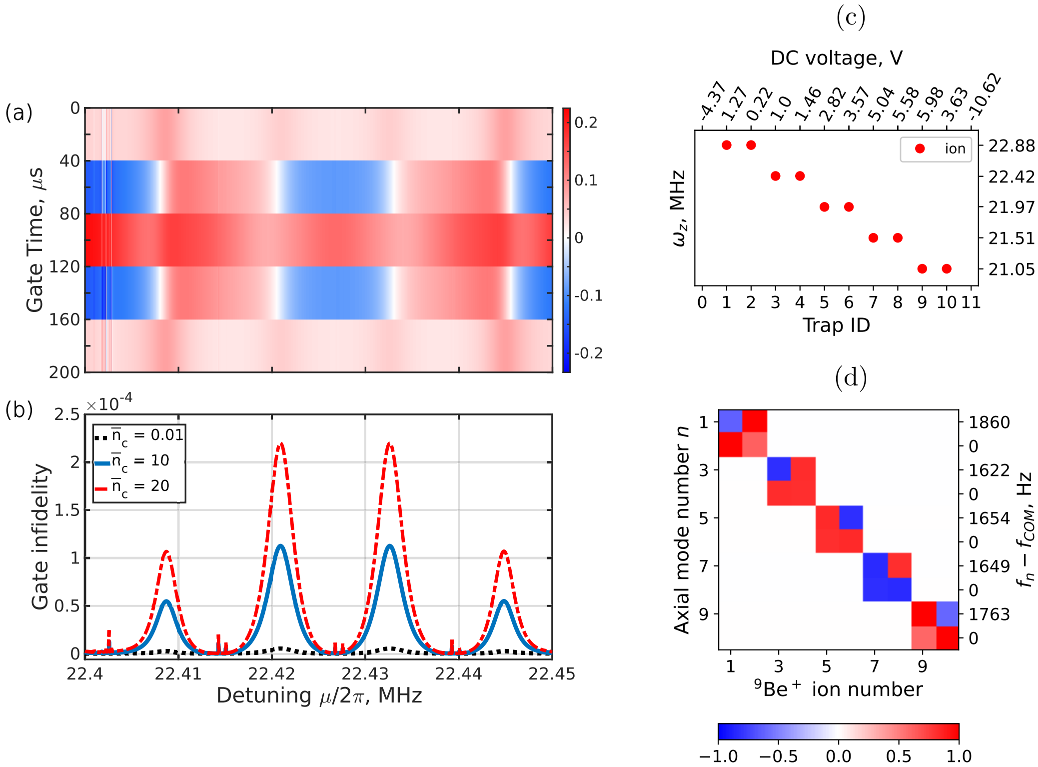

Figure 2: (a) In-time segmented Rabi frequency in MHz for two neighboring $^9Be^+$ ions, providing the highest fidelity of an MS-gate. (b) MS-gate infidelity over detuning μ for two neighboring $^9Be^+$ ions for different initial average normal mode occupations. The initial average occupation for ion pair center-of-mass mode is specified in the legend. The drift rates for all the modes are taken as 1 MHz/min. Rabi frequency instabilities coincide with gate infidelity local maxima. (c) A secular frequency spectrum of single ions depending on the trap ID. The top x axis shows required DC voltages on the central electrodes. The *0* and *11* traps are used as endcap voltages to decrease the required voltage in trapping sites. (d) A normal mode interaction matrix of $^9Be^+$ ion crystal in the presented voltage set configuration. The right y axis represents the difference between COM modes (0) and stretch mode of each ion pair. The mean frequency separation $\Delta f = 1.7$ kHz.

References

[1] *A. Podlesnyy, Y Suleimen, L. A. Akopyan, O. Lakhmanskaya and K. Lakhmanskiy*, Parallel coupling of trapped ions in multiple individual wells. arXiv:2211.07121, (2022).

Demultiplexed Single-Photon Source with a Quantum Dot Coupled to Microresonator

Maxim Rakhlin[1*], **Aidar Galimov**[1], **Ivan Dyakonov**[2], **Nikolay Skryabin**[2], **Grigorii Klimko**[1], **Marina Kulagina**[1], **Yurii Zadiranov**[1], **Konstantin Taratorin**[2], **Andrey Skalkin**[2], **Stanislav Straupe**[2,3], **Sergey Kulik**[2,4], **Alexey Toropov**[1]

[1] *Ioffe Institute, St. Petersburg, 194021, Russia*
[2] *Quantum Technology Centre, M. V. Lomonosov Moscow State University, Moscow, 119991, Russia*
[3] *Russian Quantum Center, Skolkovo, Moscow, 143025, Russia*
[4] *South Ural State University (National Research University), Chelyabinsk, 454080, Russia*
*E-mail: maximrakhlin@mail.ru

Abstract

The characteristics of a single-photon emitter based on a semiconductor quantum dot, such as their indistinguishability and brightness, depend on the stability of the recombination channel, which can switch spontaneously between exciton and trion. We show that dominant recombination through neutral exciton states can be achieved by careful control of the doping profile near an epitaxial InAs/GaAs quantum dot placed in a columnar microcavity with distributed Bragg reflectors. The achieved brightness made it possible to implement spatio-temporal demultiplexing of photons in six independent spatial modes with an in-fiber generation frequency of more than 0.1 Hz.

An ideal single-photon source is a device that delivers indistinguishable light wave packets "on demand", with each wave packet containing exactly one photon in a pure quantum state. Self-assembled semiconductor quantum dots (QDs) grown by the epitaxial method are the most promising candidate for creating an ideal single-photon source due to unique properties, such as a small spectral width of the emission line, short radiative decay time, and high quantum efficiency. Nevertheless, the fabrication of efficient single-photon sources based on QDs is not an easy task, since it requires the simultaneous fulfillment of several stringent requirements. One of the problems is the often occurring phenomenon of QD overcharging due to charge fluctuations in its environment, that leads to "blinking" and a decrease in brightness. Currently, two main methods are used to control the charge state of QDs: the implementation of the Coulomb blockade in a specially designed tunnel structure [1] and the control of the efficiency of tunneling from QDs of photoexcited carriers of the same sign in an asymmetric p-i-n heterostructure [2]. Both approaches require a careful design of the heterostructure, the implementation of complex epitaxial growth methods, and the realization of precision electrical control during source operation.

In this work, we have shown the possibility of stabilizing a given charge state of a QD by controlling the doping profile in the active region of an emitting microcavity structure with a single QD. For this purpose, self-assembled InAs/GaAs QDs placed in a columnar microcavity with distributed Bragg reflectors were grown by molecular beam epitaxy. Residual impurities in the growth chamber determine p-type background doping, as a result of which most QDs contain a resident hole and form positively charged trions upon absorption of a photon. For photoexcitation of neutrally charged excitons, background doping was compensated by introducing an n-type layer of the required thickness. Optimization of the doping profile made it possible to significantly reduce the QD "blinking" and achieve a quantum efficiency of QD excitation of more than 97% with a quality factor of the fabricated microcavity ~ 8100 and an efficiency of radiation extraction of 82%. The Hong-Ou-Mandel experiments carried out in the fabricated device demonstrate the degree of indistinguishability of 91% of successively emitted single photons within 242 ns at an efficiency of 10% inside a single-mode optical fiber. The achieved brightness made it possible to implement spatio-temporal demultiplexing of photons in six independent spatial modes (Fig. 1) with an in-fiber generation rate of more than 0.1 Hz [3]. The obtained results show the applicability of the developed heterostructures with QDs as efficient sources of photons for the implementation of a prototype photonic quantum computer based on linear optics [4].

This work was supported by Rosatom in the framework of the Roadmap for Quantum Computing (Contract No. 868-1.3-15/15-2021 dated 5 October 2021 and Contract No. R2152 dated 19 November 2021).

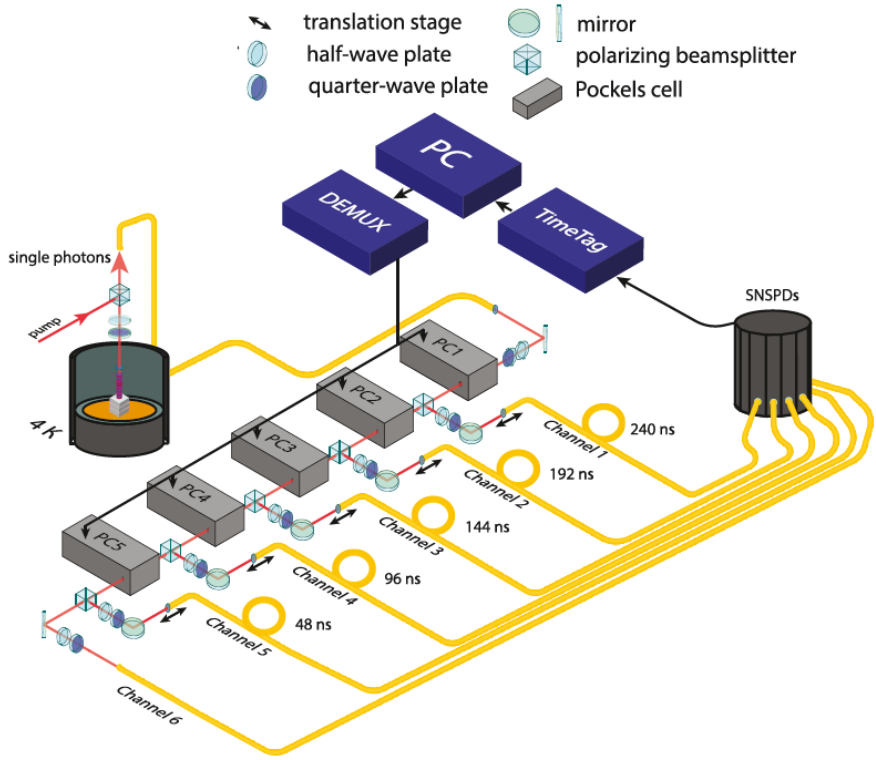

Figure 1: Optical layout of the experimental setup.

References

[1] *A. Högele, S. Seidl, M. Kroner, K. Karrai, R.J. Warburton, B.D. Gerardot, and P.M. Petroff*, Voltage-Controlled Optics of a Quantum Dot. Phys. Rev. Lett. **93**, 217401 (2004).

[2] *P. Hilaire, C. Millet, J.C. Loredo, C. Antón, A. Harouri, A. Lemaitre, I. Sagnes, N. Somaschi, O. Krebs, P. Senellart, and L. Lanco*, Deterministic assembly of a charged-quantum-dot–micropillar cavity device. Phys. Rev. B **102**, 195402 (2020).

[3] *M.V.Rakhlin, A.I. Galimov, I.V. Dyakonov, N.N. Skryabin, G.V. Klimko, M.M. Kulagina, Yu.M. Zadiranov, S.V.Sorokin, I.V.Sedova, Yu.A. Guseva, D.S.Berezina, Yu.M. Serov, N.A.Maleev, A.G.Kuzmenkov, S.I.Troshkov, K.V.Taratorin, A.K. Skalkin, S.S. Straupe, S.P.Kulik, T.V. Shubina, and A.A. Toropov*, Demultiplexed Single-Photon Source with a Quantum Dot Coupled to Microresonator. J. Lumines. **253**, 119496 (2023).

[4] *P. Kok, W.J. Munro, K. Nemoto, T.C. Ralph, J. P. Dowling, and G.J. Milburn*, Linear optical quantum computing with photonic qubits. Rev. Mod. Phys. **79**, 135 (2007).

Optimization of bipolar pulse sequences for the implementation of quantum operations using the AlphaZero algorithm

M. Sergeev[1*], **M. Bastrakova** [1,2], **V. Vozhakov**[1,3], **I. Soloviev**[1−3]

[1] *Faculty of Physics, Lobachevsky State University of Nizhny Novgorod, Nizhny Novgorod, Russia*
[2] *Russian Quantum Center, Moscow, Russia*
[3] *Skobeltsyn Institute of Nuclear Physics of Lomonosov Moscow State University, Moscow, Russia*
*E-mail: `mas_135@mail.ru`

Abstract

The possibility of implementing high-precision quantum logical operations in a superconducting qubit by state-controlling bipolar sequences of picosecond one-quantum flux pulses is shown. The perspective of improving the methods for finding these sequences by using one of the latest machine learning algorithms with reinforcement AlphaZero is being studied.

One of many possible variants for control protocols implementation for a transmon [1] (a superconducting charge qubit of a special type) is the control scheme using long sequences of control pulses with a wide spectrum - short (duration $\sim ps$) unipolar pulses generated in rapid single flux quantum quantum logic circuits. This method has proven itself in controlling main single-qubit operations [2, 3], when, using a modified sequence of unipolar pulses SCALLOP [3] it was possible to demonstrate the implementation of operations at times of $\sim$ 20 ns with the same fidelity as in Rabi microwave technique[4].

This paper presents a modification of such a control scheme, which includes the ability to use pulses of different polarity, allowing to speed up operations up to 6 ns. However, the question arises of selecting a control signal for a qubit with given parameters. For this, possible approaches to solving the optimization problem of qubit control were considered. It is known that the vast majority of algorithms for optimizing quantum dynamics are based on heuristic or purely stochastic approaches (for example, the coordinate descent method or genetic algorithms). For such algorithms, a significant limitation is the strong dependence of the final accuracy on the initial assumptions (hyperparameters), as well as the need to completely re-apply the algorithm even with a small change in the system parameters. In turn, machine learning using neural networks and reinforcement learning algorithms, one of which is AlphaZero [5], makes it possible to achieve high quality of results and, at the same time, has the ability to achieve such results when the system parameters change, even without requiring complete retraining.

After a long period of initial training using the AlphaZero algorithm, families of pulse sequences for the quantum operation $Y_{\pi/2}$ were obtained, taking into account the criterion for minimizing leakage into the overlying states outside the computational qubit basis. We used a set of input parameters that were taken from experimental work, for example, a qubit frequency of 3-7 GHz, a nonlinearity of 200-400 MHz.

In addition, the efficiency of using machine learning was shown in comparison with algorithms that do not imply a neural network and bipolar SFQ pulse system, such as microwave Rabi-technique. In particular, the visualization of the operation $Y_{\pi/2}$ on state probabilities evolution graph and on the Bloch sphere (which are displayed simultaneously at fig.1) makes it possible to clearly demonstrate the advantage of the AlphaZero algorithm in terms of reduced duration of the operation with minimal quality loss $< 10^{-3}$ (leakage to overlying states).

At fig. 1, on the Bloch sphere, one can clearly see the difference in the evolution of the states vaector. For a bipolar sequence, the red color on the sphere shows the evolution of the vector when exposed to SFQ pulses of positive amplitude, and blue color - for the negative amplitude respectively. Free precession between the SFQ pulses is marked in green.

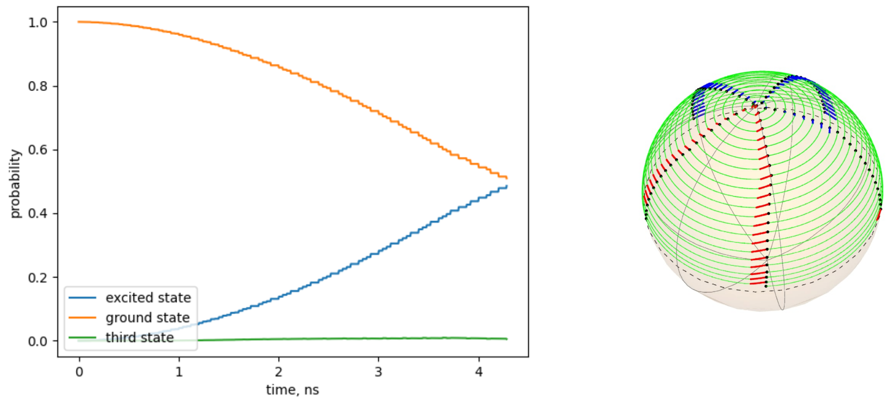

(a) Neural Network

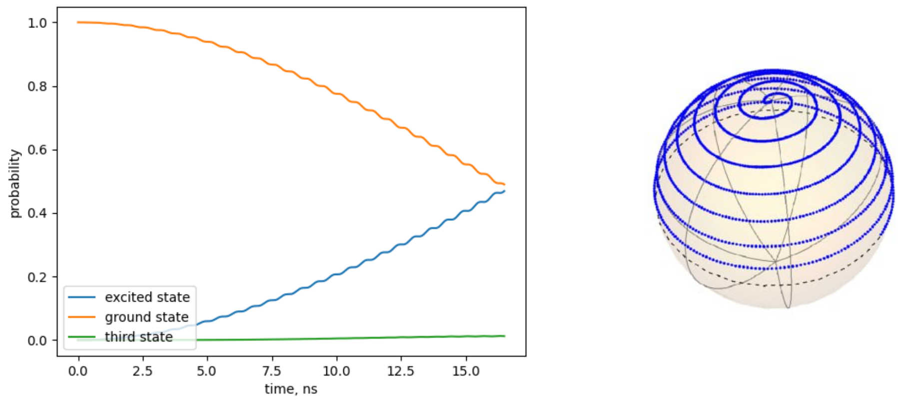

(b) Rabi technique

Figure 1: States propabilities evolution graph (on the left) and of Bloch sphere visualization (on the right) of $Y_{\pi/2}$ process: (a) for sequences generated by neural network; (b) using Rabi microwave technique.

The results of the work show the possibility of accelerating operations with transmons due to the use of voltage-inverted single flux quantum pulses in control sequences. Using the AlphaZero machine learning algorithm makes it possible to obtain the required sequence of pulses to perform a given quantum operation and for any set of qubit input parameters (frequency, nonlinearity, oscillator clock frequency, amplitude) with minimal leakage to high-lying states.

This work was supported by the Russian Science Foundation grant No. 22-72-10075.

References

[1] *P. Krantz, M. Kjaergaard, F. Yan, T. P. Orlando, S. Gustavsson, W. D. Oliver*, A quantum engineer's guide to superconducting qubits . Phys. Rev. Applied. **6**, 021318 (2020).

[2] *R. McDermott, M. G. Vavilov*, Accurate Qubit Control with Single Flux Quantum Pulses. **2**, 014007 (2014).

[3] *E. Leonard, Jr., M. A. Beck, J. Nelson, B.G. Christensen, T. Thorbeck, C. Howington*, Digital coherent control of a superconducting qubit. Phys. Rev. Applied. **11**, 014009 (2019).

[4] *M. Kjaergaard, M. E. Schwartz, J. Braumüller, P. Krantz, J. I.-J. Wang, S. Gustavsson, and W. D. Oliver*, Superconducting Qubits: Current State of Play. Annual Review of Condensed Matter Physics **11**, 369-395 (2020)

[5] *M.Dalgaard, F.Motzoi, J. J. Sørensen, J. Sherson*, Global optimization of quantum dynamics with AlphaZero deep exploration. npj Quantum Inf. **6** (2020).

Toroidal mode of a quantum metaatom in a circular waveguide

Ivan Stenishchev[1,2*], **Stanislav Gil'mulin**[1], **Alexey Basharin**[1,2]

[1] *The National University of Science and Technology MISIS, Russia, Moscow*
[2] *Institute of Theoretical and Applied Electrodynamics, Russian Academy of Sciences, Moscow, Russia*
*E-mail: `iv.steni@yandex.ru`

Abstract

In this work has been research a quantum metaatom based on a toroidal current mode with high Q-factors. The metaatom has been research in the circular waveguide. Measurements were carried out below the cutoff frequency of the waveguide to suppress radiation. The article presents a multipole expansion with allowance for irreducible terms, one-tone and two-tone spectroscopy.

The electromagnetic fields described in the far zone can be represented through a combination of the contributions of the electric, magnetic and toroidal families, taking into account their higher orders. In a complex system, oscillating poloidal displacement currents j. These currents are called toroidal. The total power dissipation P is calculated as the sum of these harmonics with coefficients determined by the radial and angular distributions of charge p and current density j induced in the source[1]. Primitive multipoles are not symmetric tensors, and therefore do not show an individual contribution to the dissipated power. However, they must be invariant to geometric transformations, which imposes the requirement to be discreet and symmetrical. The operation of symmetrization of primitive cartesian multipoles generates residual terms, which are irreducible toroidal moments [2]. aking into account these terms, we obtain the total power dissipation.

$$P_{scat} = \frac{k_0^4\sqrt{\epsilon_d}}{12\pi\epsilon_0 c\mu_0}\left|p_i + \frac{ik}{c}T_i^e + \frac{ik^3}{c}T_i^{2e}\right|^2 + \frac{k_0^4\epsilon_d\sqrt{\epsilon_d}}{12\pi\epsilon_0 c}\left|m_i + \frac{ik}{c}T_i^m\right|^2 + \frac{k_0^6\epsilon_d\sqrt{\epsilon_d}}{160\pi\epsilon_0^2 c\mu_0}\left|\widetilde{Q_{ij}^e} + \frac{ik}{c}\widetilde{T_{ij}^{Qe}}\right|^2 . \quad (1)$$

where p_i, m_i is the artesian multipoles. T_i^e, T_i^{2e}, T_i^m is the residual irreducible terms. The result of the multipole expansion is shown in Figure 1.

Experimental setup

The starting point for the creation of the qubit was the choice of the geometry of the inverted split ring resonator (ISRR), which is characterized by a high value of the toroidal dipole moment. One of the modes of the structure has two circuits with current. The chip has a SQUID instead of a Josephson junction. The controlled parameter of the metaatom was the critical current of the SQUID. The structure is studied in the superconducting regime at a temperature of 20 mK in a circular waveguide (d = 56.5 mm, l = 156 mm). The experimental setup is shown in Figure 1.

At a certain power of the probing signal, the current through the SQUID exceeds the critical one (it can be considered a resistor). With a smooth increase in power, for example, up to -5dBm, the single-tone spectrum will change in the direction of rectification. The first to lose dependence on the magnetic flux is peak, because it is characterized by a stronger current through the SQUID than dip at equal power. The graph of transmission coefficients is fitted with a Fano-curve.

The result of two-tone spectroscopy can be described using anharmonicity, which is related to the ratio $\frac{E_j}{E_c}$

$$\alpha = (E_1 - E_0) - (E_2 - E_1) = 540kHz \quad (2)$$

Calculation of anharmonicity in the program for electrodynamics simulation is performed using the following formula.

$$\alpha = \frac{(\hbar\omega)^2}{8E_j}\left(1 - \frac{W_H}{W_E}\right)^2 = 635kHz \quad (3)$$

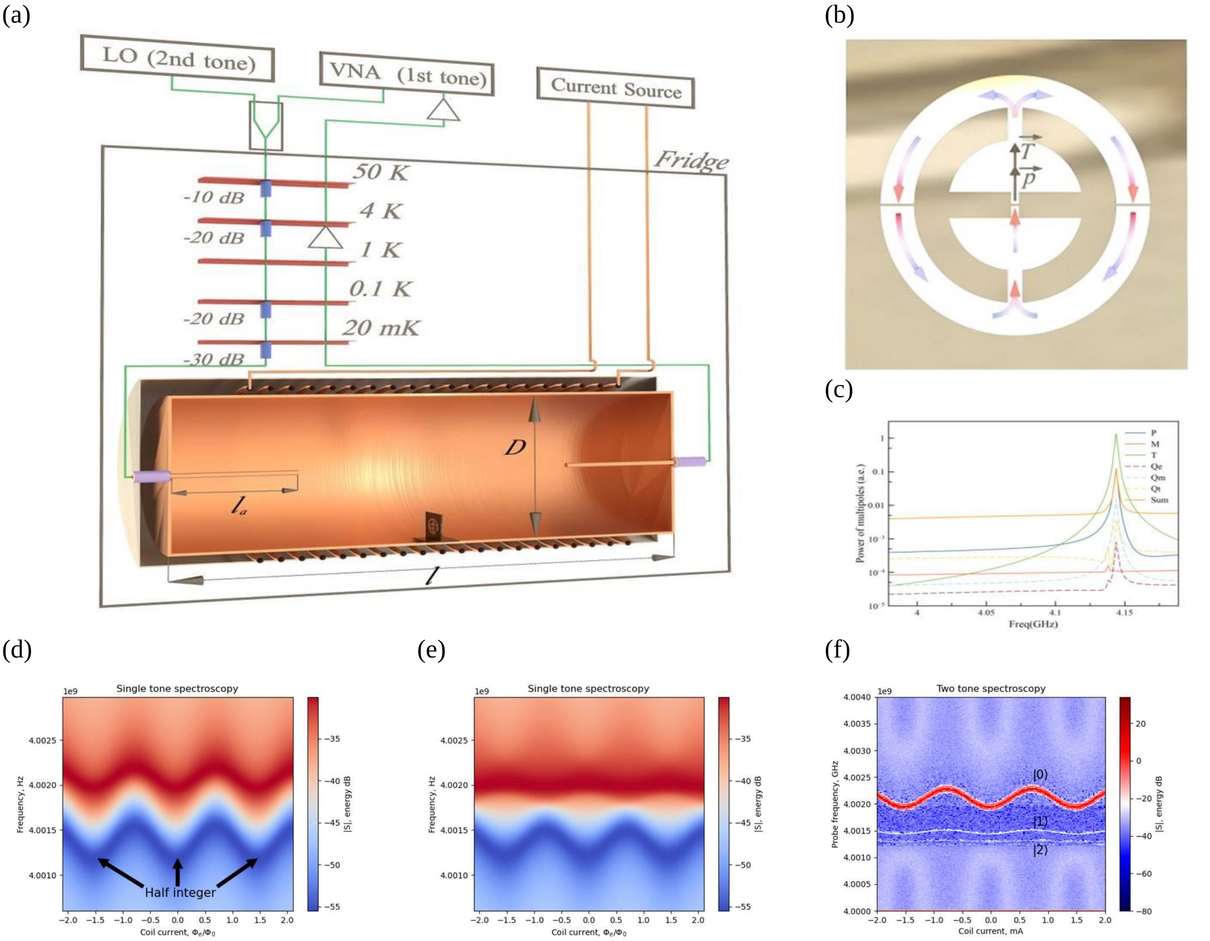

Figure 1: (a) Experimental setup, (b) current distribution, (c) multipole decomposition, (d) single-tone spectroscopy at -10dBm, (e) single-tone spectroscopy at 5dBm, (f) two-tone spectroscopy

where W_H and W_E are the powers of the electric and magnetic fields in the entire volume of the waveguide.

References

[1] *T. Kaelberer, V.A. Fedotov, N. Papasimakis, D.P. Tsai, and N.I. Zheludev*, Toroidal dipolar response in a metamaterial. Science **7**, 330(6010):1510-1512, 2010.

[2] *A. B. Evlyukhin, C. Reinhardt, E. Evlyukhin, and B. N. Chichkov*, Multipole analysis of light scattering by arbitrary-shaped nanoparticles on aplane surface. J. Opt. Soc. Am. B. **95**, 30, 10, 2589, 2013.

[3] *U. Fano*, Effects of Configuration Interaction on Intensities and Phase Shifts Phys. Rev. **95**, 124, 1866 (1961).

Impact of dynamically changing line losses on quantum key distribution

Konstantin Stepanov*, **Alina Borisova**

JSC "InfoTeCS", Moscow, Russia
*E-mail: Konstantin.Stepanov@infotecs.ru

Abstract

To ensure stable operation with high quality of service, quantum key distribution (QKD) systems require periodic parameters adjustments: alignment of delays, interferometers balancing, etc. It is assumed that the parameters of the communication line, for example, losses in the line, do not undergo significant changes during the quantum keys generation sessions. However, in real communication lines, the periods and amplitudes of loss fluctuations can be comparable with the generation time. The authors considered the influence of dynamically changing losses in the line on the quantum keys generation in QKD systems.

Introduction

Insertion loss limits the fraction of photons that reach the receiving side of the QKD, which affects the level (or percentage) of quantum errors [1]. The insertion loss is usually constant, determined by the line length ($\alpha \simeq 0{,}2$ dB/km) and connection losses. However, in some cases, for example, if the line is located on suspension supports, the cable may be subject to vibrations [2, 3]. Microbends are occurred in the fiber due to these vibrations, which causes additional non-stationary losses. Thus, it is actual to consider how the QKD parameters are affected by losses that vary with a period close to the key generation time.

Experimental setup and testing method

The experiment was carried out using the QKD system based on the phase-time protocol [4]. The scheme of the experimental setup is shown in Fig. 1.

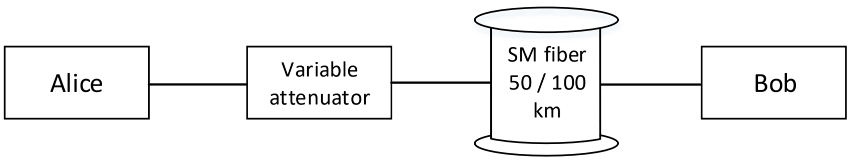

Figure 1: Experimental setup scheme

The built-in attenuator from the EXFO LTK-1 measuring platform was used as a tunable attenuator. The maximum frequency of loss change is 1 Hz. Setpoint error is less 0.01 dB. The tuning occurs by a rapid transition to a set value. During the experiment, the losses changed stepwise:

a) from 0 to the set value in one step,

b) in steps of 1 dB from 0 to the set value and back.

Each loss value was held for 1 s.

Based on the experimental results, the quantum key generation time was estimated for dynamically changing losses in the line. Table 1 shows the average and maximum values of the generation time of one key in the series.

Conclusion

Experiments demonstrated that the QKD system based on the phase-time protocol, withstands dynamic loss changes up to 3 dB in a line 100 km long and up to 8 dB in lines up to 50 km long. The results were obtained at the maximum loss change frequency 1 Hz. It was noticed that with smoother changes in losses, the generation is more stable.

Table 1: Influence of dynamic losses on generation time.

Line length	Loss changes amplitude, dB	Generation time of one key	
		Average, s	Maximum, s
100 km	0 (without changes)	7.9	14.3
	3	11.7	19.1
	6	No generation	
50 km	0 (without changes)	6.8	16.9
	3	6.0	17.2
	6	9.0	19.2
	8	10.2	31.0
	5 (1 dB tuning step)	6.2	11.9

References

[1] *S.N. Molotkov*, What is a quantum cryptography protocol that ensures the maximum distance in the case of a strictly single-photon source? JETP letters. **102**, 473 (2015).

[2] *B. Zhao, X. Zha, Z. Chen, R. Shi, D. Wang, T. Peng, and L. Yan*, Performance analysis of quantum key distribution technology for power business. Appl. Sci. **10**, 2906 (2020).

[3] *Y.Y. Ding, H. Chen, S. Wang, D.Y. He, Z.Q. Yin, W. Chen, Z. Zhou, G.C. Guo, and Z.F. Han*, Polarization variations in installed fibers and their influence on quantum key distribution systems. Opt. Express. **25**, 27923 (2017).

[4] *S.N. Molotkov*, Cryptographic robustness of a quantum cryptography system using phase-time coding. JETP letters. **106**, 1 (2008).

Deep quantum learning on a chain of superconducting qubits

Alexey Tolstobrov[1,4*], Gleb Fedorov[1,2,4], Shtefan Sanduleanu[1,2,4], Daria Kalacheva[3,1,2], Aleksey Bolgar[3,1], Viktor Lubsanov[1], Shamil Kadyrmetov[1], Alexander Dorogov[1,4], Andrey Vasenin[3,1], Aleksei Dmitriev[1,4] and Oleg V. Astafiev[3,1]

[1] *Moscow Institute of Physics and Technology*
[2] *National University of Scienece and Technology MISIS*
[3] *Skolkovo Institute of Science and Technology*
[4] *Russian Quantum Center, National University of Science and Technology MISIS*
*E-mail: `tolstobrov.ae@phystech.edu`

Abstract

We experimentally implement a supervised quantum learning algorithm in a chain of superconducting qubits to solve multilabel classification problems. We find a suitable gate sequence and training algorithm, which allows us to achieve classification accuracy $\geq 94\%$ for investigated datasets. The accuracy and stability of the algorithm is confirmed by the cross-validation method.

Introduction

The possibility of using such a nonlinear system as superconducting qubits for supervised learning has been of great interest to scientists over the recent years [1, 2]. It was also shown that there is possibility to use gradient-based methods in such kind of systems, by computing gradient using parameter-shift rule [2, 3]. The solution of the binary classification problem on such systems is experimentally demonstrated [4]. In this work we solved 3 different problems of supervised learning - parity problem, breast cancer (binary classification) and wines (multilabel classification).

Experimental setup

The investigated sample was fabricated as 8-transmon[5] chain. Each transmon had its own measurement resonator, and 2 control lines - to control the flux through the SQUID of transmon and to excite it with microwave radiation. A photo of the processor in an optical microscope is shown in Fig. .

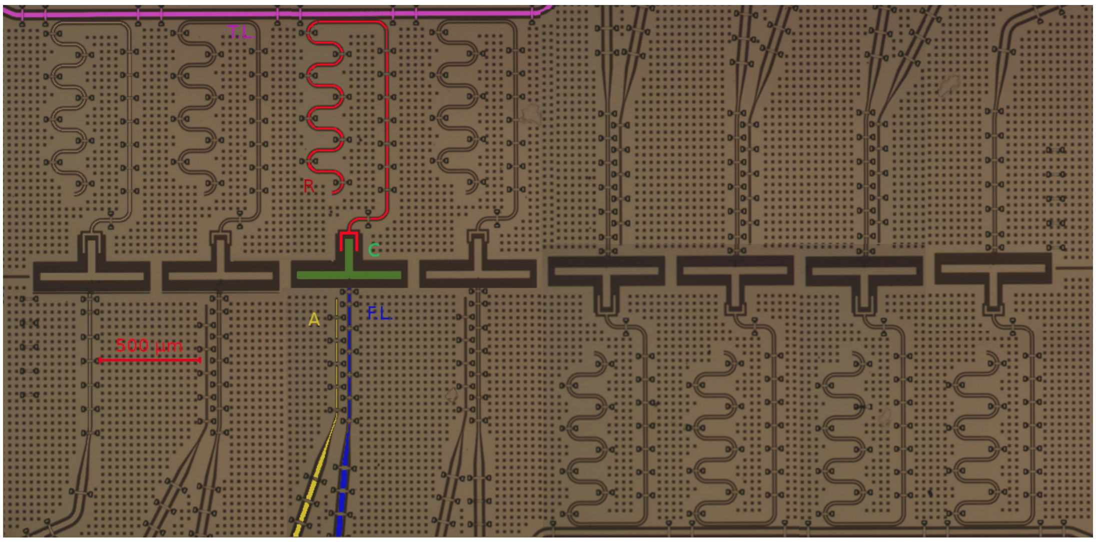

Figure 1: Micrograph of the 8-qubit quantum processor. Purple- transmission line, yellow - microwave antenna (for excitation of the qubit), blue - flux line, green - shunted capacity of the qubit, red - measuring resonator

Framework of quantum neural network

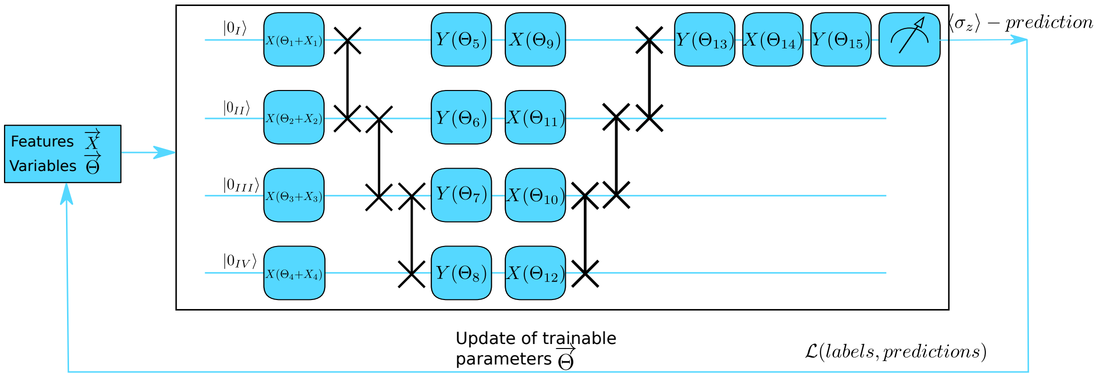

Figure 2: Schematic diagram of the quantum neural network

To simplify control of the circuit, we use only 4 out of 8 qubits in our experiments. The investigated quantum neural network consists of several layers (Fig.). Each of them has its own role. Input data is recorded in the first layer by transformation of 4 features into angles of single-qubit operations. Adding trainable biases $(\theta_1, \theta_2, \theta_3, \theta_4)$ to this angles is standard practice for machine learning and allows us to give more flexible model. The next stage in quantum circuit is entangling. This stage includes 3 two-qubit operations (i-Swap). After that we add 2 layers of single-qubit rotations with trainable angles. These operations make our model more complex because they are performed when the qubits are in an entangled state. These layers are followed by 3 two-qubit operations layers and arbitrary single-qubit rotation which is the composition of 3 (Y, X, Y) rotations. The last layer is measuring average value of $\langle\sigma_z\rangle$ for the first qubit. Having the output of quantum neural network, we use threshold classifier for the binary classification problem, which means that measured value $\langle\sigma_z\rangle \geq 0$ corresponds to the first class, while value $\langle\sigma_z\rangle<0$ corresponds to the second class. After that we compute the value of loss function on classical computer:

$$\mathcal{L}(labels, predictions) = \langle \log_2(1 + exp(-label \cdot prediction \cdot 10))\rangle, \tag{1}$$

where labels are the numbers from $\{1, -1\}$ and predictions - measured values of $\langle\sigma_z\rangle$ from -1 to 1. This function saturates to zero, when predictions have the same sign as corresponding labels, and increases linearly when they have different signs. Therefore, we need to find the minimum of this function in order to get a good classifier. This system allows us to use gradient-based methods to find minimum of the loss function. We use single-qubit rotation angles as trainable parameters of the circuit, so we have harmonic dependence of the output from $\langle\sigma_z\rangle$ and it is possible to compute partial derivative, using parameter-shift rule [2, 3]. We use mini-batch gradient-descent algorithm, which allows us to reach an optimum between speed and accuracy.

Experimental results

We solved 3 different classification tasks - parity problem, breast cancer and wines. In the parity problem we need to classify 4-bit sequences in two classes - even and odd. This problem is a simple test of our system, which shows the reproducibility of our operations and the ability of the system to be trained on reliable data. The next task - breast cancer - also binary classification problem, but it has a much larger dataset, which allows us to get more precise estimation of the working of our algorithm. We also tested the possibility of our system to solve multilabel classification problem on wines dataset. We made multilabel classification by solving 3 one-vs-others binary classification tasks. The dependence of the classifier quality from the number of iterations is shown in Fig. 3. To reliable measure accuracy of our algorithm we performed cross-validation of our algorithm, the results of cross validation are shown in Tab. 1.

Dataset	Parity	Cancer	Wines
Number of samples	16	569	178
Number of classes	2	2	3
Cross-validation accuracy	1.0	0.95	0.94

Table 1: Comparison of the investigated datasets

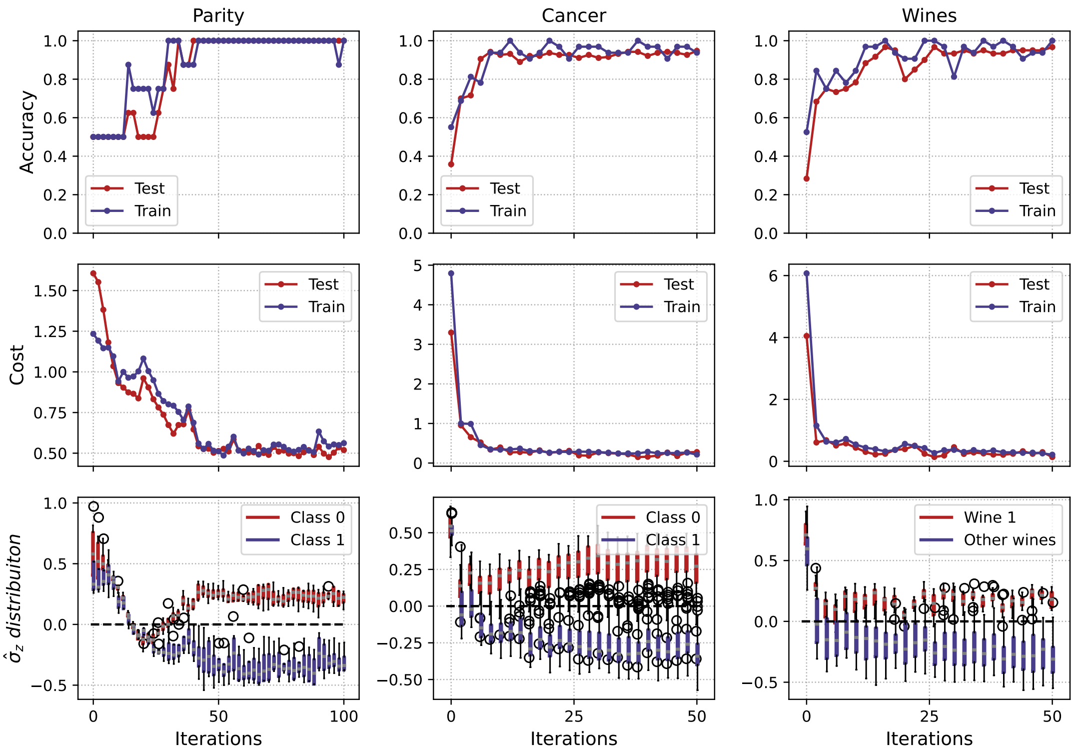

Figure 3: Training process of classifiers

Conclusion

The algorithm of multilabel classification is developed and experimentally performed in the chain of superconducting qubits. The obtained dependencies qualitatively converge with the results of numerical simulation. Obtained cross-validation accuracies close to the theoretical limit for this circuit.

Acknowledgements

The work was done in the frame of the Roadmap for the development in the Russian Federation the high-tech field of "Quantum Computation" for the period up to 2024. All samples were fabricated at the cleanroom facility of MIPT.

References

[1] Maria Schuld and Nathan Killoran. Quantum machine learning in feature hilbert spaces. *Phys. Rev. Lett.*, 122:040504, Feb 2019.

[2] K. Mitarai, M. Negoro, M. Kitagawa, and K. Fujii. Quantum circuit learning. *Phys. Rev. A*, 98:032309, Sep 2018.

[3] Maria Schuld, Alex Bocharov, Krysta M. Svore, and Nathan Wiebe. Circuit-centric quantum classifiers. *Phys. Rev. A*, 101:032308, Mar 2020.

[4] Wenhui Ren, Weikang Li, Shibo Xu, Ke Wang, Wenjie Jiang, Feitong Jin, Xuhao Zhu, Jiachen Chen, Zixuan Song, Pengfei Zhang, Hang Dong, Xu Zhang, Jinfeng Deng, Yu Gao, Chuanyu Zhang, Yaozu Wu, Bing Zhang, Qiujiang Guo, Hekang Li, Zhen Wang, Jacob Biamonte, Chao Song, Dong-Ling Deng, and H. Wang. Experimental quantum adversarial learning with programmable superconducting qubits. *Nature Computational Science*, 2(11):711–717, Nov 2022.

[5] Jens Koch, Terri M. Yu, Jay Gambetta, A. A. Houck, D. I. Schuster, J. Majer, Alexandre Blais, M. H. Devoret, S. M. Girvin, and R. J. Schoelkopf. Charge-insensitive qubit design derived from the cooper pair box. *Phys. Rev. A*, 76:042319, Oct 2007.